(NASA-CR-166227) INFRARED ASTRONOMICAL SATELLITE (IRAS) ANALYSIS OF THE TRANSMITTANCE OF OFF-AXIS ENERGY DUE TO SCATTERING AND DIFFRACTION Final Report (Breault Research Organization) 157 p HC A08/MF A01 N81-29964 THRU N81-29968 Unclas G3/74 32…

BREAULT RESEARCH ORGANIZATION

6012 E 27 Street Tucson, Arizona 85711

Errata No 1, Sept 21, 1976

for: Infrared Astronomical Satellite (IRAS)

Analysis of the Transmittance of Off-axis Energy Due to Scattering and Diffraction

Page 10, Section 2.1.1 First paragraph: change date to data.

Page 59, Equation 14. Add: for n<m

Page 60, Equation 16, first part: Add for n<m.

Equation 16, change to:

$$= \left| \sum_{n=1}^{N} A_n \right|^2$$

Page 63, Fourth line: Change to read as follows:

as a ficticious unit area surface normal to the incoming or out-

page 67, Paragraph 6.4.1 line 8, change to read as follows:

too cumbersome in the analysis of the fine-scale diffraction from the struts

Page 90, first line. Change $\theta=0$, to read $\theta_i \neq 0$

Page 92, Equation 74. Change to:

$$\phi = \cos^{-1} \{\tan w \cdot \tan(\phi_i/2)\} \qquad (74)$$

Page 100, 5% Diffuse at 88°: change from 3.5E-11 to 1.5E-11

Corresponding percentages now are: % Diffraction 99.
% Scatter 1.

BREAULT RESEARCH ORGANIZATION

6012 E 27 Street Tucson, Arizona 85711

Errata No 1, Sept 21, 1976

for: Infrared Astronomical Satellite (IRAS)

Analysis of the Transmittance
of Off-axis Energy Due to
Scattering and Diffraction

Page 10, Section 2.1.1 First paragraph: change date to data.

Page 59, Equation 14. Add: for n<m

Page 60, Equation 16, first part: Add for n<m.

Equation 16, change to:

$$= \left| \sum_{n=1}^{N} A_n \right|^2$$

Page 63, Fourth line: Change to read as follows:

as a ficticious unit area surface normal to the incoming or out-

page 67, Paragraph 6.4.1 line 8, change to read as follows:

too cumbersome in the analysis of the fine-scale diffraction from the struts

Page 90, first line. Change $\theta=0$, to read $\theta_i \neq 0$

Page 92, Equation 74. Change to:

$$\phi = \cos^{-1}\{\tan w \cdot \tan(\phi_i/2)\} \qquad (74)$$

Page 100, 5% Diffuse at 88°: change from 3.5E-11 to 1.5E-11

Corresponding percentages now are: % Diffraction 99.
% Scatter 1.

Page 102, Second line. Change % Diffuse to 5% Diffuse

5% diffuse at 24°, change from 9.5E-4 to 9.5E-5.

Corresponding Percentages now are % diffraction 1.

% scatter 99.

5% diffuse at 30°, change from 9.8E-5 to 9.8E-6

The total now becomes 1.0E-5 instead of 9.8E-5

Corresponding percentages now are: % diffraction 4.

% scatter 96.

Second line from bottom, change % Diffuse to % Diffraction

Page 104, 5% diffuse at 30°: change from 1.1E-5 to 9.8E-6

Corresponding percentages now are: % diffraction 9.

% scatter 91.

Page 102, Second summation with Martin Black at 88°

Change from 1.8E-13 to 1.4E-8

Page B-10 Change line 15 to:

$(x,y) = (0 \pm R).$

Page B-11 Change asymptotoc to asymptotic.

Page B-13 First equation (the one before B-46). The third exponential term in the brackets should have a minus (-) in the exponent:

$$+e^{-ik\beta_i S/\sqrt{2}}$$

TABLE OF CONTENTS

TABLE OF CONTENTS, Cont.

Figures

Figures, Cont.

Figures, Cont.

Figures, Cont.

TABLES

N81-29965

1.0 INTRODUCTION

This report contains the results of stray-light transmittance analysis on Perkin-Elmer's design of the Infrared Astronomical Satellite (IRAS), design number 693-10000, Revision E, dated May 9, 1978. The system was evaluated for scattered radiation propagation with the use of the APART (Arizona's Paraxial Analysis of Radiation Transfer, version 6), and the propagation of diffracted energy with both PADE (Paraxial Analysis of Diffracted Energy) and Perkin-Elmer's GUERAP II programs. The results of scatter and diffraction are first presented separately, with the combined transmittance values being presented later.

The scattered radiation analysis was performed by using both a 5% diffuse black on all the baffle and vane surfaces and by using a mathematical model of the Martin Black scattering characteristics. The results of the IR scattered-radiation analysis show that the majority of radiation comes from the inner-secondary baffle and the object side of the aperture stop. In the visible wavelengths, the primary and secondary mirrors are the dominant sources of unwanted radiation at all off-axis angles.

For all wavelengths, diffraction effects are dominant only at the large off-axis angles, except for a few specific cases at smaller angles. This is somewhat contrary to popular opinion which holds that at the long wavelengths diffraction effects will predominate. This report clearly shows that at the longer wavelengths the diffraction contributions go up significantly; however, surface-scattering characteristics are also larger, resulting in more unwanted energy reaching the image plane due to scattered radiation. It is the comparative increase which determines which propagation process predominates.

The following tasks were outlined in the Statement of Work:[1]

1. Perform an independent analysis of the off-axis rejection of the IRAS Telescope System (including sunshade, optical subsystem, and field optics) considering the effects of both scattering and diffraction over the operating wavelength range of the telescope. The telescope design analyzed shall represent the flight design to the maximum extent possible. The optical subsystem is defined to include the telescope optics, structure, and baffles. The requirements for off-axis rejection shall be as defined in Specification 2-26412 "Performance Requirements for an Infrared Telescope System for the Infrared Astronomical Satellite (IRAS)" Revision 5, dated September 15, 1977 or the latest modification thereto. The analysis shall include but not be limited to the following elements:
   (a) Computation of the off-axis rejection of the optical subsystem by itself for direct comparison with the Perkin-Elmer analysis.
   (b) Computation of the azimuthal variation of diffraction of the telescope for comparison as in (a) above.
   (c) Computation of the effects of the field optics including both the cavity behind the field lens and the aperture that preceeds the detector cavity.
   (d) Computation of the system off-axis performance at 632.8 nm and 10.4 nm.

The analysis in each task shows, in most cases, good agreement with Perkin-Elmer's original analysis, even though the systems analyzed were slightly different.

The specular sunshield effectively blocks off the solar radiation for off-axis angles greater than 60°. However, because of its specular coating, it may collect and reflect unwanted radiation from near off-axis sources into the system. The field masks and lenses in the final flight system will alter the propagation paths to the individual detectors. In all cases this will result in better off-axis rejection. For a few off-axis positions, the masks will provide the crucial reduction required to meet the specifications.

The stray light requirements used in this analysis are those defined in Specification 2-26412, which are repeated here:

3.2.2.3 Stray Light Rejection

The Telescope System stray light rejection requirements are defined as follows:

a. Let $P(\theta)$ be the power (watts) from an unwanted point source detected when the Telescope System's line of sight is displaced an angle θ from the point source. $P(\theta = 0) = P(0)$ is then the power that could be detected if the point source were imaged directly on the detector.

b. The normalized off-axis attenuation $A(\theta)$ is defined as

$$A(\theta) = \frac{1}{\Omega} \frac{P(\theta)}{P(0)} \text{ sr}^{-1}$$

where Ω is the solid angle (sr) subtended by the detector. The Telescope System shall have a normalized off-axis attenuation equal to or less than the values of $A(\theta)$ tabulated below in Table 3.2.2.3.

Table 3.2.2.3
REQUIRED A(θ) sr^{-1}

Spectral Band (μm)

θ	0.4 - 0.9	8 - 15	15 - 30	48 - 81	87 - 118
5°	1×10	7×10^{0}	3×10^{-1}	4×10^{-2}	2×10^{-2}
24°	3×10^{-1}	1×10^{-5}	8×10^{-6}	4×10^{-6}	5×10^{-6}
60°	3×10^{-7}	5×10^{-8}	1×10^{-7}	2×10^{-7}	1×10^{-7}
88°	1×10^{-7}	2×10^{-8}	9×10^{-9}	4×10^{-9}	4×10^{-9}

In any computerized stray-light analysis, the model of the system is very important, including the scattering characteristics of the surfaces. The surface elements that were used in this analysis are shown in Figs. 1 to 3. Figure 1 shows those elements that were modeled as existing in object space (space one). Table 1 describes each surface according to the numbers that appear in the three figures. Because of the nature of the APART program, the appropriate elements must be entered into each space of the system. As can be seen in the three figures, the elements in each space need not be the same.

Elements numbered 5 and 6 are the sections of the primary baffle which have vanes. In APART, the locus of vane tips is entered as the "surface" of the element. This accounts for the odd shape of sections 5 and 6 relative to section 8.

Section 8 has some localized vane structure to shield rivets along the barrel baffle seam that is not accounted for in the analysis. These structures are comparatively small and should not adversely affect the results.

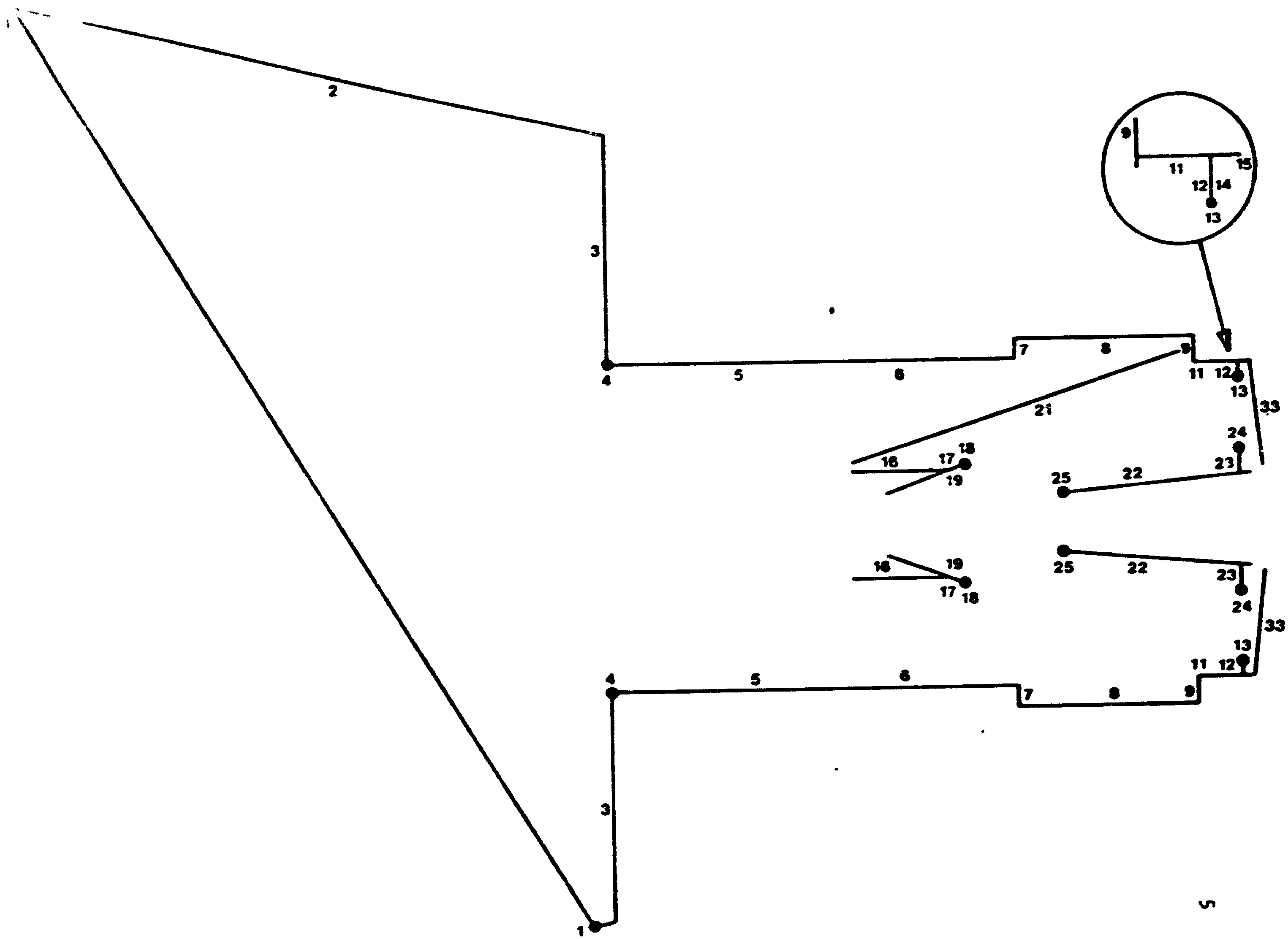

Fig. 1. IRAS Surfaces Modeled into Space One.

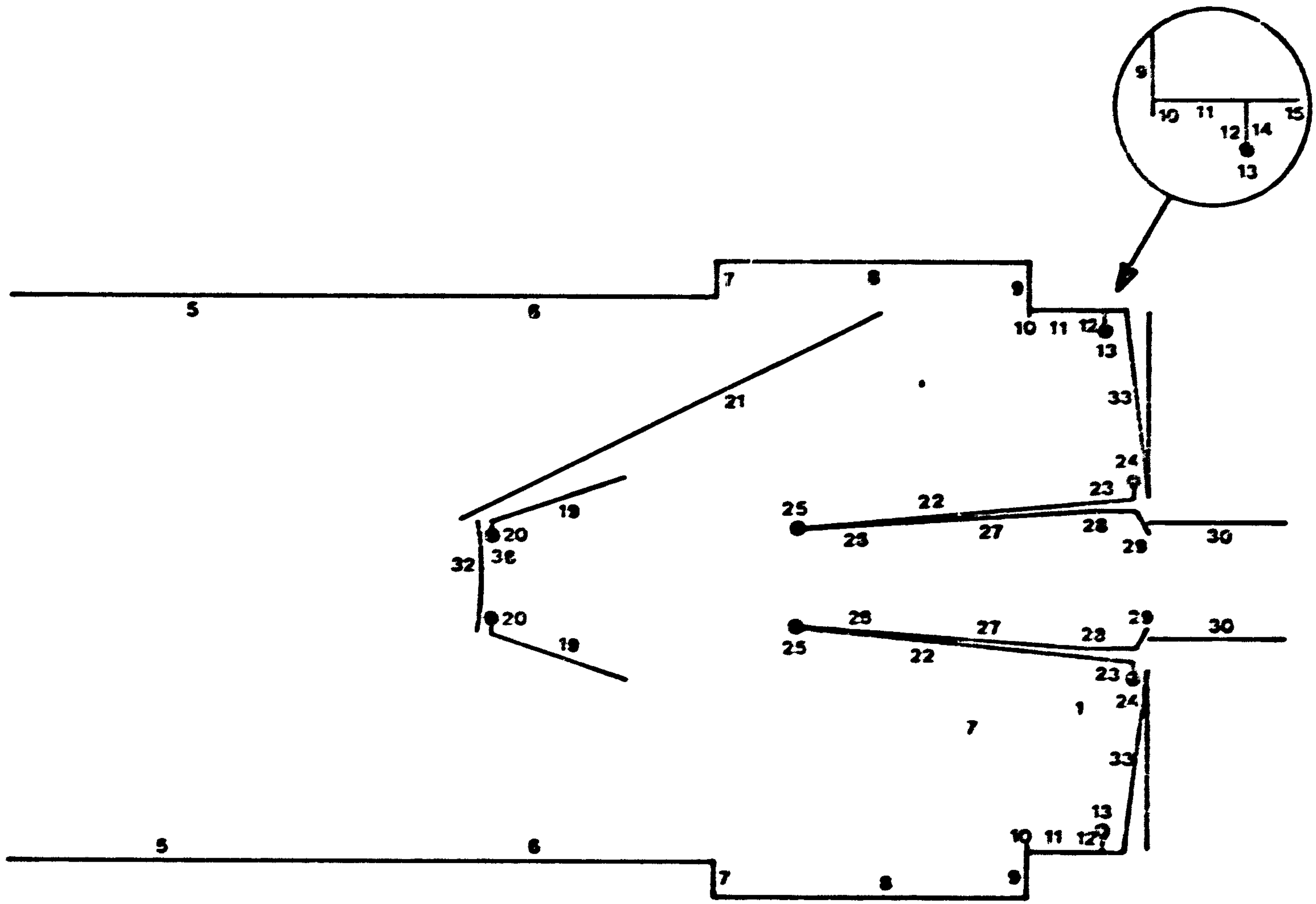

Fig. 2. Objects Modeled in Space Two (Between the Primary and Secondary).

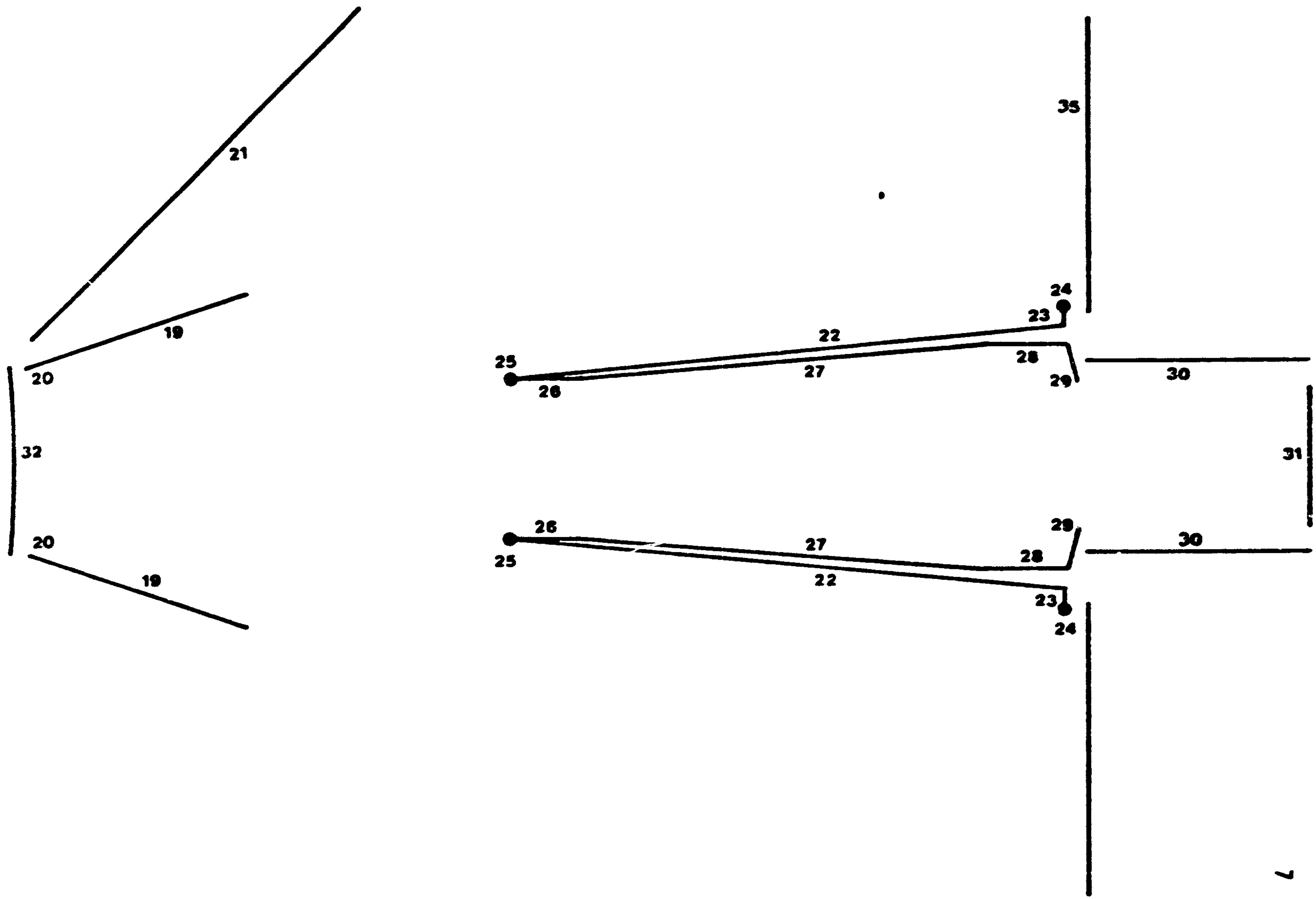

Fig. 3. Objects Modeled in Space Three (Image Space).

Table 1. Description of Objects Used in APART.

Object #	Description	Sections
1	Elliptical tilted diffracting edge	1 x 5
2	Sliced at 31° conical reflecting shield	5
3	Disk as radiators	4
4	Entrance port diffracting edge	1
5	Front section of main tube where first 5 vanes are 88.5 mm separation	5
6	Second front section of main tube where 8 vanes are spaced 44.2 mm apart	4
7	Right side of the last vane of object 6	2
8	Vaneless side wall of the main baffle	5
9	Vane at right side of object 8	1
10	Small right side of object 9	1
11	Baffle extending from aperture stop backward	1
12	Left side of aperture stop vane	1
13	Diffracting aperture stop tip	1
14	Right side of aperture stop	1
15	Small cylinder extending from aperture stop to primary mirror	1
16	Cylindrical outside of secondary structure	1
17	Conical outside of the secondary baffle	1
18	Secondary baffle tip	1
19	Inside of secondary baffle	5
20	Small extension from secondary baffle toward secondary mirror	1
21	Back side of spider support	10 x 3
22	Outside of inner conical baffle	5 x 5
23	Inner obscuration vane at the primary mirror	1
24	Diffracting edge at tip of inner conical baffle	1
25	Diffracting edge at tip of inner conical baffle	1
26	Cylindrical end of inner conical	1
27	Middle part of the inner conical baffle	4
28	Cylindrical right end of inner conical baffle	2

Table I. Description of Objects Used in APART, Cont.

Object #	Description	Sections
29	Steep cone at right end of inner conical baffle	2
30	Image baffle	2
31	Image	5
32	Secondary mirror	4
33	Primary mirror	6
34	Not used	
35	Primary mirror as used in space three	6

2.0 ANALYSIS OF THE OPTICAL SUBSYSTEM (OSS)

2.1 COMPARISON WITH PERKIN-ELMER'S ANALYSIS

2.1.1. The Visible Band. The analysis of the optical subsystem (OSS) was performed to permit a comparison with the Perkin-Elmer analysis as reported in PE Report No. 13616. Initial evaluation of this report and a listing of the input data decks revealed some conflicting information. Figures 1 and 2 from the report are reproduced here as Figs. 4 and 5. By observation, one can see that the size of the inner-primary baffle near the primary is much too large and the aperture stop appears to be too small. A check of the data input listing,[3] Fig. 6, shows that neither is the case. As was explained in the introduction, object 2 in the PE report should have the locus of the vane tips used as the "surface". The drawing is inconsistent with the actual (and correct) date input. The only error in PE's input data is the reference values of the marginal and chief rays for each of the spaces. The detailed effect of this error on the calculations is quite complicated; briefly, it will shift the location of the image of the objects.

Table 2 shows the percent of power contributed to the full detector area ($r = 5.04$ cm) from each of the individual objects. The black coatings were assumed to be 5% Lambertian diffuse. Ths mirror coating had a BRDF of 1.75E-1 sr^{-1} at $\beta - \beta_o = .01$ with a β^{-1} falloff. This value is 100 times higher than the BRDF specified by PE for 10 μ. However, PE later[4] did specify a $(\lambda/\lambda_o)^{-2}$ scaling at $\lambda_o = 10$ μ. The mirror BRDF used is thus about 2.3 times lower than the appropriately scaled data. Subsequent analysis reported here will include the BRDF scaled according

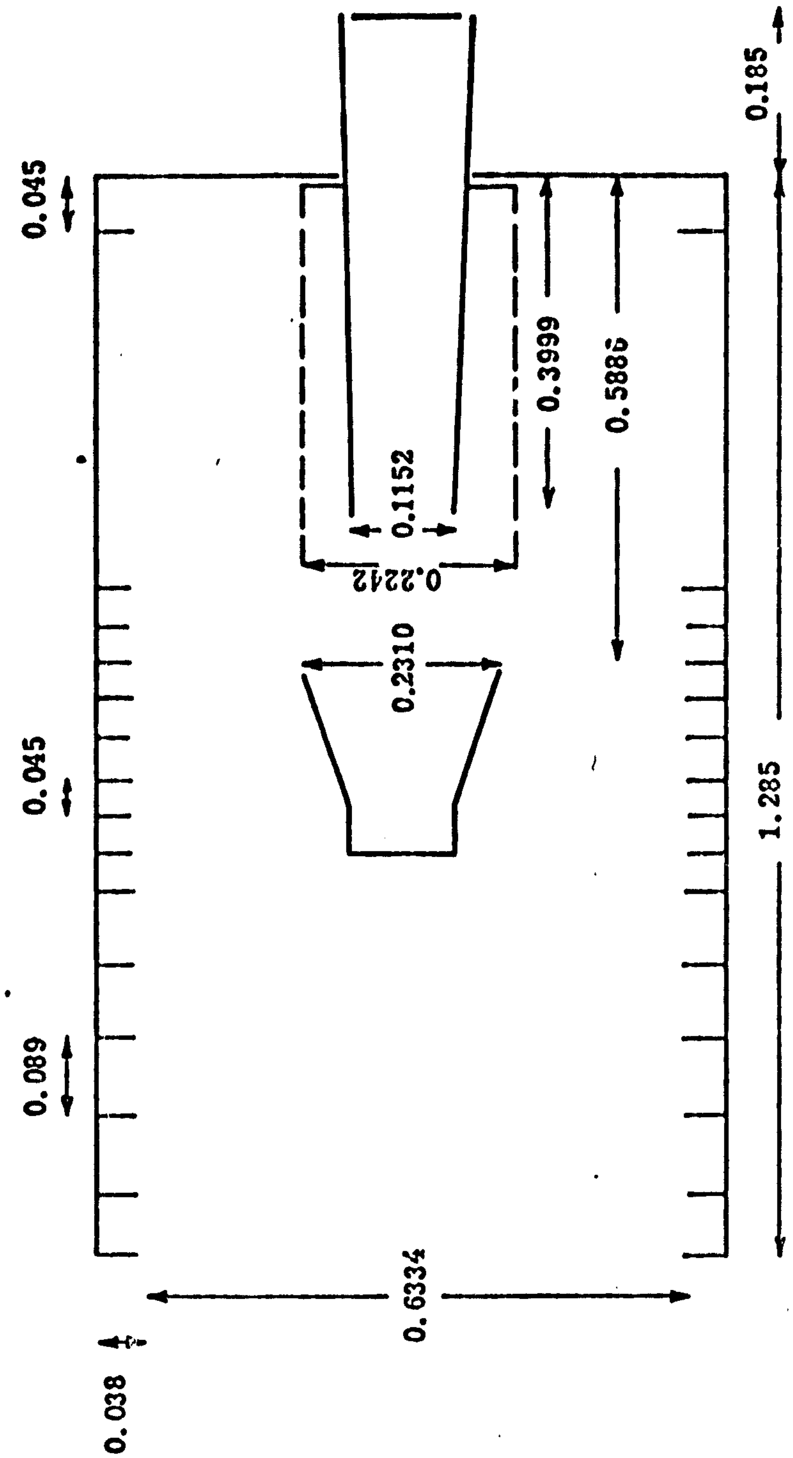

All Dimensions in Meters

Fig. 4. IRAS Baffle Design (Units Meters), PE Data.[5]

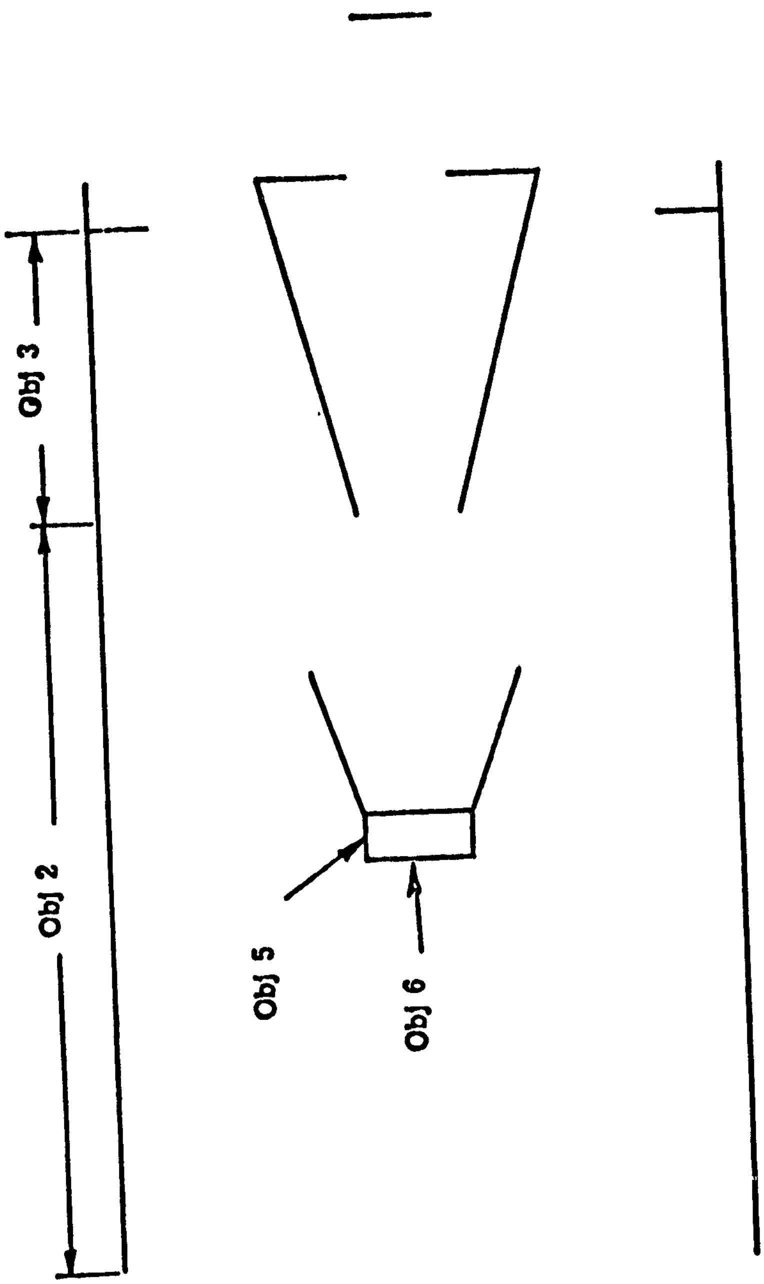

Fig. 5. Model Used for APART Program Calculations, PE Data.[6]

```
YZERO .75
VERSION ABSOLUTE
OBJECT 2 -1 10 -1.285 .309 1 -1 .3 -.0112788
OBJECT 2 1 10 -.3999 .309 1 -1
OBJECT 1 1 10 -100. 27.73 1 -1
OBJECT 1 1 10 -80.38 47.35 1 -1
OBJECT 3 1 10 -.3999 .367 1 -1
OBJECT 3 1 10 -.05413 .367 1 -1
OBJECT 4 1 10 -.05413 .30 1 -1
OBJECT 4 1 10 -.054 .367 1 -1
OBJECT 5 1 3 -.8244 .058 1 1
OBJECT 5 1 3 -.747 .059 1 1
OBJECT 6 1 3 -.8244 .059 1 -1
OBJECT 6 1 3 -.8244 0. 1 -1
OBJECT 7 1 5 -.747 .059 1 1
OBJECT 7 1 5 -.5886 .1116 1 1
OBJECT 8 1 5 -.3999 .05728 1 1
OBJECT 8 1 5 0. .100 1 1
OBJECT 9 1 5 -.7474313  .05771 1 -1
OBJECT 9 1 5 -.5886 .1089 1 -1
OBJECT 10 1 3 -.7474313  .05771 1 1
OBJECT 10 1 3 -.7474313 0. 1 1
OBJECT 11 1 10 -.3999 .05628 1 -1
OBJECT 11 1 10 0. .056 1 -1
OBJECT 12 1 5 .0266 .310 1 -1
OBJECT 12 -1 5 0. .310 1 -1 .3 4.96E-4
OBJECT 22 -1 5 0. .310 -1 -1 .3 4.96E-4
OBJECT 22 1 5 .0266 .310 -1 -1
OBJECT 32 1 10 -1.285 .309 -1 -1
OBJECT 32 1 10 -.3999 .309 -1 -1
OBJECT 33 1 10 -.3999 .367 -1 -1
OBJECT 33 1 10 -.05413 .367 -1 -1
OBJECT 34 1 10 -.05413 .3 -1 -1
OBJECT 34 1 10 -.054 .367 -1 -1
OBJECT 35 1 3 -.8244 .058 -1 1
OBJECT 35 1 3 -.747 .059 -1 1
OBJECT 36 1 3 -.8244 .059 -1 -1
OBJECT 36 1 3 -.8244 0. -1 -1
OBJECT 37 1 5 -.747 .059 -1 1
OBJECT 37 1 5 -.5886 .1116 -1 1
OBJECT 38 1 5 -.3999 .05728 -1 1
OBJECT 38 1 5 0. .100 -1 1
OBJECT 39 1 5 -.7474313  .05771 -1 -1
OBJECT 39 1 5 -.5886 .1089 -1 -1
OBJECT 41 1 10 -.3999 .05628 -1 -1
OBJECT 41 1 10 0. .056 -1 -1
OBJECT 40 1 3 -.7474313  .05771 -1 1
OBJECT 40 -1 3 -.7474313 0. -1 1 .050856239 6.848889E-3
OBJECT 60 -1 3 -.7474313  .05771 1 1 .050856239 6.848889E-3
OBJECT 60 1 3 -.7474313 0. 1 1
OBJECT 62 1 10 -1.285 .309 1 -1
OBJECT 62 1 10 -.3999 .3090 1 -1
OBJECT 63 1 10 -.3999 .367 1 -1
OBJECT 63 1 10 -.05413 .367 1 -1
OBJECT 64 1 10 -.05413 .30 1 -1
OBJECT 64 1 10 -.054 .367 1 -1
OBJECT 68 1 5 -.3999 .05728 1 1
OBJECT 68 1 5 0. .100 1 1
```


Rear Part of Aperture Stop Only.

Fig. 6. Input Data Listing from Perkin-Elmer's Analysis.

Table 2. % Power Contributions to Image for Visible Wavelengths and 5% Diffuse.

Percent of Power Contributed by Each Object as a
Function of Off-axis Source Position

OBJECT / OFF AXIS POSITION	1	2	3	4	5	6	7
1 SHIELD TIP	0.0	0.0	0.0	0.0	0.0	0.0	0.0
2 OUTER SHIELD	0.0	0.0	0.0	0.0	0.0	0.0	0.0
3 RADIATOR	0.0	0.0	0.0	0.0	0.0	0.0	0.0
4 ENTRANCE APT TIP	0.0	0.0	0.0	0.0	0.0	0.0	0.0
5 OUTER MAIN BAFFLE	0.0	0.0	0.0	0.0	0.0	0.0	0.0
6 MIDDLE MAIN BAFFLE	0.0	0.0	0.0	0.0	0.0	0.0	0.0
7 MIDDLE RIGHT END	0.0	0.0	0.0	0.0	0.0	0.0	0.0
8 INNER MAIN BAFFLE	0.0	0.0	0.0	0.0	0.0	0.0	0.0
9 INNER RIGHT END	0.0	0.0	0.0	0.0	0.0	0.0	0.0
10 RIGHT END	0.0	0.0	0.0	0.0	0.0	0.0	0.0
11 LEFT APT CONE	0.0	0.0	4.0	29.7	0.0	.6	.3
12 LEFT APERTURE	0.0	0.0	19.4	73.2	0.0	.5	1.6
13 APERTURE STOP	0.0	0.0	0.0	0.0	0.0	0.0	0.0
14 RIGHT APERTURE	0.0	0.0	6.2	0.0	0.0	0.0	0.0
15 RIGHT APT CONE	0.0	0.0	0.0	0.0	0.0	0.0	0.0
16 SEC HOUSING	0.0	0.0	0.0	0.0	0.0	0.0	0.0
17 OUTER SEC. BAFF	0.0	0.0	0.0	0.0	0.0	0.0	0.0
18 SEC. BAFF TIP	0.0	0.0	0.0	0.0	0.0	0.0	0.0
19 INNER SEC BAFFLE	56.5	13.7	0.0	0.0	84.5	13.7	42.8
20 INNER SEC TIP	0.0	0.0	0.0	0.0	0.0	3.2	10.2
21 STRUT BACK	0.0	0.0	0.0	0.0	0.0	.3	1.2
22 OUTER CONICAL	0.0	0.0	0.0	0.0	0.0	0.0	0.0
23 CENTERAL CIRCLE	0.0	0.0	0.0	0.0	0.0	.1	.3
24 CENT OBSCUR TIP	0.0	0.0	0.0	0.0	0.0	0.0	0.0
25 OUTER CONICAL TIP	0.0	0.0	0.0	0.0	0.0	0.0	0.0
26 LEFT INNER CONICAL	0.0	0.0	0.0	0.0	0.0	.8	.1
27 MIDDLE INNER CONICAL	0.0	0.0	0.0	0.0	0.0	64.5	.7
28 RIGHT INNER CONICAL	0.0	0.0	0.0	0.0	0.0	0.0	0.0
29 INNER CONICAL END	0.0	0.0	0.0	0.0	0.0	0.0	0.0
30 IMAGE BAFFLE	0.0	0.0	0.0	0.0	0.0	0.0	0.0
31 IMAGE	0.0	0.0	0.0	0.0	0.0	0.0	0.0
32 SECONDARY MIRROR	32.3	0.0	0.0	0.0	.5	4.9	15.6
33 PRIMARY MIRROR	11.1	86.3	47.6	0.0	15.5	11.3	26.7
34 ENTRANCE PORT	0.0	0.0	0.0	0.0	0.0	0.0	0.0
35 PRIM MIRROR AS DISK	0.0	0.0	0.0	0.0	0.0	0.0	0.0
36 POINT SOURCE	0.0	0.0	0.0	0.0	0.0	0.0	0.0

TOTAL POWER	.[illegible]E-01	.20[illegible]E-02	.660E-03	.[illegible]E-04	.121E-04	.154E-06	.108E-03
SOURCE ANG	5.0	10.0	17.0	24.0	30.0	60.0	85.0

* Infrared Astronomical Satellite (IRAS)
Scattered Light Analysis of OSS
For Ames Research Center NASA June 21, 1978
Perkin-Elmer Design Number 693-10000 Revision E of 5/9/78
Units are cm BRO

ORIGINAL PAGE IS OF POOR QUALITY

to the PE formula. In either case, the significant contributors are the inner-secondary baffle, the primary, and the aperture stop.

A detailed critique of the design or an analysis for each off-axis position will be avoided here as this analysis is to compare results with those obtained by PE. Significant differences in the principal propagation paths will be highlighted. When the flight version (OSS plus sunshield, field optics, and masks) is evaluated, there will be greater detail so that the effects of suggested design changes will be readily recognized.

The above analysis, with a 5% diffuse black coating, was repeated using a model of Martin Black as the surface scatterer. A brief description of the model is given in Appendix A. This model accounts for the higher forward scatter and lower back scatter that is characteristic of Martin Black. The results with the Martin Black model (Table 3) show some significant changes in the propagation paths due to the above characteristics. The A(0) values are plotted in Fig. 7 for both runs along with the specification for the 0.4 to 0.9 μ band.

A comparison of PE results (Fig. 8) with our analysis shows excellent agreement except for one data point at 10°. PE reports that the major contributor at this angle should be the inside of the secondary baffle. However, this was added as a separate hand calculation.[7] APART calculated the power focused onto the inner-secondary baffle; it then computed the radiation scattered forward toward the image of the detector as imaged by the secondary and also the energy backscattered to the primary and through the secondary before reaching the image. The area directly

Table 3. % Power to Image for Visible Wavelengths and Martin Black Coating.

Percent of Power Contributed by Each Object as a Function of Off-axis Source Position

OBJECTS/	OFF AXIS POSITION 1	2	3	4	5	6	7
1 SHIELD TIP	0.0	0.0	0.0	0.0	0.0	0.0	0.0
2 OUTER SHIELD	0.0	0.0	0.0	0.0	0.0	0.0	0.0
3 RADIATOR	0.0	0.0	0.0	0.0	0.0	0.0	0.0
4 ENTRANCE APT TIP	0.0	0.0	0.0	0.0	0.0	0.0	0.0
5 OUTER MAIN BAFFLE	0.0	0.0	0.0	0.0	0.0	0.0	0.0
6 MIDDLE MAIN BAFFLE	0.0	0.0	0.0	0.0	0.0	0.0	0.0
7 MIDDLE RIGHT END	0.0	0.0	0.0	0.0	0.0	0.0	0.0
8 INNER MAIN BAFFLE	0.0	0.0	0.0	0.0	0.0	0.0	0.0
9 INNER RIGHT END	0.0	0.0	0.0	0.0	0.0	0.0	0.0
10 RIGHT END	0.0	0.0	0.0	0.0	0.0	0.0	0.0
11 LEFT APT CONE	0.0	0.0	.4	26.3	0.0	.0	.0
12 LEFT APERTURE	0.0	0.0	2.0	73.7	0.0	.0	.1
13 APERTURE STOP	0.0	0.0	0.0	0.0	0.0	0.0	0.0
14 RIGHT APE TUBE	0.0	0.0	.9	0.0	0.0	0.0	0.0
15 RIGHT APT CONE	0.0	0.0	0.0	0.0	0.0	0.0	0.0
16 SEC HOUSING	0.0	0.0	0.0	0.0	0.0	0.0	0.0
17 OUTER SEC. BAFF	0.0	0.0	0.0	0.0	0.0	0.0	0.0
18 SEC. BAFF TIP	0.0	0.0	0.0	0.0	0.0	0.0	0.0
19 INNER SEC BAFFLE	58.2	84.5	0.0	0.0	12.6	1.5	35.1
20 INNER SEC TIP	0.0	0.0	0.0	0.0	0.0	.0	1.0
21 STRUT BACK	0.0	0.0	0.0	0.0	0.0	.0	.1
22 OUTER CONICAL	0.0	0.0	0.0	0.0	0.0	0.0	0.0
23 CENTRAL OBSCUR	0.0	0.0	0.0	0.0	0.0	.0	.0
24 CENT OBSCUR TIP	0.0	0.0	0.0	0.0	0.0	0.0	0.0
25 OUTER CONICAL TIP	0.0	0.0	0.0	0.0	0.0	0.0	0.0
26 LEFT INNER CONICAL	0.0	0.0	0.0	0.0	0.0	.1	.9
27 MIDDLE INNER CONICAL	0.0	0.0	0.0	0.0	0.0	95.3	7.6
28 RIGHT INNER CONICAL	0.0	0.0	0.0	0.0	0.0	0.0	0.0
29 INNER CONICAL END	0.0	0.0	0.0	0.0	0.0	0.0	0.0
30 IMAGE BAFFLE	0.0	0.0	0.0	0.0	0.0	0.0	0.0
31 IMAGE	0.0	0.0	0.0	0.0	0.0	0.0	0.0
32 SECONDARY MIRROR	31.1	0.0	0.0	0.0	.0	.9	21.0
33 PRIMARY MIRROR	10.7	15.5	96.8	0.0	87.4	2.1	34.2
34 ENTRANCE PORT	0.0	0.0	0.0	0.0	0.0	0.0	0.0
35 PRIM MIRROR AS DISK	0.0	0.0	0.0	0.0	0.0	0.0	0.0
36 POINT SOURCE	0.0	0.0	0.0	0.0	0.0	0.0	0.0
TOTAL POWER	.644E-01	.116E-01	.461E-03	.589E-05	.525E-04	.321E-07	.339E-10
SOURCE ANG	5.0	10.0	17.0	24.0	30.0	60.0	88.0

*Infrared Astonomical Satellite (IRAS)
*Scattered Light Analysis of OSS
*Perkin-Elmer Design Number 693-10000 Revision E of 5/9/78
*Units are cm Bro

ORIGINAL PAGE IS
OF POOR QUALITY

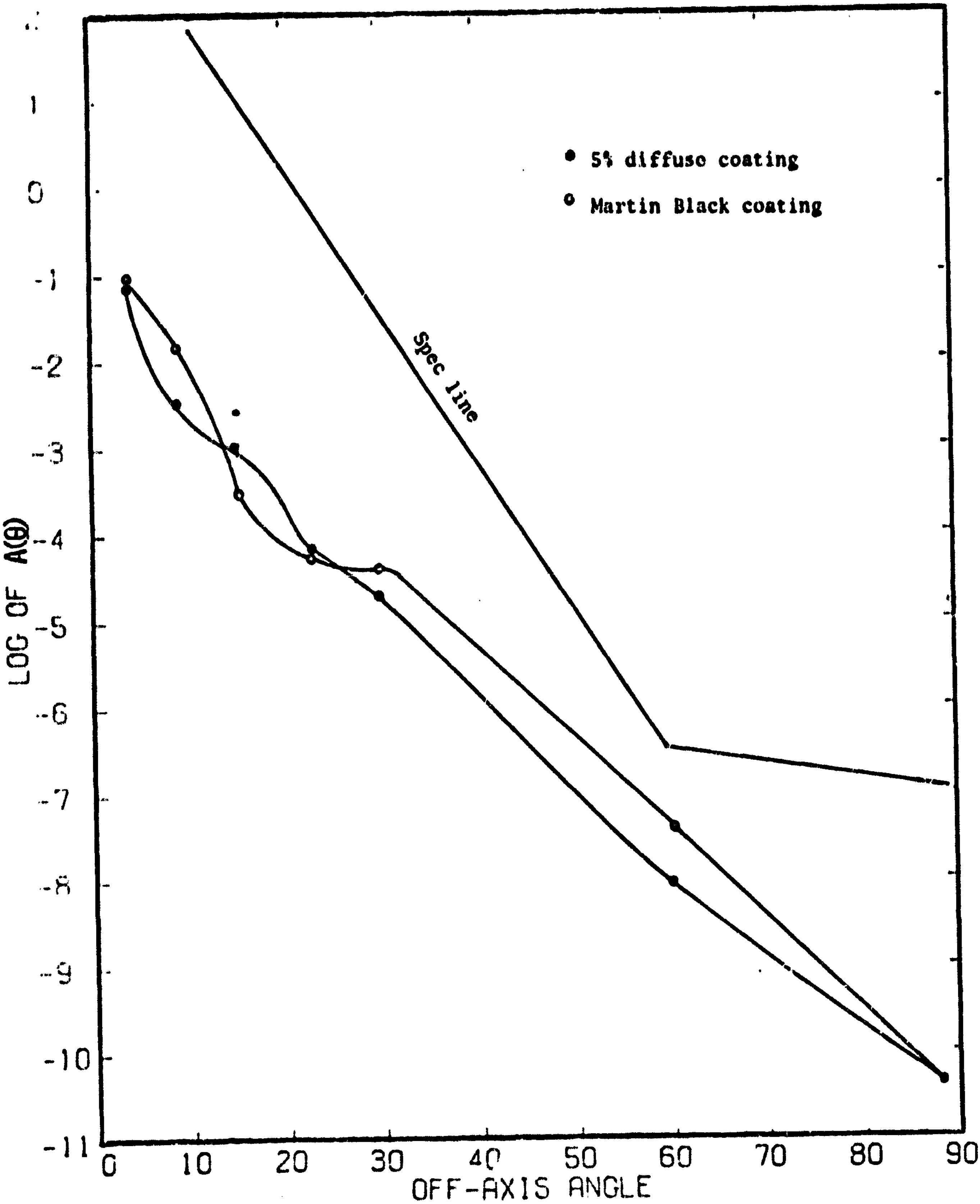

Fig. 7. 0.4 - 1.9μ Performance without the Field Mask.

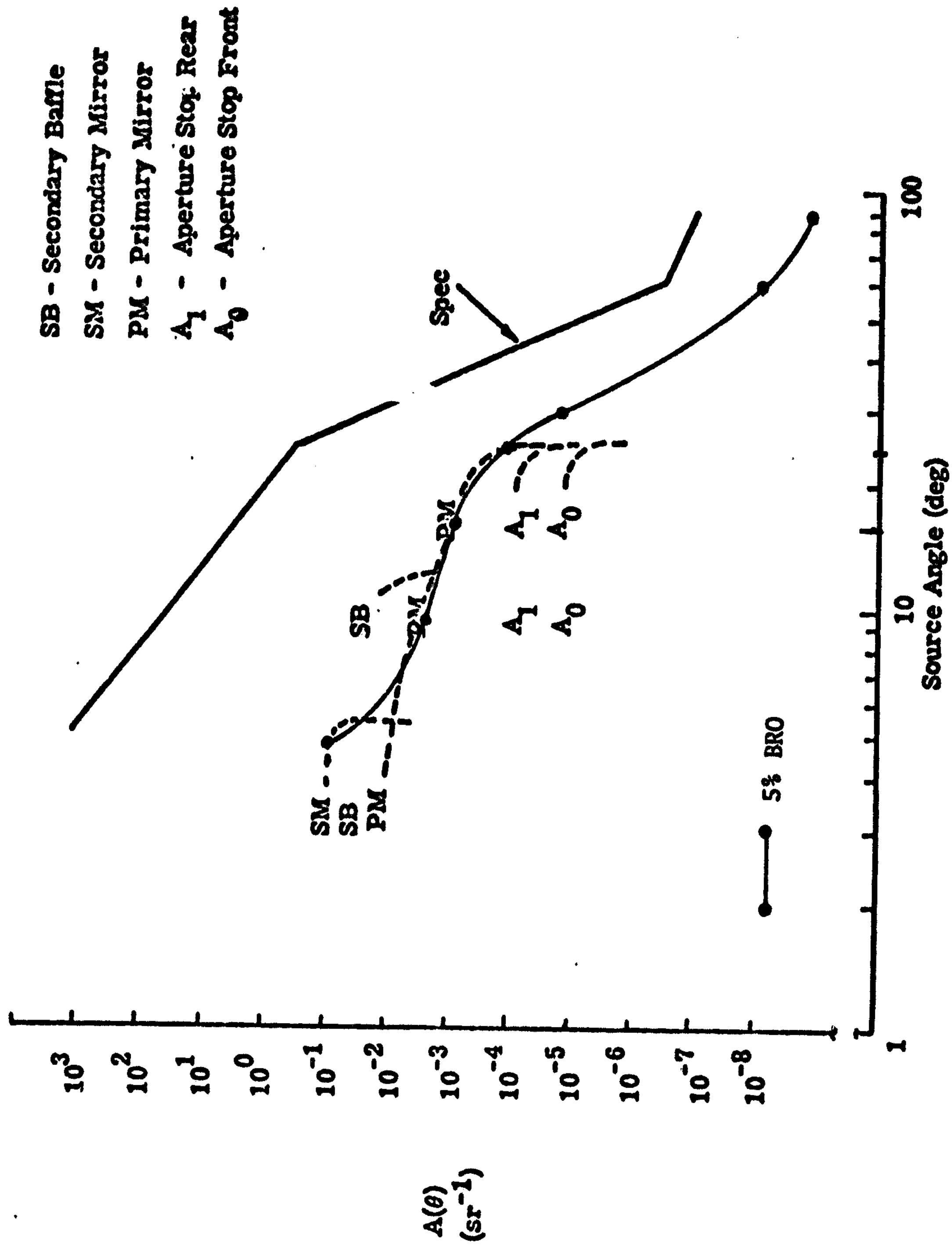

Fig. 8. Visible First-order Scatter, PE Data.

seen from the image did not receive direct illumination, thus, the hand calculation appears to be in error.

Figure 9 is a very simplified drawing of the rays that can reach the secondary baffle. The main baffle tube blocks out all the radiation to the sections on the secondary baffle that can be seen directly.

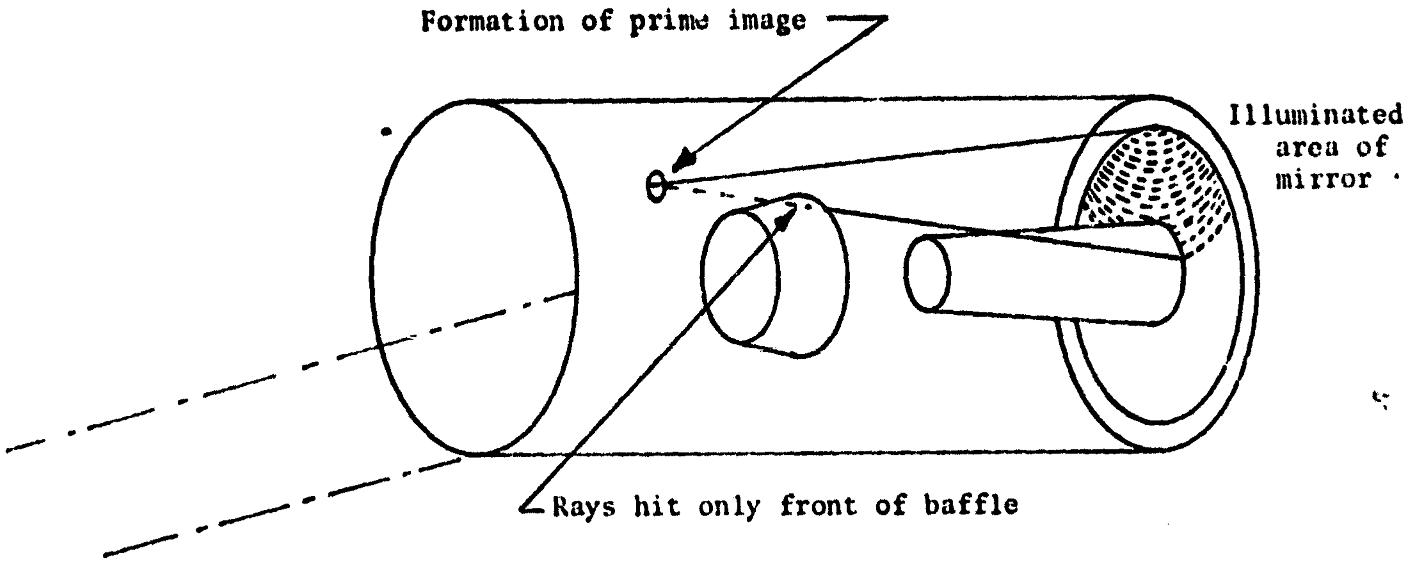

Fig. 9. The Left Sections of the Secondary Baffle do not Receive Direct Illumination.

There is one last point to discuss in the comparative analysis of the visible band results. This APART analysis predicts the contributions from the front side and back side of the aperture stop is the reverse of that presented by PE. The magnitude of the power contributed also appears to be reversed. Only a small portion of the back surface can receive radiation compared to the entire front surface, which is seen directly. With Lambertian coatings, then, the front side must contribute more.

<u>2.1.2. The 8-15μ IR Band</u>. The OSS was evaluated for its off-axis rejection using a 5% Lambertian diffuse coating. The mirror coating had

a BRDF of 1.75 E-3 at $\beta-\beta_o$ = .01 with β^{-1} falloff. β_o is the sine of the angle of incidence, while β is the sine of the angle from the surface normal to the observation point. Table 4 shows the contributions from each object. One can readily see that the mirror scatter plays a secondary rold in the IR. In this analysis, it is by definition (and generally accepted as a true statement) that mirror scatter goes down with increasing wavelength. Therefore, unless the BRDF of the black surfaces also decrease with wavelength, one should not expect significantly better off-axis rejection at the longer wavelengths.

The major contributors are the inner-secondary baffle, the aperture stop, and the inner-primary conical baffle. Note that the back side of the strut contributes only 5.6% of the total energy and that is only at one angle. The orientation of the struts is shown in Figs. 10 and 11. In particular, one of the struts is aligned with the peak of the sun-shield tip. The values calculated in this analysis have the strut and the off-axis point source in the same plane. For small off-axis angles the unwanted radiation is (nearly) focused onto the strut, making this azimuth the worst case.

Table 5 shows the same analysis but with Martin Black on the baffle surfaces. As was the case with the analysis in the visible band, the percentage numbers vary but the same objects are critical to the system's performance. This is due to the variation in the forward and backward scatter characteristics. In most cases this shifts the percent contributed from a back scatter path to the forward scatter path. Figure 12 shows the relative A(θ) values for the two runs along with the specification. The Martin Black A(θ) values are more often below the IRAS 8-15μ spec line.

Table 4. Power Contribution Table (10.6 Microns 5% Coating).

Percent of Power Contributed by Each Object as a Function of Off-axis Source Position

OBJECTS/	OFF AXIS POSITION 1	2	3	4	5	6	7
1 SHIELD TIP	0.0	0.0	0.0	0.0	0.0	0.0	0.0
2 OUTER SHIELD	0.0	0.0	0.0	0.0	0.0	0.0	0.0
3 RADIATOR	0.0	0.0	0.0	0.0	0.0	0.0	0.0
4 ENTRANCE APT TIP	0.0	0.0	0.0	0.0	0.0	0.0	0.0
5 OUTER MAIN BAFFLE	0.0	0.0	0.0	0.0	0.0	0.0	0.0
6 MIDDLE MAIN BAFFLE	0.0	0.0	0.0	0.0	0.0	0.0	0.0
7 MIDDLE RIGHT END	0.0	0.0	0.0	0.0	0.0	0.0	0.0
8 INNER MAIN BAFFLE	0.0	0.0	0.0	0.0	0.0	0.0	0.0
9 INNER RIGHT END	0.0	0.0	0.0	0.0	0.0	0.0	0.0
10 RIGHT OF 9	0.0	0.0	0.0	0.0	0.0	0.0	0.0
11 LEFT APT CONE	.0	4.6	14.7	29.6	3.4	.7	.5
12 LEFT APERTURE	.5	36.8	58.5	70.1	2.5	.7	2.4
13 APERTURE STOP	0.0	0.0	0.0	0.0	0.0	0.0	0.0
14 RIGHT APERTURE	0.0	0.0	24.7	0.0	0.0	0.0	0.0
15 RIGHT APT CONE	0.0	0.0	0.0	0.0	0.0	0.0	0.0
16 SEC HOUSING	0.0	0.0	0.0	0.0	0.0	0.0	0.0
17 OUTER SEC. BAFF	0.0	0.0	0.0	0.0	0.0	0.0	0.0
18 SEC. BAFF TIP	0.0	0.0	0.0	0.0	0.0	0.0	0.0
19 INNER SEC BAFFLE	73.0	45.5	0.0	0.0	87.7	16.3	74.6
20 INNER SEC TIP	25.7	0.0	0.0	0.0	4.1	3.8	17.9
21 STRUT BACK	.2	5.6	0.0	0.0	1.4	.4	2.1
22 OUTER CONICAL	0.0	0.0	0.0	0.0	0.0	0.0	0.0
23 CENTERAL OBSCUR	.1	4.7	0.0	0.0	.5	.1	.5
24 CENT OBSCUR TIP	0.0	0.0	0.0	0.0	0.0	0.0	0.0
25 OUTER CONICAL TIP	0.0	0.0	0.0	0.0	0.0	0.0	0.0
26 LEFT INNER CONICAL	0.0	0.0	0.0	0.0	.1	.9	.2
27 MIDDLE INNER CONICAL	0.0	0.0	0.0	0.0	.1	76.8	1.2
28 RIGHT INNER CONICAL	0.0	0.0	0.0	0.0	0.0	0.0	0.0
29 INNER CONICAL END	0.0	0.0	0.0	0.0	0.0	0.0	0.0
30 IMAGE BAFFLE	0.0	0.0	0.0	0.0	0.0	0.0	0.0
31 IMAGE	0.0	0.0	0.0	0.0	0.0	0.0	0.0
32 SECONDARY MIRROR	.4	0.0	0.0	0.0	.0	.1	.3
33 PRIMARY MIRROR	.1	2.9	2.0	.3	.2	.1	.5
34 ENTRANCE PORT	0.0	0.0	0.0	0.0	0.0	0.0	0.0
35 PRIM MIRROR AS DISK	0.0	0.0	0.0	0.0	0.0	0.0	0.0
36 POINT SOURCE	0.0	0.0	0.0	0.0	0.0	0.0	0.0
TOTAL POWER	.480E-01	.627E-03	.218E-03	.871E-04	.117E-04	.517E-08	.249E-10
SOURCE ANG	5.0	10.0	17.0	24.0	30.0	60.0	88.0

* Infrared Astonomical Satellite (IRAS)

* Scattered Light Analysis of OSS

*Perkin-Elmer Design Number 693-10000 Revision E of 5/9/78

* Units are cm Bro

ORIGINAL PAGE IS OF POOR QUALITY

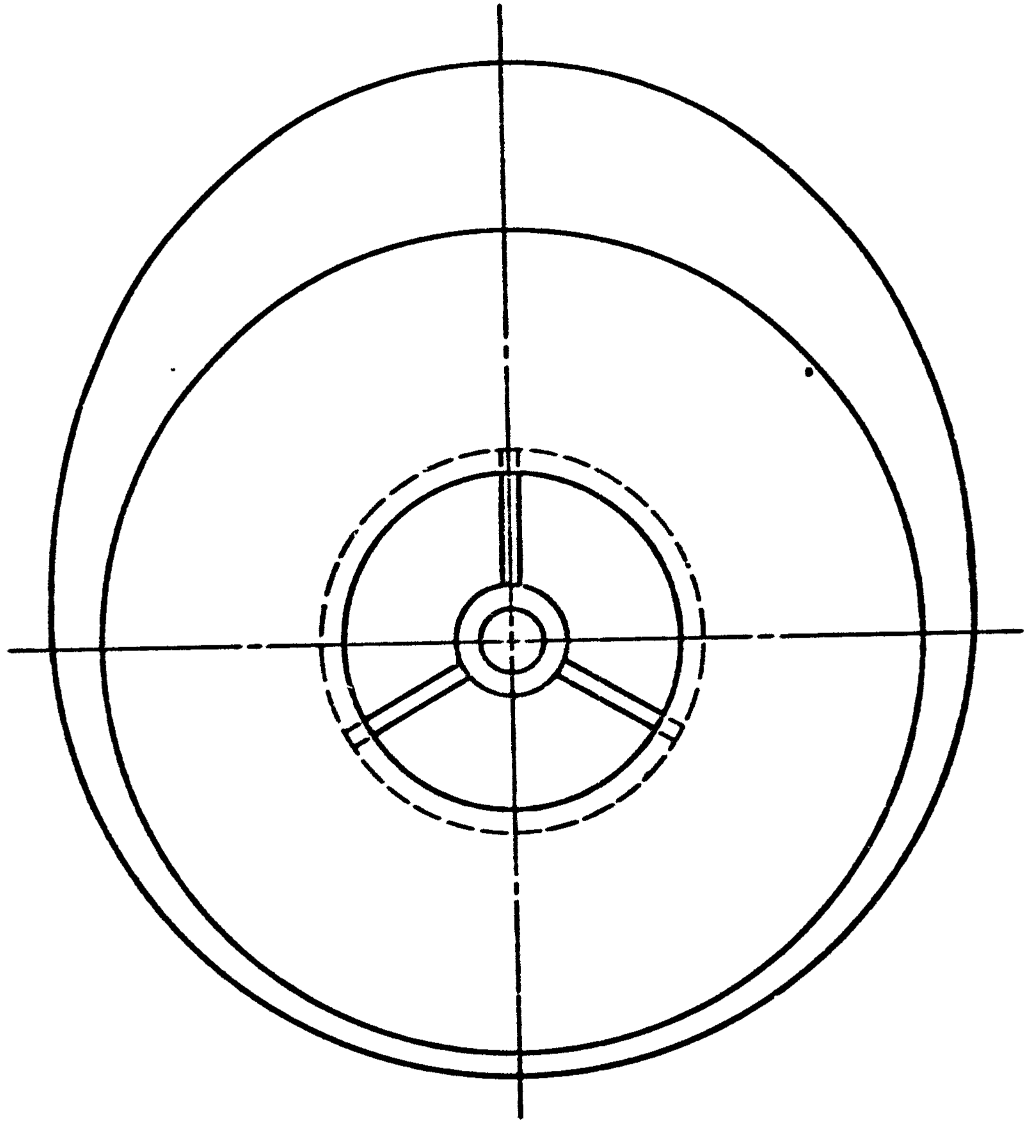

Fig. 10. Strut Orientation of the IRAS System.

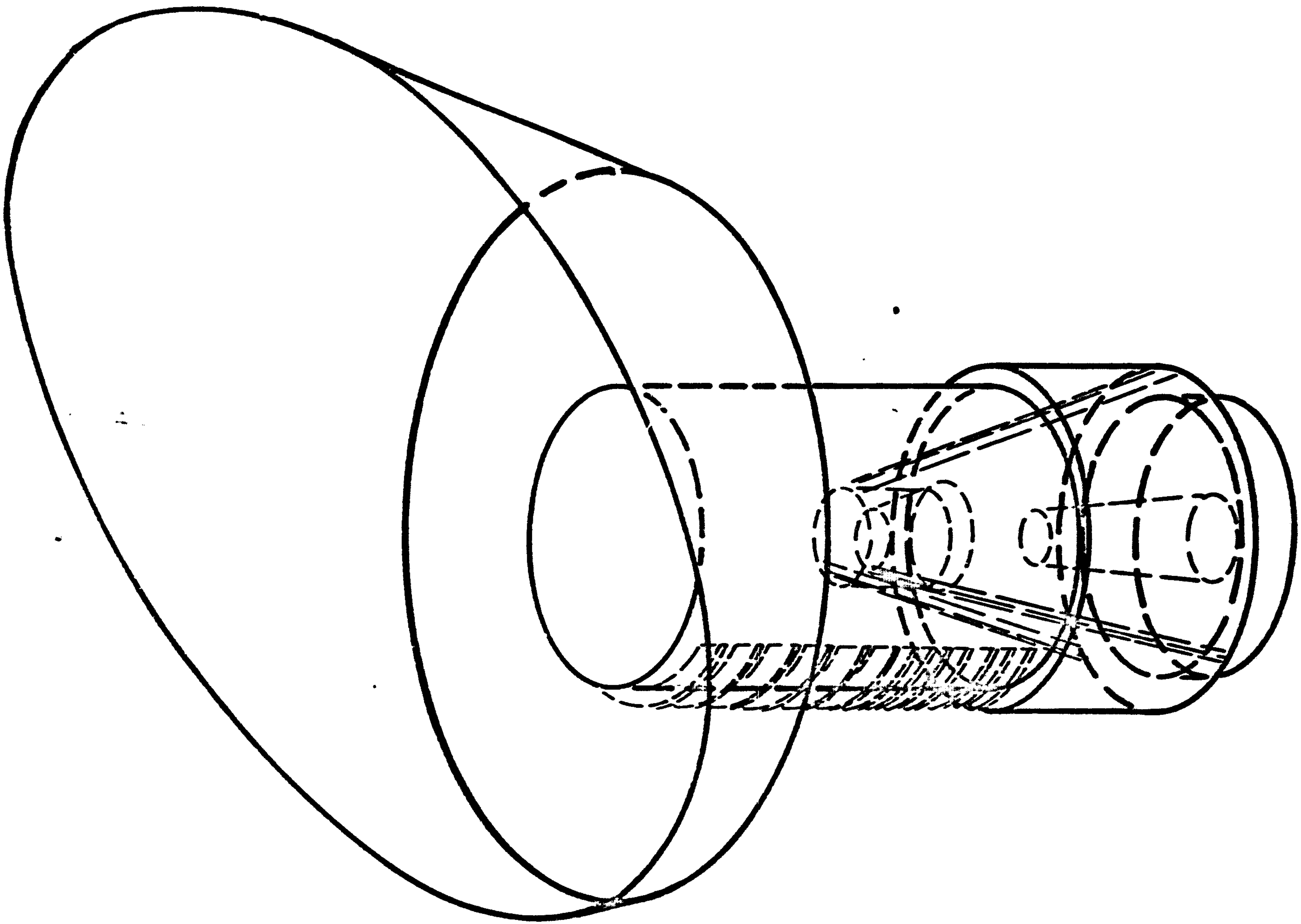

Fig. 11. Model of IRAS Used in the APART Calculations with Vanes and Profile of Sunshade.

Table 5. Power Contribution Table (10.6 Microns Martin Black).

Percent of Power Contributed by Each Object as a Function of Off-axis Source Position

OBJECTS	OFF AXIS POSITION 1	2	3	4	5	6	7
1 SHIELD TIP	0.0	0.0	0.0	0.0	0.0	0.0	0.0
2 OUTER SHIELD	0.0	0.0	0.0	0.0	0.0	0.0	0.0
3 RADIATOR	0.0	0.0	0.0	0.0	0.0	0.0	0.0
4 ENTRANCE APT TIP	0.0	0.0	0.0	0.0	0.0	0.0	0.0
5 OUTER MAIN BAFFLE	0.0	0.0	0.0	0.0	0.0	0.0	0.0
6 MIDDLE MAIN BAFFLE	0.0	0.0	0.0	0.0	0.0	0.0	0.0
7 MIDDLE RIGHT END	0.0	0.0	0.0	0.0	0.0	0.0	0.0
8 INNER MAIN BAFFLE	0.0	0.0	0.0	0.0	0.0	0.0	0.0
9 INNER RIGHT END	0.0	0.0	0.0	0.0	0.0	0.0	0.0
10 RIGHT OF 9	0.0	0.0	0.0	0.0	0.0	0.0	0.0
11 LEFT APT CONE	.0	.0	9.9	25.1	.0	.0	.0
12 LEFT APERTURE	.0	.2	46.7	70.5	.0	.0	.3
13 APERTURE STOP	0.0	0.0	0.0	0.0	0.0	0.0	0.0
14 RIGHT APERTURE	0.0	0.0	20.4	0.0	0.0	0.0	0.0
15 RIGHT APT CONE	0.0	0.0	0.0	0.0	0.0	0.0	0.0
16 SEC HOUSING	0.0	0.0	0.0	0.0	0.0	0.0	0.0
17 OUTER SEC. BAFF	0.0	0.0	0.0	0.0	0.0	0.0	0.0
18 SEC. BAFF TIP	0.0	0.0	0.0	0.0	0.0	0.0	0.0
19 INNER SEC BAFFLE	97.0	95.6	0.0	0.0	90.6	1.5	77.2
20 INNER SEC TIP	2.3	0.0	0.0	0.0	.0	.0	2.2
21 STRUT BACK	.0	.0	0.0	0.0	.4	.0	.2
22 OUTER CONICAL	0.0	0.0	0.0	0.0	0.0	0.0	0.0
23 CENTERAL OBSCUR	.0	.0	0.0	0.0	.2	.0	.1
24 CENT OBSCUR TIP	0.0	0.0	0.0	0.0	0.0	0.0	0.0
25 OUTER CONICAL TIP	0.0	0.0	0.0	0.0	0.0	0.0	0.0
26 LEFT INNER CONICAL	0.0	0.0	0.0	0.0	.4	.1	2.0
27 MIDDLE INNER CONICAL	0.0	0.0	0.0	0.0	2.1	98.3	16.8
28 RIGHT INNER CONICAL	0.0	0.0	0.0	0.0	0.0	0.0	0.0
29 INNER CONICAL END	0.0	0.0	0.0	0.0	0.0	0.0	0.0
30 IMAGE BAFFLE	0.0	0.0	0.0	0.0	0.0	0.0	0.0
31 IMAGE	0.0	0.0	0.0	0.0	0.0	0.0	0.0
32 SECONDARY MIRROR	.5	0.0	0.0	0.0	.0	.0	.5
33 PRIMARY MIRROR	.2	.2	23.0	4.3	6.3	.0	.8
34 ENTRANCE PORT	0.0	0.0	0.0	0.0	0.0	0.0	0.0
35 PRIM MIRROR AS DISK	0.0	0.0	0.0	0.0	0.0	0.0	0.0
36 POINT SOURCE	0.0	0.0	0.0	0.0	0.0	0.0	0.0
TOTAL POWER	.366E-01	.983E-02	.194E-04	.615E-05	.731E-05	.321E-07	.154E-10
SOURCE ANG	5.0	10.0	17.0	24.0	30.0	60.0	80.0

* Infrared Astonomical Satallite (IRAS)
* Scattered Light and Diffraction Analysis
* For Ames Research Center NASA Jun 21, 1978
* Units are cm Bro

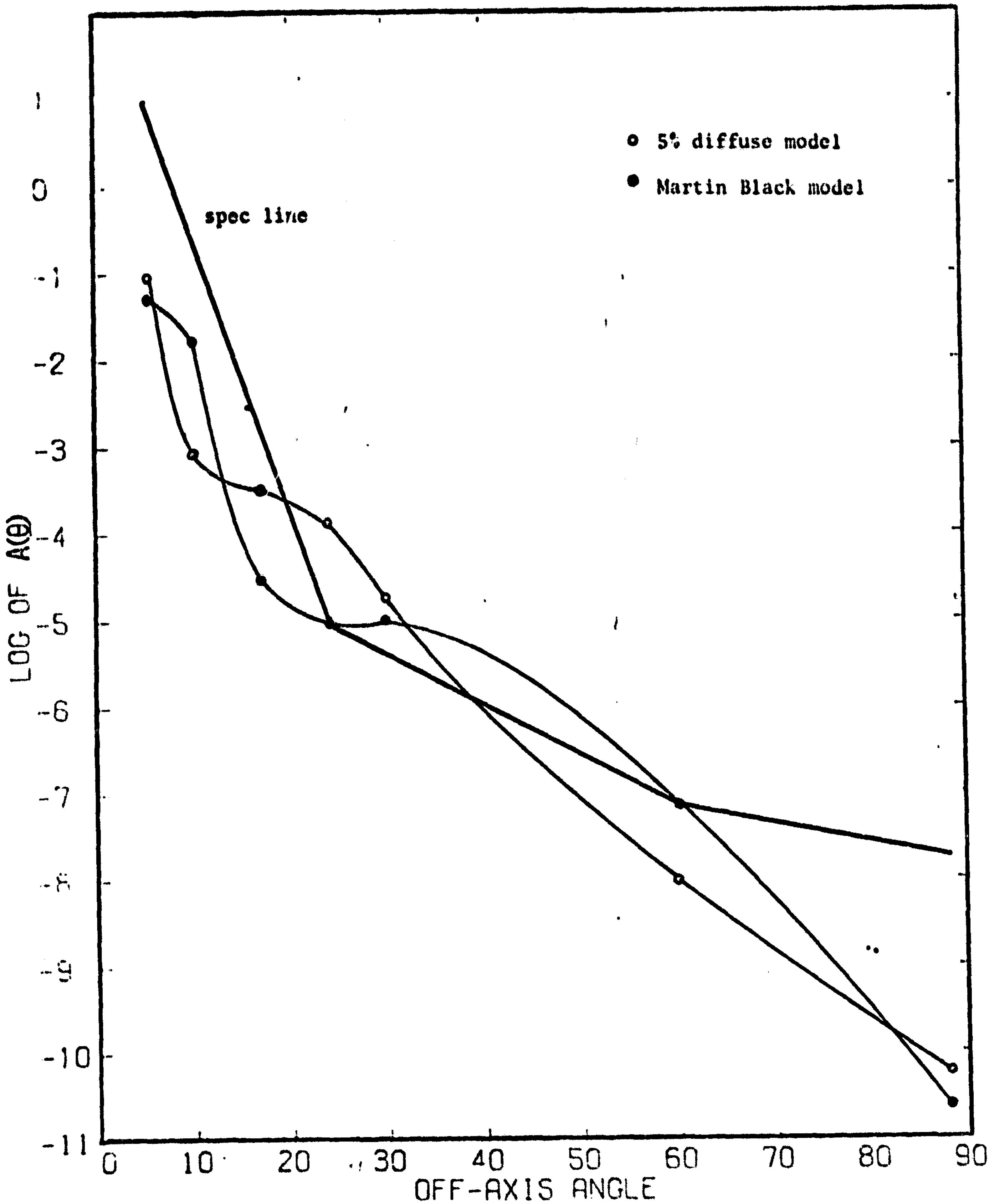

Fig. 12. A(θ) for 8 - 15μ Band of OSS.

Figure 13 compares the PE results with the 5% results. The contribution calculated by PE, as indicated by the dashed line at 10 degrees, is much higher. The contribution from the front side of the aperture is about 10% higher than predicted by PE for the back side. These are the same values as calculated in the visible, because the 5% black hasn't changed with wavelength.

2.1.3. Black Coatings at Long Wavelengths. When the Martin Black coating was used to evaluate the OSS in the 8-15μ band, the predicted values were, in several cases, above the 8-15μ spec line. At the longer wavelengths the spec line moves down to lower rejection values. However, existing data indicates that the hemispherical diffuse reflectivity increases with wavelength (Fig. 14). This implies that at some off-axis angles A(θ) will be above the spec lines for all the IR bands.

The above statement must be tempered with the following additional statements: Other measured data[9] exists which indicates that the increase is not as pronounced (Fig. 15). At the longer wavelengths the surface roughness relative to the wavelength, is much less. As with the mirrors one might suspect that the diffuse BRDF should drop significantly while the specular component will increase. It is not known whether the data in Fig. 14 includes both the specular and diffuse component.

In any case, it is imperative to have measured BRDF data as a function of the input and output angles. Such data is not presently available for the wavelengths above 10.6μ. Without it, the validity of the evaluations at the longer wavelengths is questionable.

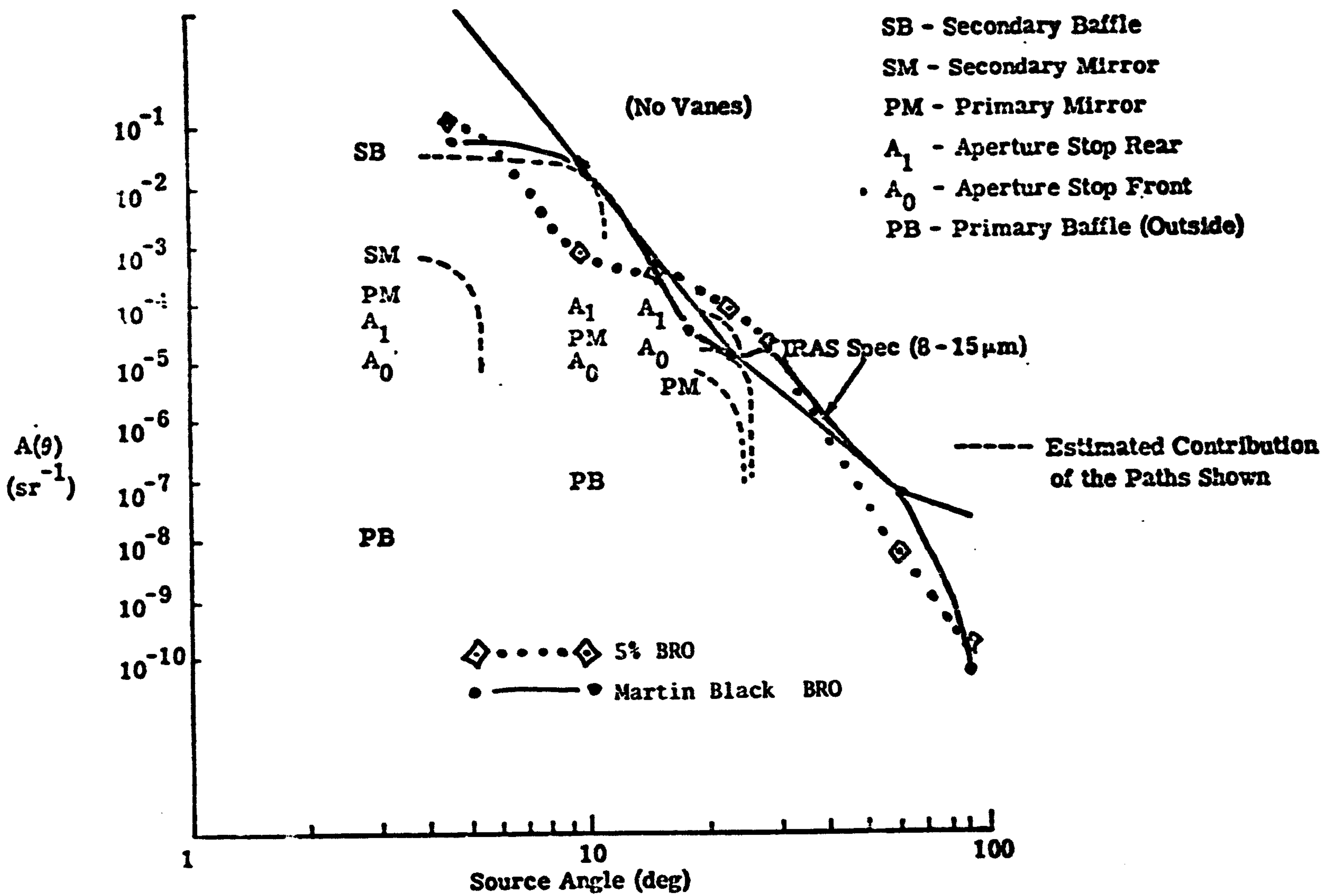

Fig. 13a. First Order Scatter (5% Diffuse Reflectance on Baffles).

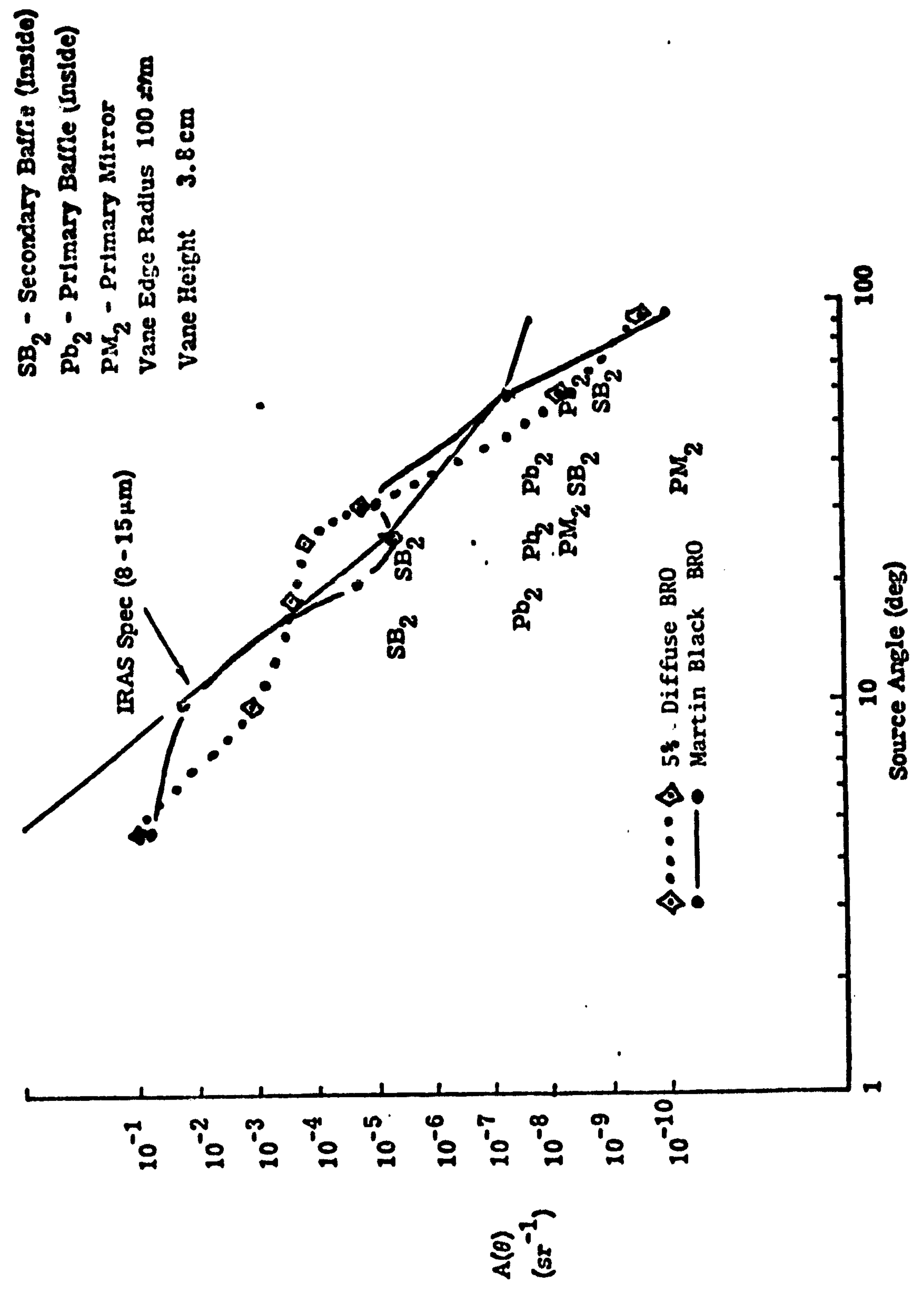

Fig. 13b. Second-order Scatter (5% Diffuse Reflectance, Vanes in Barrel Baffle Front).

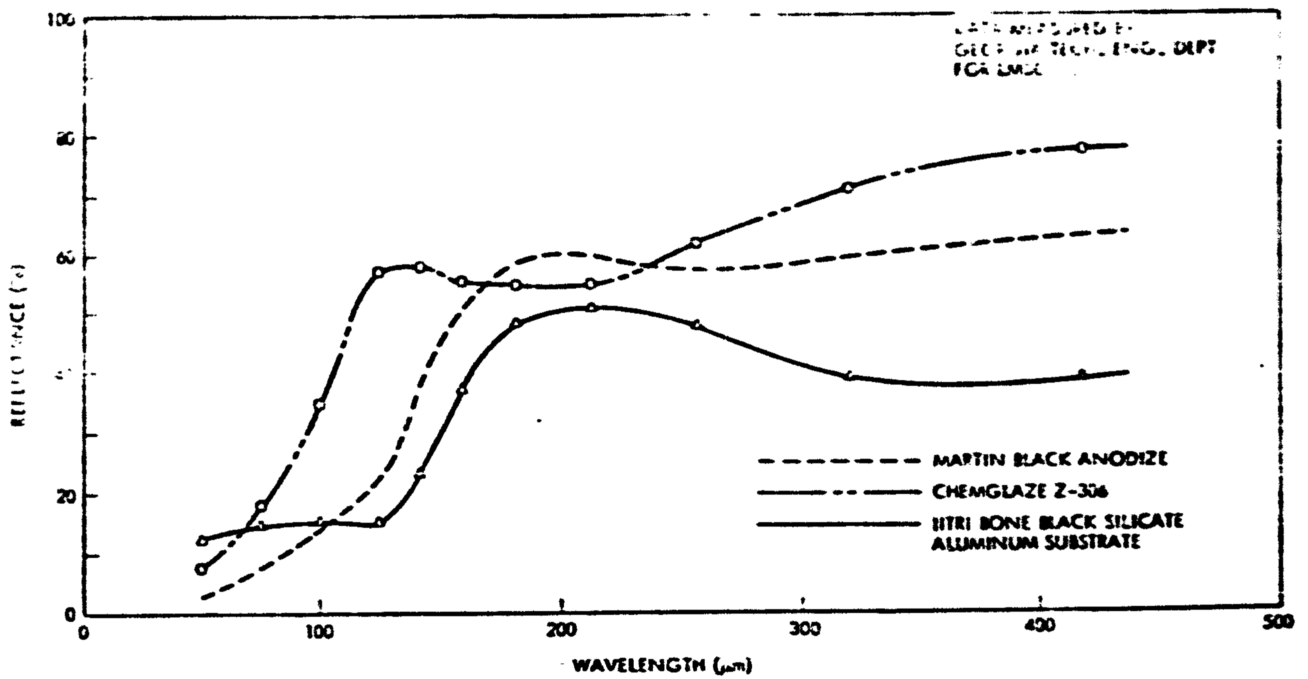

Fig. 14. Hemispherical Diffuse Measurements as a Function of λ.[8]

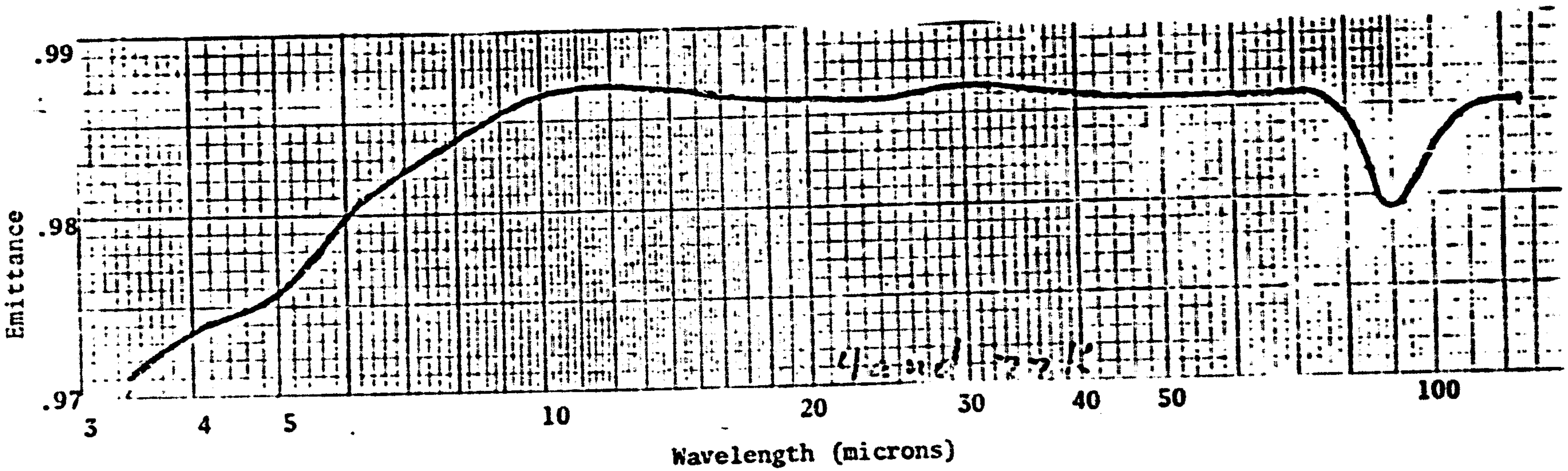

Fig. 15. Martin's Data on Martin Black for Long Wavelengths.[9]

In the analysis of the flight system, discussed later in this report, it will be assumed that the BRDF profiles at all wavelengths remain the same, only the magnitude varies with wavelength as indicated in Fig. 14.

If, as discussed above, the coating exhibits a marked specular reflection at the longer wavelengths, this could significantly alter the predicted attenuation factors. Most likely the specular component will not be a delta function but exhibit a relatively high BRDF over a fairly large solid angle ($\approx .02\ sr^{-1}$). Under such circumstances, the forward scatter from the secondary baffle towards the secondary mirror would be significantly higher and specular reflections from the inner conical baffle towards the field mask would cause additional problems for large off-axis angles. It would then be desirable to eliminate all possible near-specular paths.

3.0 SUNSHIELD ANALYSIS

This portion of the analysis was performed in two stages. In this section the characteristics of the sunshield itself will be explored. The overall effect of the sunshield will be discussed later as part of the evaluation of the overall flight system design.

The sunshield design can be seen in Fig. 10. Figure 16 shows a profile of the shield. The design of the shield has been detailed elsewhere;[10] basically it blocks sunlight for off-axis angles greater than 60° when the sun is in the plane of the tip of the cone. Earth light is rejected at 88° for off-axis angles in the opposite direction.

The underside of the sunshield has a specular surface to reduce the thermal loading on the telescope. When the unwanted source is more than

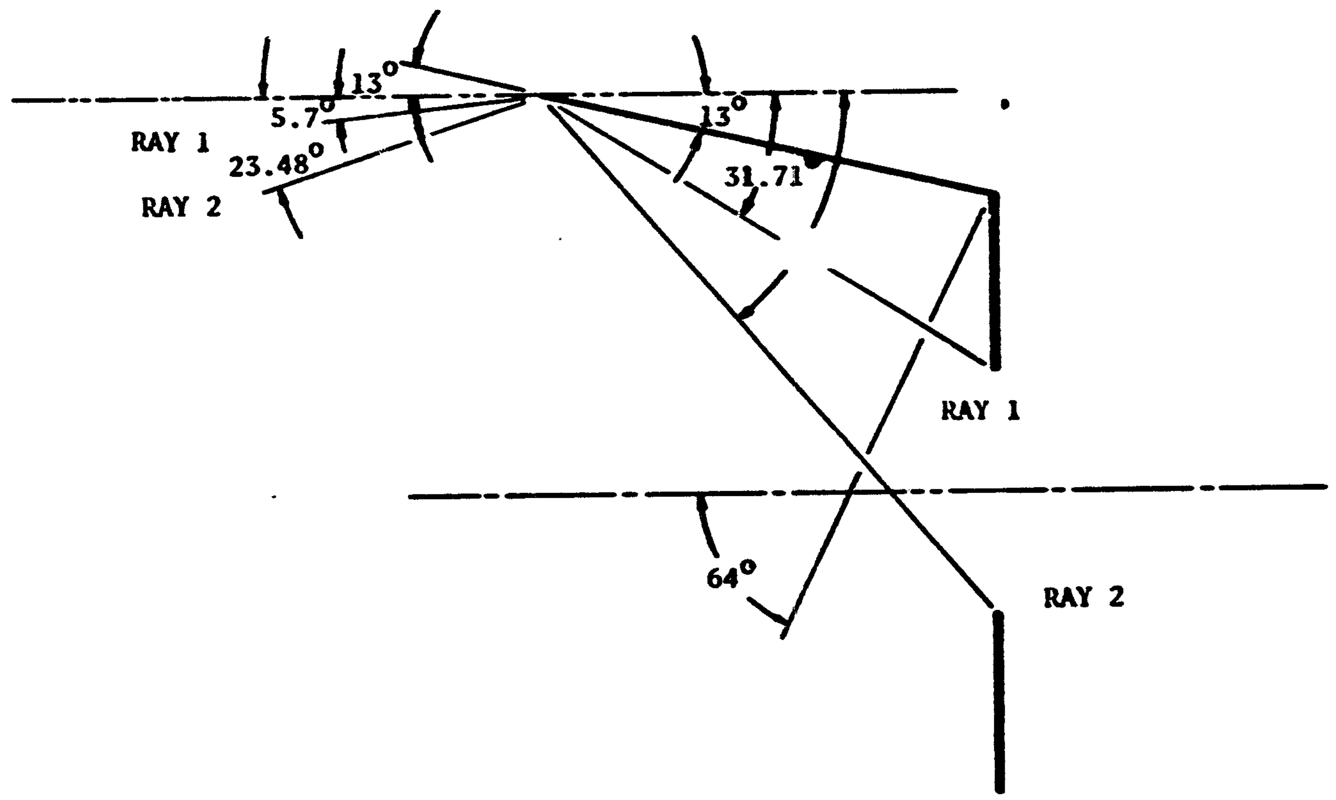

Fig. 16. Specular Reflections off the Sunshield.

64° off axis only diffuse scatter and self-emitted radiation will enter the main tube. For specular surfaces, the emissivity is low and the diffuse scatter is low, hence the heat load will be low and the attenuation high.

However, at small off-axis angles unwanted light is specularly reflected into the main tube, increasing the heat load and the A(θ) values. The problem is three-dimensional, but Fig. 16 will help to clarify the problem. Ray 1 from a source 5.7° off-axis will just reach the entrance part of the main tube. So the increase to the specular reflected energy should start at quite small off axis angles. Ray 2 is from a source 23.48° off-axis. Beyond this angle, specular paths do not enter the entrance port and the input energy will fall off.

The three dimensional nature of the problem also causes skew rays to be focused into the system. To analyze the problem quickly, several scale models of the sunshield were made using specularly coated Mylar. Transmittance measurements were made as a function of the off-axis position of the source (Fig. 17). The peak input power is for a source point 25° off axis as shown in Table 6. This is very unfortunate because the A(θ) for the OSS is just slightly above the specification for off axis angles of 24-60° when the system was evaluated using Martin Black. The sunshield will cause the values to go even higher.

By changing the angle of the sunshield, the peak value due to specular reflection may be moved to a less obnoxious off-axis angle. Depending on how this is done, it will usually affect moments of inertia and/or the radiators that presently exist.

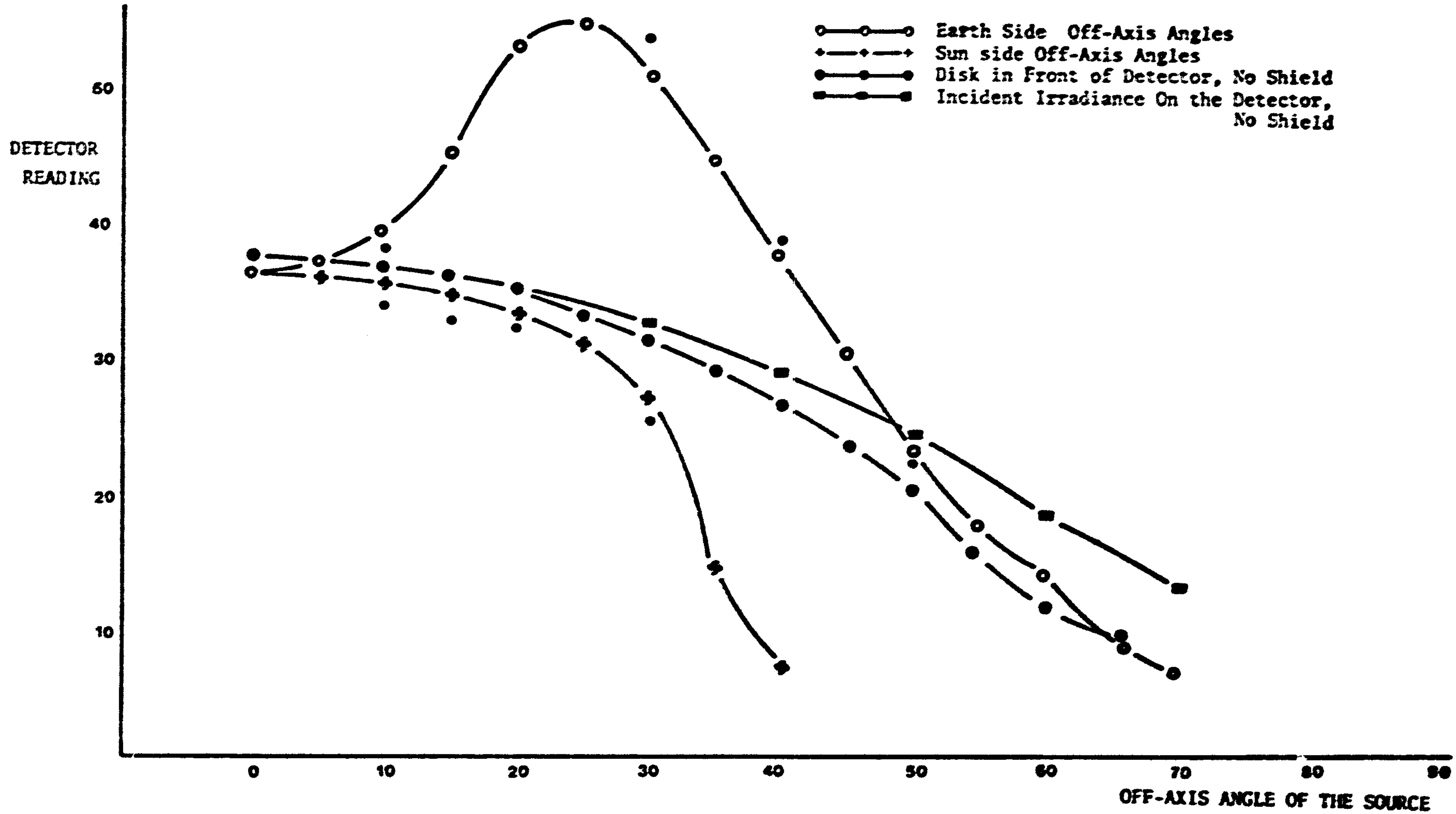

Fig. 17. Measured Performance of the Sunshield Model.

Table 6. Data from Measurements on a Sample Sunshade.

Off-axis Angle	F
0	1.00
5	1.03
10	1.10
15	1.29
20	1.59
25	1.69
30	1.64
35	1.51
40	1.40
45	1.18
50	.99

$\phi_{IN} = \phi_o * F$

ϕ_{IN} is the power into the main baffle sections

ϕ_o is the power into the system without the sunshield

4.0 FIELD MASK AND LENSES

To analyze the effects of the field stop and the field optics, a single detector was selected and located on axis. The field of view from the detector was calculated using ACCOS by running rays from the edge of the detector surface backwards through the lens, and using the field stop as the limiting aperture for the rays, determining the direction they leave the field-optics set. This was done for the band 1 field-lens assembly with the data as supplied by Ball Brothers Research Corporation in a 16 May 1978 letter number 86563.78.0.0038. A picture of this process is shown in Fig. 18. From this data, it was determined that the transfers from the objects along the inside of the inner primary-mirror baffle could not reach the detector (Objects 26, 27, 28, and 30). These transfers were eliminated from the analysis for the IR single detector.

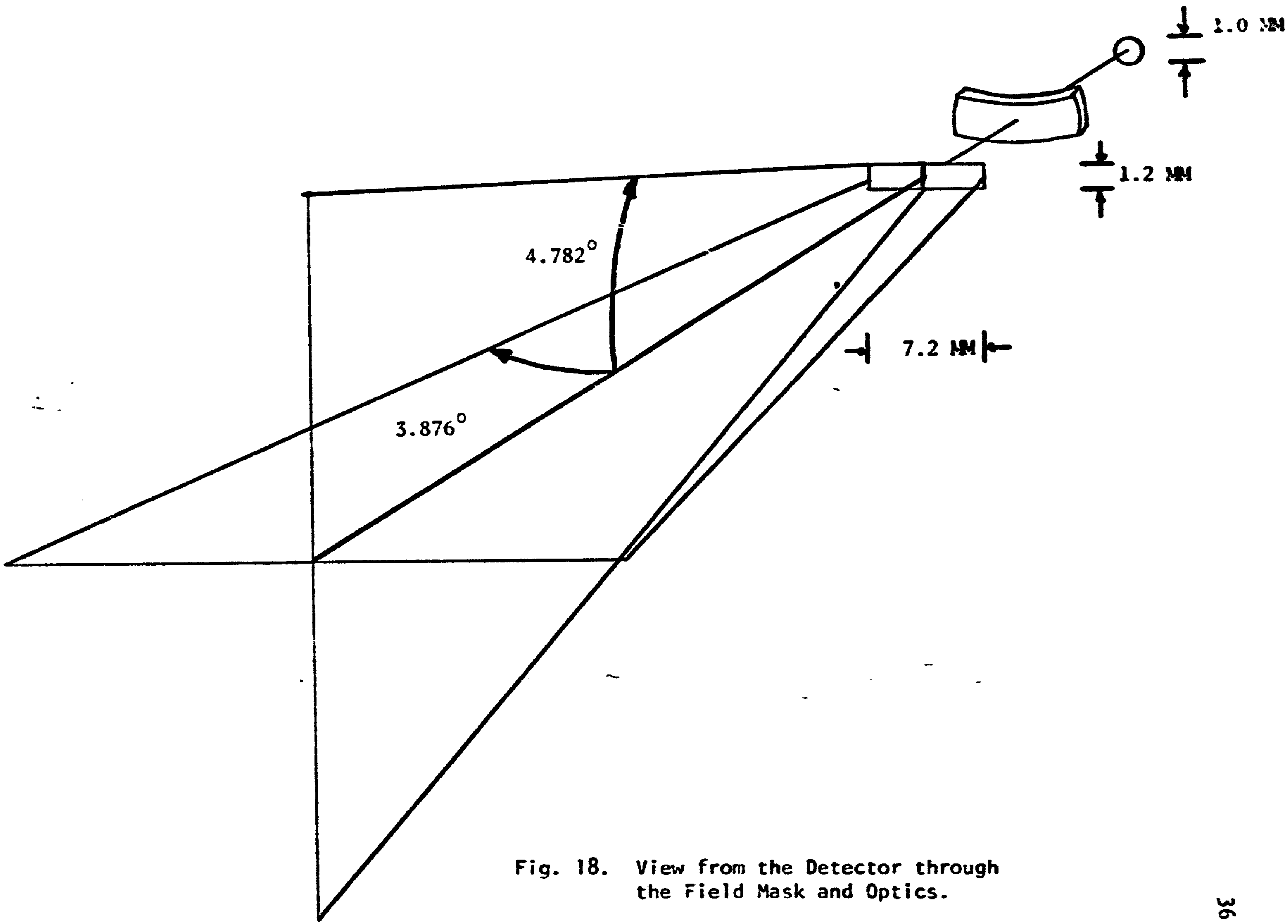

Fig. 18. View from the Detector through the Field Mask and Optics.

The field stop is oversized allowing all the stray radiation from the secondary mirror (object 32) and objects imaged through it to reach the detector. These transfers were changed to account for the smaller size detector rather than the whole image surface. The limiting field of view from the detector casts an elliptical-shaped hole onto the inner-secondary baffle. To model this transfer, the size of the elliptical aperture projected out to the secondary baffle was determined and entered as an obscuration in APART, with the detector being modeled as a rectangular disk.

4.1 DIFFRACTION EFFECTS

The size of the field stops must be oversized because they are in the far-field diffraction region of the system aperture stop. The field stops are, however, not in the far-field region for power transfers coming directly from the inner-secondary baffle, where here we must consider near-field diffraction from a linear edge. In this case, the light rays diffracted around the edge will be of secondary importance compared to the direct rays near the edge which will pass undiffracted to the detector. The inner-secondary baffle is the only object in which edge diffraction would produce any measurable contribution.

5.0 ANALYSIS OF THE FLIGHT DESIGN

The preliminaries of the scattered-light analysis on the flight design have been considered. What remains is the scatter and diffraction analysis on the flight-design system as a whole. This section contains the stray-light analysis of the flight system including the OSS, sunshield, field mask and lenses. The diffraction analysis will be presented in the next section.

5.1 SYSTEM MODEL

The physical size and shape of the objects are shown in Figs. 1, 2, and 3, except for the detector area which is shown in Fig. 18.

The BRDF values of the mirrors are according to PE's formula as described in Appendix A. By definition, there is no wavelength scaling with the 5% diffuse surface. When Martin Black is used the values and profiles remain constant except for the 100 micron band. In this band the BRDF profile is ASSUMED to remain the same while the magnitude is increased by a factor of 10. This results in an increase in the A(θ) of 10^N where N is the number of Martin Black-surface scatters encountered.

The scattered light from the sunshield becomes a factor only for very large off-axis angles (≥88°). The specular component is of no consequence at these angles. No measured BRDF values were available for this surface, therefore it was assigned a Lambertian diffuse component of .001 for all wavelengths. At these angles the sunshield is the only surface that is directly illuminated so the A(θ) values will scale directly with the sunshields surface scatter. The .001 BRDF yields A(θ) values well below the spec line and, as will be seen, diffraction effects predominate at these large off-axis angles.

5.2 SCATTERED LIGHT ANALYSIS 0.4-0.9 BAND

The contribution of power from each object to the image plane is shown in Tables 7 and 8, for the 5% and Martin Black coatings respectively.

At 5° the direct scatter from the directly illuminated primary and secondary mirrors are the major sources of scattered light.

Table 7. % Table for .4-.9μ Band with 5% Diffuse for Flight System.

PERCENT OF POWER CONTRIBUTED
BY EACH OBJECT AS A FUNCTION
OF OFF AXIS SOURCE POSITION

OBJECTS/	OFF AXIS POSITION 1	2	3	4	5	6	7	8	9
1 SHIELD TIP	0.0	0.0	0.0	0.0	0.0	0.0	0.0	0.0	0.0
2 OUTER SHIELD	0.0	0.0	0.0	0.0	0.0	0.0	0.0	0.0	0.0
3 RADIATOR	0.0	0.0	0.0	0.0	0.0	0.0	0.0	0.0	0.0
4 ENTRANCE APT TIP	0.0	0.0	0.0	0.0	0.0	0.0	0.0	0.0	0.0
5 OUTER MAIN BAFFLE	0.0	0.0	0.0	0.0	0.0	0.0	0.0	0.0	0.0
6 MIDDLE MAIN BAFFLE	0.0	0.0	0.0	0.0	0.0	0.0	0.0	0.0	0.0
7 MIDDLE RIGHT END	0.0	0.0	0.0	0.0	0.0	0.0	0.0	0.0	0.0
8 INNER MAIN BAFFLE	0.0	0.0	0.0	0.0	0.0	0.0	0.0	0.0	0.0
9 INNER RIGHT END	0.0	0.0	0.0	0.0	0.0	0.0	0.0	0.0	0.0
10 RIGHT OF 9	0.0	0.0	0.0	0.0	0.0	0.0	0.0	0.0	0.0
11 LEFT APT CONE	0.0	0.0	0.0	0.0	0.0	0.0	0.0	0.0	0.0
12 LEFT APERTURE	0.0	0.0	7.4	36.5	0.0	0.0	0.0	0.0	0.0
13 APERTURE STOP	0.0	0.0	0.0	0.0	0.0	0.0	0.0	0.0	0.0
14 RIGHT APERTURE	0.0	0.0	4.7	0.0	0.0	0.0	0.0	0.0	0.0
15 RIGHT APT CONE	0.0	0.0	0.0	0.0	0.0	0.0	0.0	0.0	0.0
16 SEC HOUSING	0.0	0.0	0.0	0.0	0.0	0.0	0.0	0.0	0.0
17 OUTER SEC. BAFF	0.0	0.0	0.0	0.0	0.0	0.0	0.0	0.0	0.0
18 SEC. BAFF TIP	0.0	0.0	0.0	0.0	0.0	0.0	0.0	0.0	0.0
19 INNER SEC BAFFLE	27.9	3.9	0.0	6.5	66.3	10.6	14.9	14.2	14.4
20 INNER SEC TIP	13.5	0.0	0.0	0.0	0.0	0.0	0.0	0.0	0.0
21 STRUT BACK	0.0	0.0	0.0	0.0	0.0	0.0	0.0	0.0	0.0
22 OUTER CONICAL	0.0	0.0	0.0	0.0	0.0	0.0	0.0	0.0	0.0
23 CENTERAL OBSCUR	0.0	0.0	0.0	0.0	0.0	0.0	0.0	0.0	0.0
24 CENT OBSCUR TIP	0.0	0.0	0.0	0.0	0.0	0.0	0.0	0.0	0.0
25 OUTER CONICAL TIP	0.0	0.0	0.0	0.0	0.0	0.0	0.0	0.0	0.0
26 LEFT INNER CONICAL	0.0	0.0	0.0	0.0	0.0	0.0	0.0	0.0	0.0
27 MIDDLE INNER CONICAL	0.0	0.0	0.0	0.0	1.5	61.5	48.1	51.4	52.6
28 RIGHT INNER CONICAL	0.0	0.0	0.0	0.0	0.0	0.0	0.0	0.0	0.0
29 INNER CONICAL END	0.0	0.0	0.0	0.0	0.0	0.0	0.0	0.0	0.0
30 IMAGE BAFFLE	0.0	0.0	0.0	0.0	0.0	0.0	0.0	0.0	0.0
31 IMAGE	0.0	0.0	0.0	0.0	0.0	0.0	0.0	0.0	0.0
32 SECONDARY MIRROR	32.0	0.0	0.0	0.0	.2	11.2	14.6	12.4	10.4
33 PRIMARY MIRROR	26.6	96.1	87.9	57.0	31.9	16.7	22.4	22.1	22.6
34 POINT SOURCE	0.0	0.0	0.0	0.0	0.0	0.0	0.0	0.0	0.0
TOTAL POWER	.937E-04	.730E-05	.187E-05	.181E-06	.204E-07	.317E-09	.856E-13	.658E-13	.345E-13
SOURCE ANG	5.0	10.0	17.0	24.0	30.0	60.0	88.0	98.0	108.0

* INFRARED ASTRONOMICAL SATELLITE (IRAS)
* SCATTERED LIGHT VISIBLE DETECTOR, FIVE PERCENT
* FOR AMES RESEARCH CENTER-NASA JULY 26, 1978
* PERKIN-ELMER DESIGN NUMBER 693-10000 REVISION E OF 5/9/78
* UNITS ARE CM AZIMUTH 180. SRL

ORIGINAL PAGE IS
OF POOR QUALITY

PERCENT OF POWER CONTRIBUTED
BY EACH OBJECT AS A FUNCTION
OF OFF AXIS SOURCE POSITION

OBJECTS/	OFF AXIS POSITION 1	2	3	4	5	6	7	8	9
1 SHIELD TIP	0.0	0.0	0.0	0.0	0.0	0.0	0.0	0.0	0.0
2 OUTER SHIELD	0.0	0.0	0.0	0.0	0.0	0.0	0.0	0.0	0.0
3 RADIATOR	0.0	0.0	0.0	0.0	0.0	0.0	0.0	0.0	0.0
4 ENTRANCE APT TIP	0.0	0.0	0.0	0.0	0.0	0.0	0.0	0.0	0.0
5 OUTER MAIN BAFFLE	0.0	0.0	0.0	0.0	0.0	0.0	0.0	0.0	0.0
6 MIDDLE MAIN BAFFLE	0.0	0.0	0.0	0.0	0.0	0.0	0.0	0.0	0.0
7 MIDDLE RIGHT END	0.0	0.0	0.0	0.0	0.0	0.0	0.0	0.0	0.0
8 INNER MAIN BAFFLE	0.0	0.0	0.0	0.0	0.0	0.0	0.0	0.0	0.0
9 INNER RIGHT END	0.0	0.0	0.0	0.0	0.0	0.0	0.0	0.0	0.0
10 RIGHT OF 9	0.0	0.0	0.0	0.0	0.0	0.0	0.0	0.0	0.0
11 LEFT APT CONE	0.0	0.0	0.0	0.0	0.0	0.0	0.0	0.0	0.0
12 LEFT APERTURE	0.0	0.0	.6	4.2	.0	.0	.0	.0	.0
13 APERTURE STOP	0.0	0.0	0.0	0.0	0.0	0.0	0.0	0.0	0.0
14 RIGHT APERTURE	0.0	0.0	.4	0.0	0.0	0.0	0.0	0.0	0.0
15 RIGHT APT CONE	0.0	0.0	0.0	0.0	0.0	0.0	0.0	0.0	0.0
16 SEC HOUSING	0.0	0.0	0.0	0.0	0.0	0.0	0.0	0.0	0.0
17 OUTER SEC. BAFF	0.0	0.0	0.0	0.0	0.0	0.0	0.0	0.0	0.0
18 SEC. BAFF TIP	0.0	0.0	0.0	0.0	0.0	0.0	0.0	0.0	0.0
19 INNER SEC BAFFLE	26.9	65.6	0.0	4.5	5.7	.2	1.0	.8	.7
20 INNER SEC TIP	1.2	0.0	0.0	0.0	.0	.0	.1	.1	.1
21 STRUT BACK	0.0	0.0	.0	0.0	.0	.0	.0	.0	.0
22 OUTER CONICAL	0.0	0.0	0.0	0.0	0.0	0.0	0.0	0.0	0.0
23 CENTERAL OBSCUR	0.0	0.0	0.0	0.0	0.0	0.0	0.0	0.0	0.0
24 CENT OBSCUR TIP	0.0	0.0	0.0	0.0	0.0	0.0	0.0	0.0	0.0
25 OUTER CONICAL TIP	0.0	0.0	0.0	0.0	0.0	0.0	0.0	0.0	0.0
26 LEFT INNER CONICAL	0.0	0.0	0.0	0.0	0.0	0.0	0.0	0.0	0.0
27 MIDDLE INNER CONICAL	0.0	0.0	0.0	0.0	.2	97.1	84.5	88.3	91.3
28 RIGHT INNER CONICAL	0.0	0.0	0.0	0.0	0.0	0.0	0.0	0.0	0.0
29 INNER CONICAL END	0.0	0.0	0.0	0.0	0.0	0.0	0.0	0.0	0.0
30 IMAGE BAFFLE	0.0	0.0	0.0	0.0	0.0	0.0	0.0	0.0	0.0
31 IMAGE	0.0	0.0	0.0	0.0	0.0	0.0	0.0	0.0	0.0
32 SECONDARY MIRROR	39.2	0.0	0.0	0.0	.0	1.2	6.9	4.8	3.2
33 PRIMARY MIRROR	32.7	34.4	99.0	91.3	94.0	1.5	7.5	6.0	4.8
34 POINT SOURCE	0.0	0.0	0.0	0.0	0.0	0.0	0.0	0.0	0.0
TOTAL POWER	.764E-04	.204E-04	.166E-05	.113E-06	.912E-07	.394E-09	.257E-13	.219E-13	.127E-13
SOURCE ANG	5.0	10.0	17.0	24.0	30.0	60.0	88.0	98.0	108.0

* INFRARED ASTRONOMICAL SATELLITE (IRAS)
* SCATTERED LIGHT VISIBLE DETECTOR, MARTIN BLACK
* FOR AMES RESEARCH CENTER-NASA JULY 23, 1978
* PERKIN-ELMER DESIGN NUMBER 693-10000 REVISION E OF 5/9/78
* UNITS ARE CM AZIMUTH 180 AWG SRL BRD

Table 8. % Table for 0.4-0.9μ Band with Martin Black for Flight System.

At 10°, the secondary is no longer directly illuminated. The primary mirror and inner-secondary baffle are now the major contributors of scattered light. The mirror scatter remains fixed for both the 5% diffuse and Martin Black calculation, so the relative importance shown in the percent table is due to the change in the black-scattering characteristics.

There are three paths of scatter from the secondary to the detectors (Fig. 19):

1. Directly from the left most sections (20%) of the baffle to the detector.
2. To the image of the detector as reflected in secondary (right most sections - 20%)
3. To the image of the detector as reflected by the primary and secondary (right most sections - 20%).

The projected solid angle of the detector, as seen from the source sections, is 100 times less from the last two positions when compared to the directly seen area. However, the left most sections are not directly illuminated at, or beyond, 10 degrees.

With the 5% black the forward and backscatter contributions are approximately equal. This is unrealistic. With the Martin Black model the black-scatter path (Path 3) drops by a factor of about 10 while the forward scatter BRDF goes up by about 100. The forward-scatter path is the dominant propagation path because of the near specular forward scattering characteristics.

For angles between 17° and 24° the primary mirror and aperture stop are both illuminated. The primary receives considerably more power and is thus the major contributor; its relative contribution decreasing as the entrance aperture shades it at larger angles.

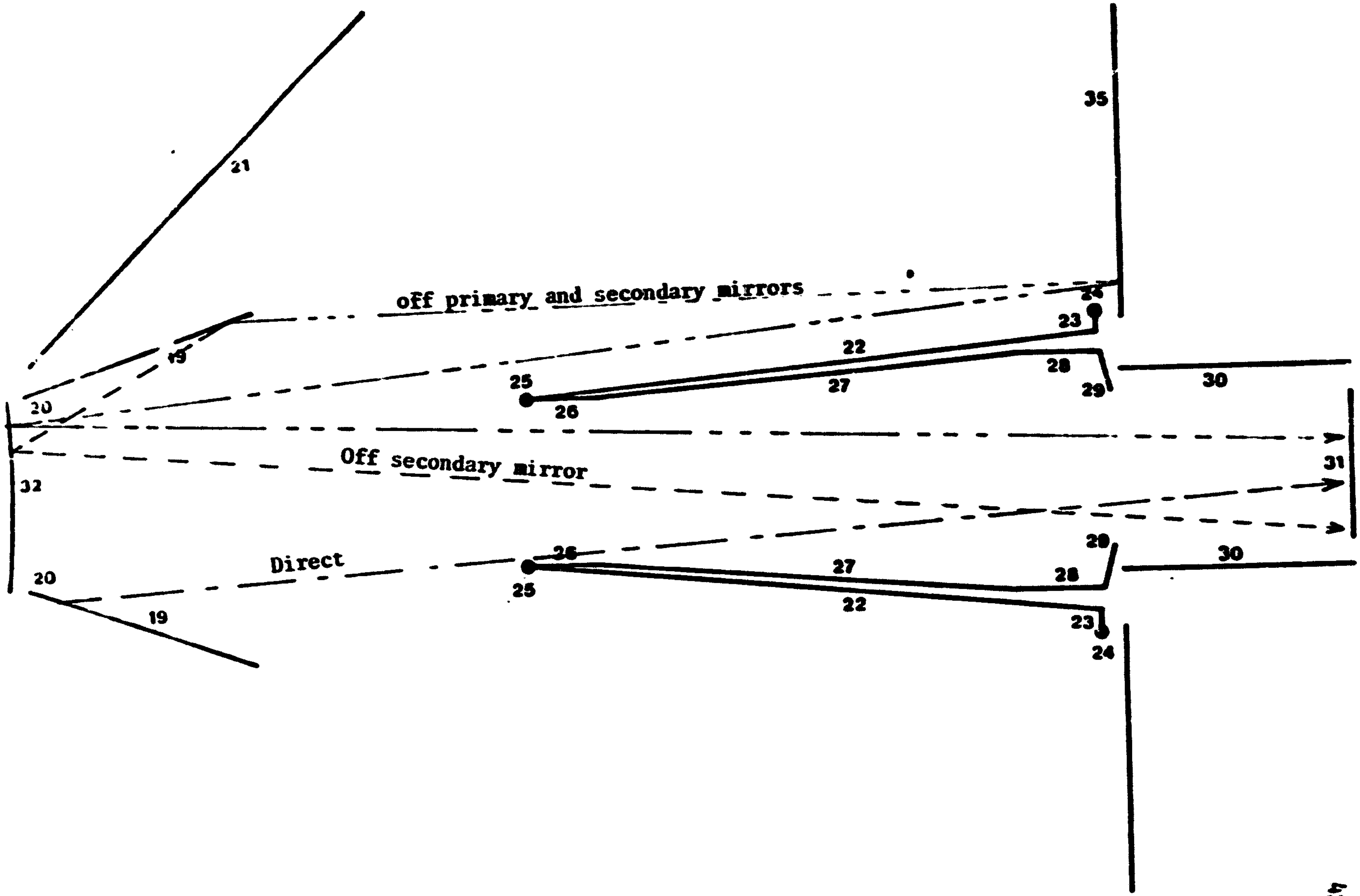

Fig. 19. Paths from the Secondary Baffle to the Image.

For angles larger than 24° no objects are illuminated that are seen from the image. Up to 88° the main tube (objects 5, 6, 8) are illuminated and these in turn scatter to all of the objects seen by the visible detector. At the 30° angle object 8 can transfer power directly to the inner-secondary baffle which causes its contribution to be higher than for larger angles. For all angles larger than 30; the contributions remain fairly constant with only the magnitude dropping with higher angle. At angles greater than 88° the specular heat shield is illuminated (assumed reflectivity $\rho = 0.001$) and this drops the scatter another 4 orders of magnitude.

In summary, the inner-secondary baffle, inner conical baffle, and the mirrors are the dominant sources of scatter. The BRDF at $\beta-\beta_0 = 0.01$ of the mirror is $0.414\ sr^{-1}$ which is high even for average quality mirrors. Somewhat better performance can be expected.

Figure 20a shows the plot of $A(\theta)$ for the 5% diffuse, Martin Black model, and the spec line. The only problem in meeting the specification is at the 60° angle; diffraction is always below the scatter.

5.3 SCATTERED LIGHT ANALYSIS (11μ BAND)

For all the IR bands, the importance of mirror scatter drops significantly. In ideally baffled systems, the $A(\theta)$ values should be determined solely by the optical surfaces (mirror scatter) or by diffraction. However, in this system the limiting factor is either the black surfaces or diffraction. Based upon the available information, the hemispherical-diffuse scatter for Martin Black remains relatively constant until the 100μ IR band. The $A(\theta)$ value will not drop significantly if the principle contributor is a black surface.

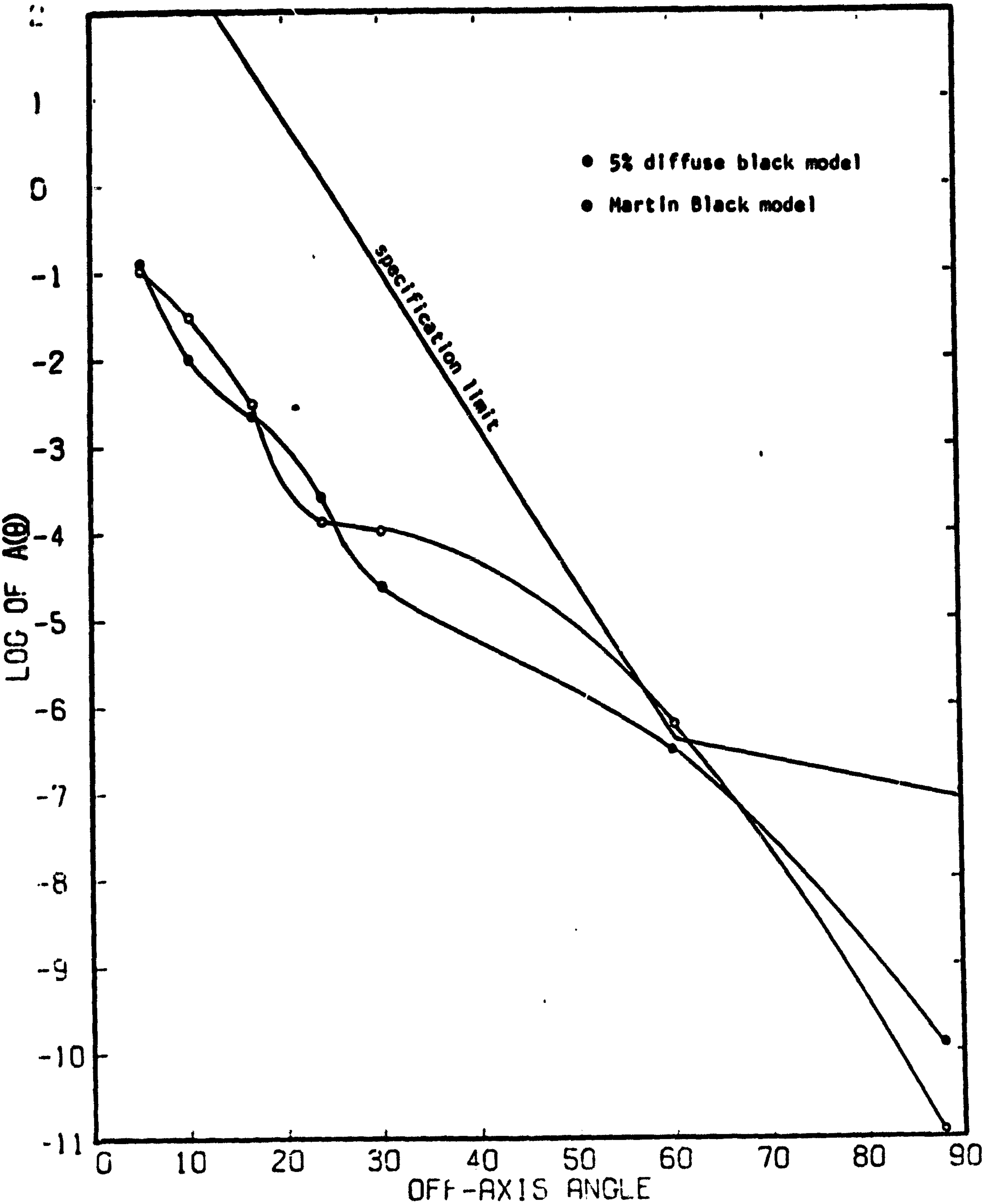

Fig. 20a. A(θ) for Martin Black and 5% Coatings in the 0.4-0.7μ Band.

5.3.1. 5° and 10° Off-axis Source Positions. The principle path of propagation is from the source to the inner-secondary baffle (after reflecting off the primary) to the detector as seen in reflection. This is the same path which was discussed in detail in the discussion of the visible band.

5.3.2. 17°, 24° and 30° Off-axis Source Positions. The dominant path of scatter is from the front side of the aperture to the detector. This is a backscatter direction for near-normal angle of incidence; a near optimum condition for Martin Black. The path is the result of the stop location. Because the stop is not at the secondary, the physical size of the secondary mirror must be oversized to accomodate a field of view, allowing out-of-field elements to be seen from the detector.

At 24° and 30° off-axis angles, power is directly loaded onto the rear sections of the main tube (elements 6 and 8). From there energy scatters directly to the inner-secondary baffle. Half of the radiation on the secondary baffle comes from the last section of vanes on object 6, while the other half comes from object 8. The radiation on the inner-secondary baffle then scatters towards the secondary mirror and reflects to the detectors. This second-order path is significant enough to almost equal the first-order path from the aperture stop to the detectors.

The specular reflections off the sunshield have their greatest impact at these angles and continuing up to about 50° off-axis. The amount of increase is relative to the values shown in Fig. 19.

5.3.3. 60° to 100° Off-axis Source Positions. At 60° off-axis the propagation path is from the source to the front section of the outer-primary baffle, to the inner-secondary baffle (via a reflection off the primary) and then forward scattering to the detector. The specular reflections of the sunshield are no longer significant because they do not enter the main tube.

For off-axis angles greater than 88°, the first collecting element must be the specular sunshield. This radiation is scattered to the vanes on the main baffle, then to the inner-secondary baffle, and finally to the detector.

5.4 SUMMARY OF THE SCATTERED-LIGHT ANALYSES AND RECOMMENDATIONS.

Figures 20b to 20e show the predicted performance of the IRAS system in each of the wavebands. From the previous discussion and the percent table (Table 9) for the 11 micron band, one sees that the mirror scatter is not significant. To reduce the scattered light, one or more of the following steps must be made:

1. Find a better black coating.
2. Change the projected solid angle between the inner-secondary baffle and detectors and also between the aperture stop and the detectors.
3. Reduce the power that reaches the two critical objects: the aperture stop and the secondary baffle.

The first solution is probably not possible in the near future. The second solution can be realized by shifting the stop to the secondary, sacrificing some light-gathering power. An analysis of the APART output indicates that the $A(\theta)$ values should drop by a factor of 90 for all but the 5° off-axis position. At this angle the effect of stop shift is too

Table 9. % Power Contribution to Image for Flight System, Martin Black 11.0μ BRDF Data.

Percent of Power Contributed by Each Object as a Function of Off Axis Source Position

OBJECTS/	OFF AXIS POSITION 1	2	3	4	5	6	7	8	9
1 SHIELD TIP	0.0	0.0	0.0	0.0	0.0	0.0	0.0	0.0	0.[illegible]
2 OUTER SHIELD	0.0	0.0	0.0	0.0	0.0	0.0	0.0	0.0	0.[illegible]
3 RADIATOR	0.0	0.0	0.0	0.0	0.0	0.0	0.0	0.0	0.[illegible]
4 ENTRANCE APT TIP	0.0	0.0	0.0	0.0	0.0	0.0	0.0	0.0	0.[illegible]
5 OUTER MAIN BAFFLE	0.0	0.0	0.0	0.0	0.0	0.0	0.0	0.0	0.[illegible]
6 MIDDLE MAIN BAFFLE	0.0	0.0	0.0	0.0	0.0	0.0	0.0	0.0	0.[illegible]
7 MIDDLE RIGHT END	0.0	0.0	0.0	0.0	0.0	0.0	0.0	0.0	0.[illegible]
8 INNER MAIN BAFFLE	0.0	0.0	0.0	0.0	0.0	0.0	0.0	0.0	0.[illegible]
9 INNER RIGHT END	0.0	0.0	0.0	0.0	0.0	0.0	0.0	0.0	0.[illegible]
10 RIGHT OF 9	0.0	0.0	0.0	0.0	0.0	0.0	0.0	0.0	0.[illegible]
11 LEFT APT CONE	0.0	0.0	0.0	0.0	0.0	0.0	0.0	0.0	0.[illegible]
12 LEFT APERTURE	0.0	0.0	46.6	49.3	0.0	0.0	0.0	0.0	0.[illegible]
13 APERTURE STOP	0.0	0.0	0.0	0.0	0.0	0.0	0.0	0.0	0.[illegible]
14 RIGHT APERTURE	0.0	0.0	30.5	0.0	0.0	0.0	0.0	0.0	0.[illegible]
15 RIGHT APT CONE	0.0	0.0	0.0	0.0	0.0	0.0	0.0	0.0	0.[illegible]
16 SEC HOUSING	0.0	0.0	0.0	0.0	0.0	0.0	0.0	0.0	0.[illegible]
17 OUTER SEC. BAFF	0.0	0.0	0.0	0.0	0.0	0.0	0.0	0.0	0.[illegible]
18 SEC. BAFF TIP	0.0	0.0	0.0	0.0	0.0	0.0	0.0	0.0	0.[illegible]
19 INNER SEC BAFFLE	98.7	99.9	0.0	47.7	88.8	90.4	90.7	90.7	90.[illegible]
20 INNER SEC TIP	0.0	0.0	0.0	0.0	0.0	0.0	0.0	0.0	0.[illegible]
21 STRUT BACK	0.0	0.0	0.0	0.0	0.0	0.0	0.0	.9	1.[illegible]
22 OUTER CONICAL	0.0	0.0	0.0	0.0	0.0	0.0	0.0	0.0	0.[illegible]
23 CENTERAL OBSCUR	0.0	0.0	0.0	0.0	0.0	0.0	0.0	0.0	0.[illegible]
24 CENT OBSCUR TIP	0.0	0.0	0.0	0.0	0.0	0.0	0.0	0.0	0.[illegible]
25 OUTER CONICAL TIP	0.0	0.0	0.0	0.0	0.0	0.0	0.0	0.0	0.[illegible]
26 LEFT INNER CONICAL	0.0	0.0	0.0	0.0	0.0	0.0	0.0	0.0	0.[illegible]
27 MIDDLE INNER CONICAL	0.0	0.0	0.0	0.0	0.0	0.0	.1	0.0	0.[illegible]
28 RIGHT INNER CONICAL	0.0	0.0	0.0	0.0	0.0	0.0	0.0	0.0	0.[illegible]
29 INNER CONICAL END	0.0	0.0	0.0	0.0	0.0	0.0	0.0	0.0	0.[illegible]
30 IMAGE BAFFLE	0.0	0.0	0.0	0.0	0.0	0.0	0.0	0.0	0.[illegible]
31 IMAGE	0.0	0.0	0.0	0.0	0.0	0.0	0.0	0.0	0.[illegible]
32 SECONDARY MIRROR	1.0	0.0	0.0	0.0	.0	3.9	4.1	3.5	3.[illegible]
33 PRIMARY MIRROR	.4	.1	22.9	3.0	11.2	5.7	5.1	4.9	4.[illegible]
34 POINT SOURCE	0.0	0.0	0.0	0.0	0.0	0.0	0.0	0.0	0.[illegible]
TOTAL POWER	.200E-04	.134E-04	.211E-07	.499E-08	.877E-08	.571E-12	.106E-15	.266E-15	.186E-[illegible]
SOURCE ANG	5.0	10.0	17.0	24.0	30.0	60.0	88.0	98.0	108.0

ORIGINAL PAGE IS OF POOR QUALITY

* INFRARED ASTRONOMICAL SATELLITE (IRAS)
* SCATTERED LIGHT
* FOR AMES RESEARCH CENTER NASA JUN 21, 1978
* PERKIN-ELMER DESIGN NUMBER 693-10000 REVISION E OF 5/9/78
* UNITS ARE CM AZIMUTH 160 AWG SRL BRD

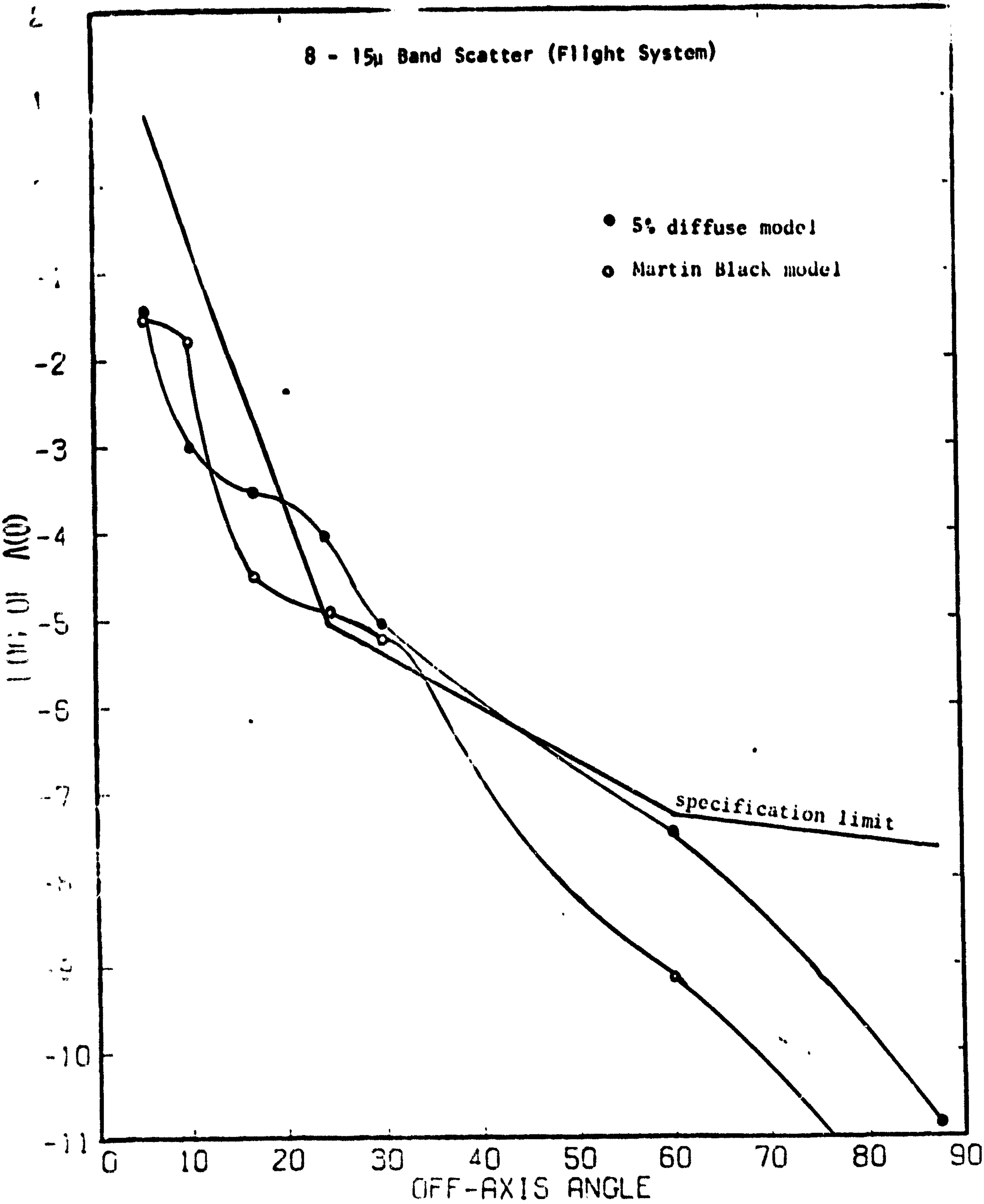

Fig. 20b. A(θ) for OSS in the 11μ Band.

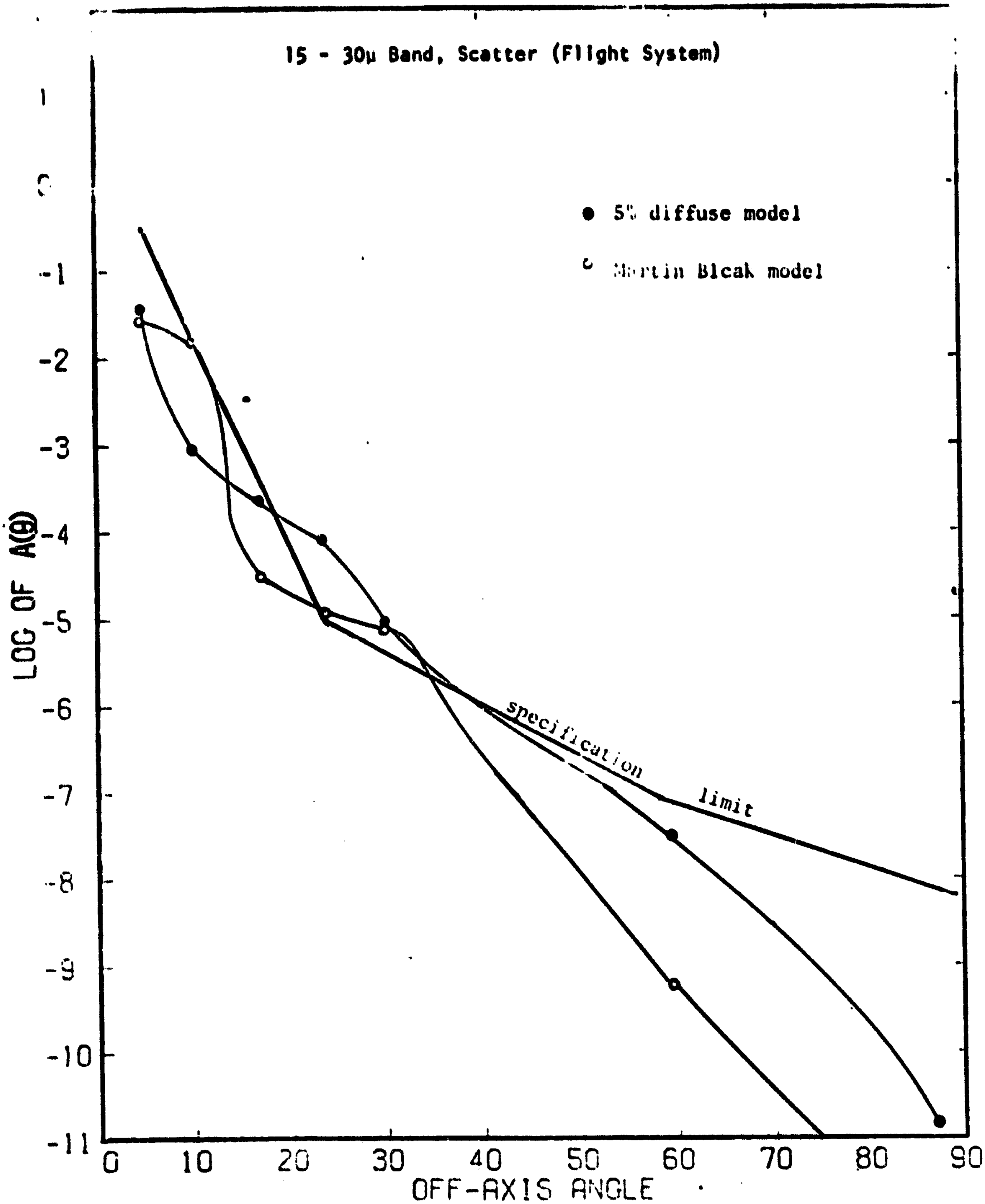

Fig. 20c. A(θ) for OSS in the 22μ Band.

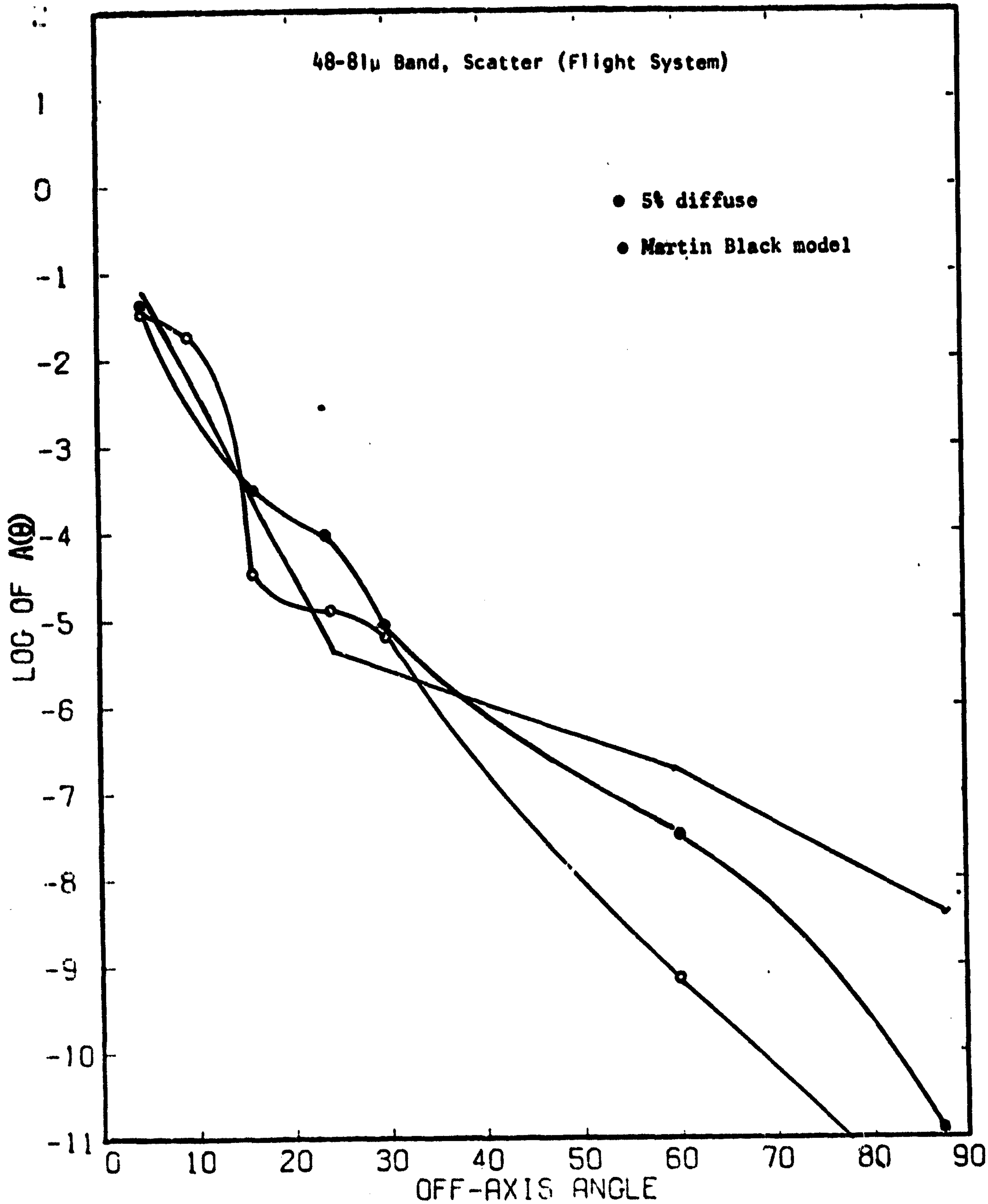

Fig. 20d. A(θ) for the OSS in the 65μ Band.

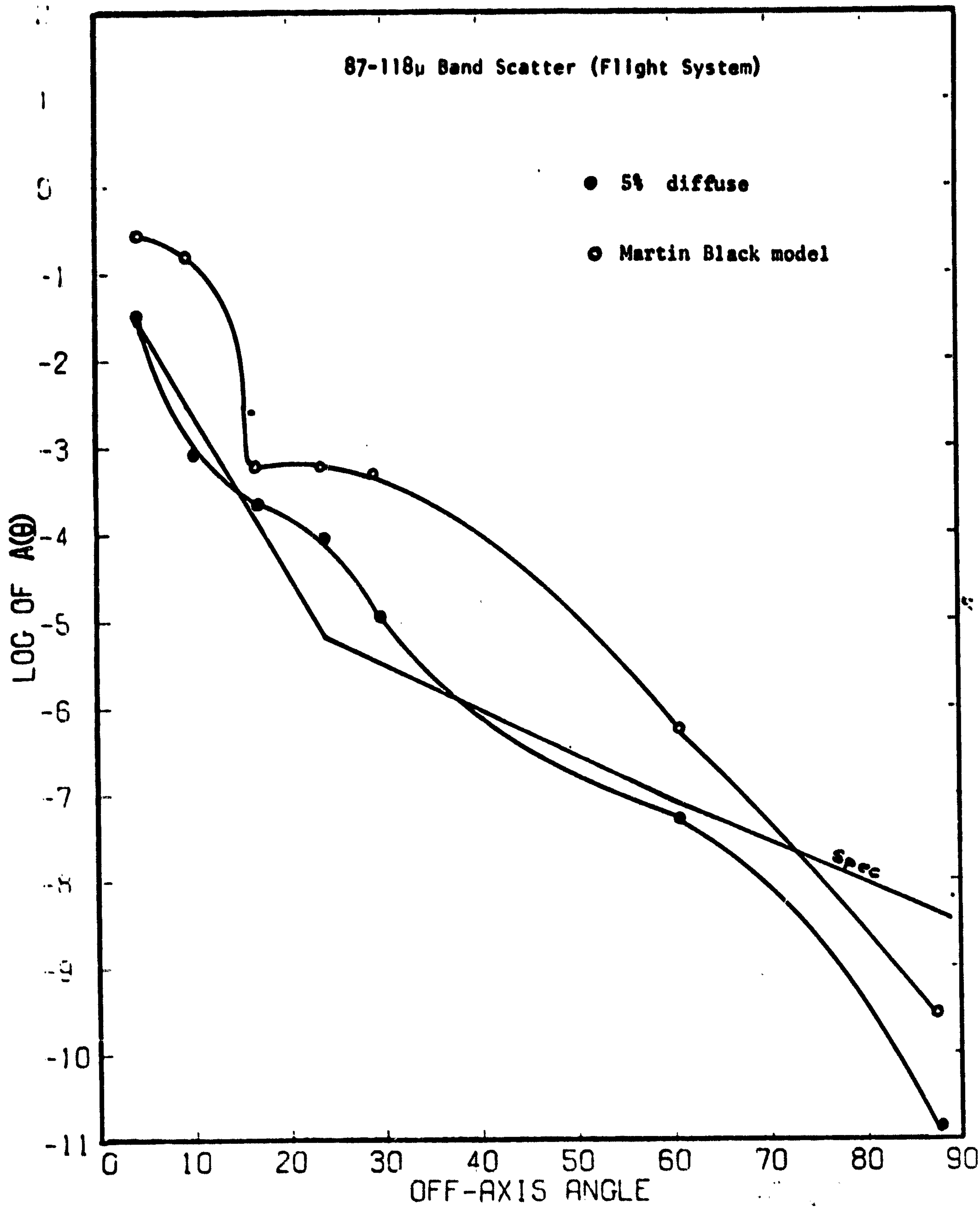

Fig. 20e. A(θ) for the OSS in the 100μ Band.

difficult to predict because low mirror scatter will be replaced by higher diffuse scatter. But, without the additional scatter, the forward scattering path would be eliminated, dropping the A(θ) value by a factor of 10.

The above changes require no change in the secondary baffle design. By making the baffle more cylindrical and adding cylindrical vanes at the base of the secondary baffle, even lower A(θ) values can be achieved. It is strongly recommended that these changes be seriously considered.

The above changes would block the most serious near specular path (off the inner-secondary baffle's black surface), which would be very high if the surfaces are becoming more specular with wavelength.

A specular black coating on the existing aperture stop would have a lower diffuse scatter than Martin Black. However, this would be effective (lower A(θ)) only for a small range of angles about 17°. The specular reflection would also have to be considered and controlled.

The third solution is a redesign such that the aperture stop and secondary baffle would receive less power requiring a redesign of the sunshield, main-baffle tube, and the use of angled vanes. How effective this could be would depend highly upon the size and shapes that would be allowed.

6.0 DIFFRACTION

Since there is no previous publication on our diffraction algorithm, a detailed explanation of its methods and limitations will be presented here.

6.1 INTRODUCTION

In the analysis of stray radiation in an optical system due to an out-of-field source, it is usually necessary to calculate the near-field, wide-angle diffraction from apertures that are orders of magnitude larger than the mean wavelength of the radiation. Since the well-known Fresnel or Fraunhofer approximations do not apply, this would require doing a two-dimensional complex numerical integration over the area of the aperture with a sampling interval on the order of a wavelength. Even with today's computer systems, the storage and calculation requirements would be excessive.

However, we will show how this cumbersome numerical problem can be reduced by suitable approximations to the summation of only a few numbers. The procedure involves a rigorous transformation of the two-dimensional integral over the aperture to a one-dimensional integral along the edge of the aperture. This one-dimensional integral can then be accurately approximated by the sum of the contributions from a few points on the aperture edge. The final simplification involves neglecting the phases of the individual contributions so that complex numbers do not have to be used.

6.2 THEORY

6.2.1 Scalar Diffraction Theory. The various components of electric and magnetic field vectors are coupled together by Maxwell's equations. A self-consistent solution of these equations for complex arbitrary geometries and materials would be difficult. Few such solutions exist even for simple idealized systems. However, the problem can be simplified by assuming that the transverse components are independent of each other so that we will only have to deal with a single scalar quantity, u, that represents one of the transverse components. This assumption turns out to yield accurate results as long as the size of the apertures and observation distances are many wavelengths.

Since this complex scalar field amplitude u(x,y,z,t) obeys the wave equation, for harmonic time signals, u becomes independent of time and must be a solution of the Helmholtz equation.

$$\nabla^2 u + K^2 u = 0 \qquad (K = \frac{2\pi}{\lambda}) \tag{1}$$

The solution in the case of diffraction can be represented as a two-dimensional integral over the diffracting aperture.[11]

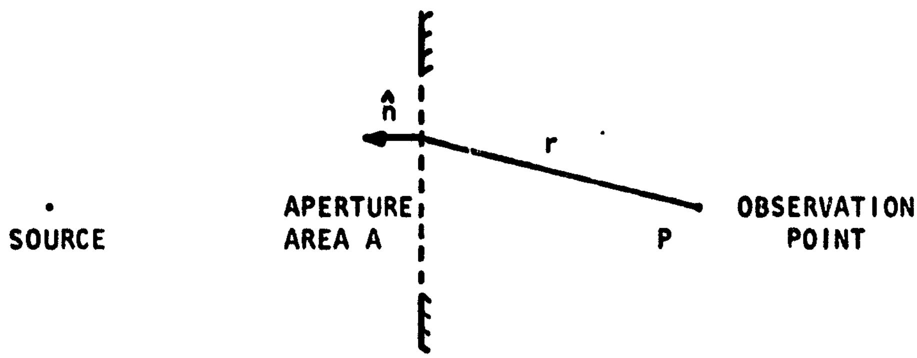

Fig. 21. Typical Geometry for Diffraction Integral

$$u(P) = \frac{1}{4\pi} \iint_A (G \frac{\partial u}{\partial n} - u \frac{\partial G}{\partial n}) \, d\sigma \tag{2}$$

where G is a Green's function which will be specified later.

It is necessary to know the value of the field and its normal derivative everywhere on the aperture. In general, this would be a function of the material properties of the diffracting aperture. If we assume that the aperture is perfectly absorbing or "black", then Kirchhoff's approximate boundary conditions may be used in the plane of the aperture:

$$\begin{cases} u = \dfrac{\partial u}{\partial n} = 0 & \text{outside aperture opening} \quad (3) \\[2ex] u \;\&\; \dfrac{\partial u}{\partial n} & \text{are the same as the incident field inside opening} \quad (4) \end{cases}$$

Although these conditions seem quite reasonable, they lead to a mathematical inconsistency in that they are not reproduced by our formula for the diffracted field when the observation point is in the aperture plane. Nevertheless, experimental measurements[12] have found that they produce surprisingly accurate predictions, again as long as we are not too near the aperture.

It is now left to specify the function G. G must also be a solution of the Helmoltz equation. The simplest choice turns out to be a spherical wave that emanates from the point of interest in the aperture.

$$G = \frac{e^{ikr}}{r} \tag{5}$$

This choice of Green's function corresponds to the Fresnel-Kirchhoff formulation of diffraction. Other Green's functions are possible which can lead in some cases to substantially different results. We will return to this point in a later section.

6.2.2 Boundary Wave Diffraction. The edge of a diffracting aperture appears bright when viewed from within the shadow. This observation was given theoretical footing by Sommerfeld's rigorous solution of the diffraction from the semi-infinite plane.[13] His result could be manipulated to yield a wave component that emanates from the edge.

Then Rubinowicz was able to rigorously decompose the Kirchhoff scalar diffraction formula into a geometric wave and a diffracted boundary wave for arbitrary apertures by properly modifying the region of integration.[14]

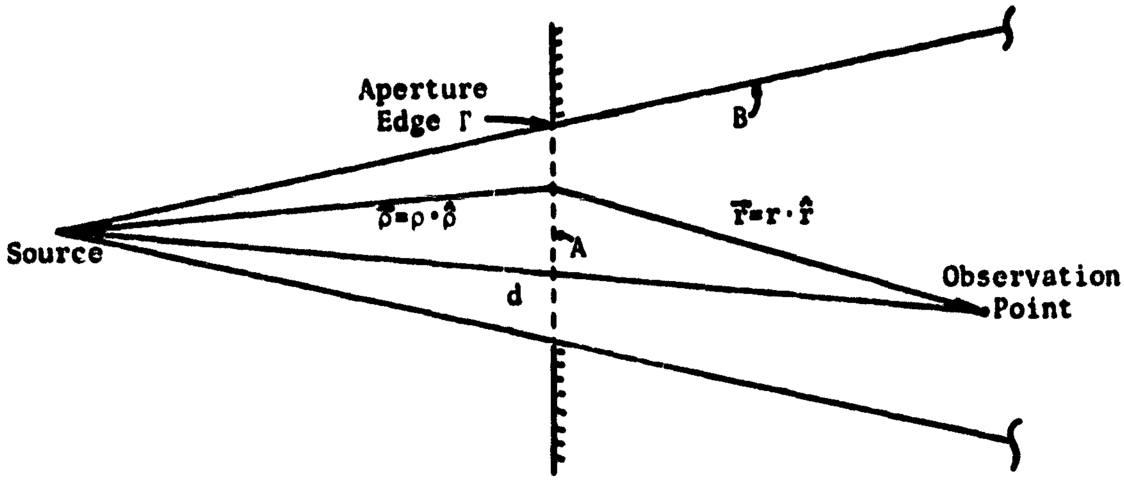

Fig. 22. Regions of Integration in Boundary-wave Formulation.

Then

$$u = u_G + u_D \tag{6}$$

where the geometrical field is:

$$u_G = \begin{cases} \dfrac{e^{ikd}}{d} & \text{in light region} \\ 0 & \text{in shadow region} \end{cases} \tag{7}$$

and the diffracted field is given by:[15]

$$u_D = \frac{1}{4\pi} \iint_B \left(\frac{e^{ikr}}{r} \cdot \frac{\partial}{\partial n} \frac{e^{ik\rho}}{\rho} - \frac{e^{ik\rho}}{\rho} \cdot \frac{\partial}{\partial n} \frac{e^{ikr}}{r} \right) d\sigma$$

$$= -\frac{1}{4\pi} \oint_\Gamma \frac{e^{ik(r+\rho)}}{r\rho} \frac{(\hat{r}\times\hat{\rho})\cdot\boldsymbol{\ell}}{(1+\hat{r}\cdot\hat{\rho})} \, d\ell \qquad (8)$$

On the boundary of the geometric shadow where $\hat{r}\cdot\hat{\rho} = -1$, both the geometrical and diffracted field are discontinuous. These discontinuities compensate one another such that the total field is continuous across the shadow edge.

<u>6.2.3. The Method of Stationary Phase</u>. We have reduced the calculation of diffraction from integrating over an area to integrating along a line. For the large apertures encountered in real optical systems, this one-dimensional integral would still require excessive calculational effort, either analytically or numerically. However, because the apertures are orders of magnitude larger than the wavelength, the stationary phase approximation can be applied.

For convenience, we can write the equation for the diffracted field in the form:

$$u_D = \int_a^b f(\ell) \, e^{ik\mu(\ell)} d\ell \qquad (9)$$

The interval of integration [a,b] does not necessarily enclose the entire edge since the edge could be only partially illuminated by the source or seen from the observation point due to intervening objects.

This integral can be suitably approximated by the method of stationary phase:[16]

$$u_D = \sum_{i=1}^{N} f(\ell_i) e^{ik\mu(\ell_i)} \sqrt{\frac{2\pi}{K|\mu''(\ell_i)|}}\; e^{i\,\pi/4\cdot \mathrm{SIGN}(\mu''(\ell_i))}$$

$$+ \frac{f(b)e^{ik\mu(b)}}{ik\mu'(b)} - \frac{f(a)e^{ik\mu(a)}}{ik\mu'(a)} + \mathcal{O}\left(\frac{1}{K^2}\right) \qquad (10)$$

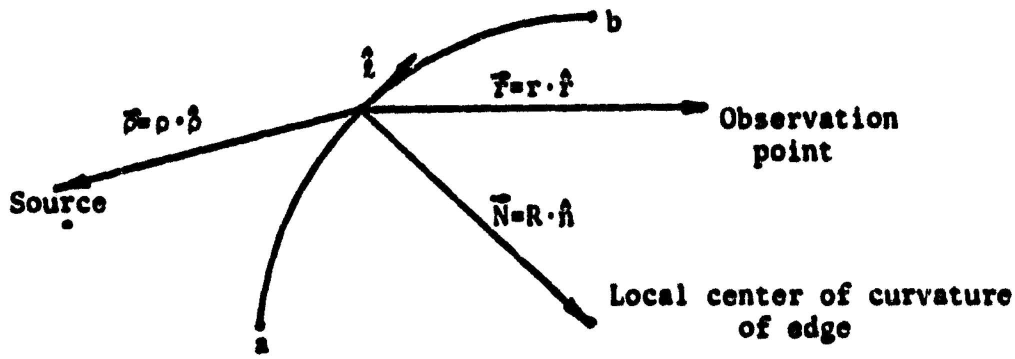

Fig. 23. Vector Definitions for Stationary Phase Approximation to the Boundary Wave Integral.

where

$$\mu(\ell) = r+\rho$$

$$\mu'(\ell) = -(\hat{r}+\hat{\rho})\cdot\hat{\ell} = \frac{d\mu(\ell)}{d\ell}$$

$$\mu''(\ell) = \frac{(\hat{r}\times\hat{\ell})^2}{r} + \frac{(\hat{\rho}\times\hat{\ell})^2}{\rho} - \frac{(\hat{r}+\hat{\rho})\cdot\hat{n}}{R}$$

$$f(\ell) = \frac{-a(\ell)(\hat{r}\times\hat{\rho})\cdot\hat{\ell}}{4\pi r(1+\hat{r}\cdot\hat{\rho})}\ , \quad a(\ell) = \text{incident amplitude } \alpha\ \frac{1}{\rho}$$

The points on the edge of stationary phase (minimum or maximum optical path difference from source to edge to observation point) are determined by:

$$\mu'(\ell_i) = 0 \quad a < \ell_i < b \qquad i = 1,N \qquad (11)$$

In the case of a closed smooth path of integration, there will be in general at least two points of stationary phase and the contribution from the end points of the integration will be zero. In most cases, the contribution from the endpoints will be negligible if a point of stationary phase exists within the interval because it scales as λ^2 as opposed to only λ for the stationary phase contribution.

6.2.4. Addition of the Fields from the Diffraction Points. The diffracted field at the observation point now has the form of a simple summation of complex numbers, i.e.,

$$u_D = \sum_{n=1}^{N} A_n e^{i\phi_n} \qquad A_n , \phi_n \text{ REAL} \quad A_n \geq 0 \tag{12}$$

where N is the number of stationary phase points on the diffracting element of the edge plus two. The irradiance is just the modulus squared of u_D:

$$E_D = |u_D|^2 = u_D u_D^* \tag{13}$$

Upon substitution:

$$E_D = \left[\sum_{n=1}^{N} A_n e^{i\phi_n}\right] \cdot \left[\sum_{n=1}^{N} A_n e^{-i\phi_n}\right]$$

$$= \sum_{n=1}^{N} A_n^2 + 2 \sum_{n=1}^{N} \sum_{m=1}^{N} A_n A_m \cos(\phi_n - \phi_m) \tag{14}$$

Since the a's and ϕ's are smooth functions of the system variables, the first term represents the D.C. component while the second term contains the oscillitory behavior. If we want the envelope of the diffraction pattern in the vicinity of the observation point, let

$$\cos(\phi_n - \phi_m) \rightarrow 1 \tag{15}$$

then:

$$\text{MAX } [E_D] = \sum_{n=1}^{N} A_n{}^2 + 2 \sum_{n=1}^{N} \sum_{m=1}^{N} A_n A_m$$

$$= \sum_{n=1}^{N} A_n{}^2 \tag{16}$$

i.e., the different terms are exactly in phase.

Suppose, that one is more interested in an average value or, in a statistical sense, the most likely value of the irradiance. The phase is related to the system parameters by:

$$\phi = \frac{2\pi}{\lambda} \cdot [\text{OPTICAL PATH LENGTH}] \tag{17}$$

It is therefore a function of the source location, observation point location, location of the edge and wavelength of the radiation. If the incoherent source and/or detector are of a finite size then it is necessary to integrate over them. Likewise, if this incident radiation is polychromatic, then one must integrate over the wavelength band. In general, the phase difference will vary rapidly, so that the integration will be over a function that oscillates many times around a mean value of zero. Therefore, $\int \cos(\phi_n - \phi_m) \approx 0$ and

$$\int E_D \approx \int \sum_{n=1}^{N} A_n{}^2 \tag{18}$$

The average value of the irradiance is:

$$\left\langle E_D \right\rangle \approx \sum_{n=1}^{N} A_n{}^2 \tag{19}$$

One could arrive at the same result using an equivalent statistical argument. If the location of the source, aperture, and observation point and wavelength have a certain uncertainty associated with them, then the phase is a random number. If its distribution function extends over many radians (O.P.D. of several wavelengths), then the expectation value of the cosine of the phase differences will be zero. Therefore, the expected value of the irradiance is just an incoherent superposition of the individual contributions:

$$\langle E_D \rangle \simeq \sum_{n=1}^{N} A_n^{\,2} \tag{20}$$

Finally, suppose all the contributions are approximately equal then:

$$A_n \simeq a \qquad n=1,2\ldots N \tag{21}$$

and

$$\text{MAX } [E_D] \simeq N \langle E_D \rangle \tag{22}$$

However, if one contribution dominates over the others

$$A_1 = A \;\&\; A_2 = A_3 \ldots A_n \simeq 0 \tag{23}$$

then

$$\text{MAX } [E_D] \simeq \langle E_D \rangle \tag{24}$$

Therefore, it depends on the particular problem as to which number is more meaningful. In either case, it is not necessary to keep track of the phases of the individual diffraction contributions, and the calculation of diffracted energy is reduced to the summation of a few real numbers.

6.3 THE PADE COMPUTER PROGRAM

A computer program, based on the theory develo... in the preceding section, has been written to calculate the diffracted energy in a complex optical system. Called PADE (Paraxial Analysis of Diffracted Energy), the program is structured after the APART program so that the two can be used in conjunction to calculate mixed mode, i.e., diffraction and scattering, stray radiation paths.

As in APART, objects are divided into sections.

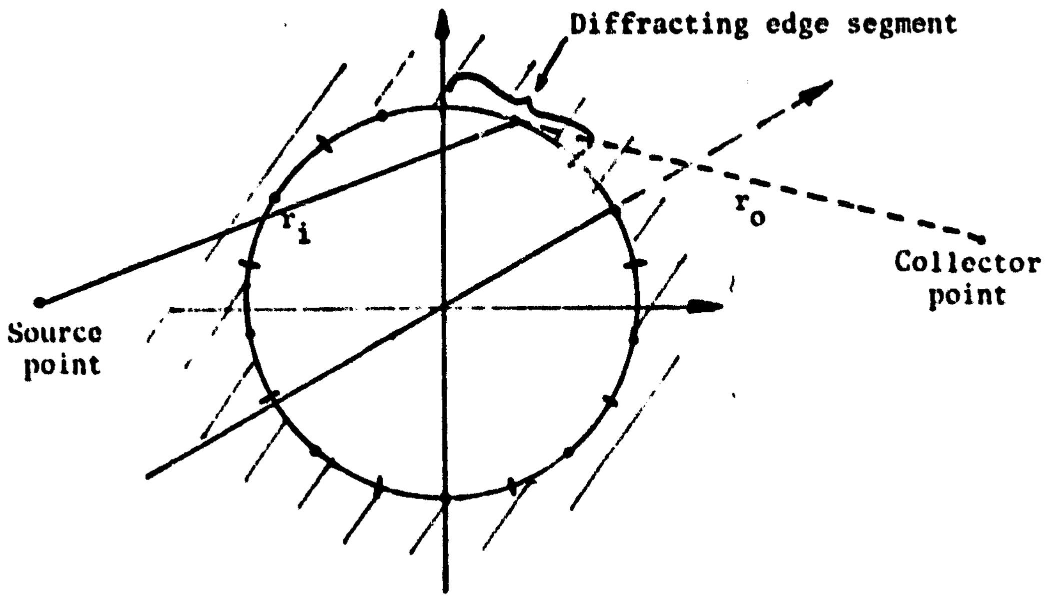

Fig. 24. Sectioned Diffracting Edge.

Imaging and obscurations are handled just as they are in APART.

To calculate the diffracted energy from a particular section on the edge, a modification of the basic APART equation (see Appendix C) is used:

$$\phi_c = E_i \cdot BDDF \cdot GCF' \tag{25}$$

where ϕ_c is the power on the collector area and E_i is the power incident on a unit area surface normal to the incoming beam at the edge point. The GCF' factor is the same as in APART except that the edge is treated as a ficticious unit area surface normal to both the incoming and outcoming beam depending on whether it is a collector or source, respectively. The BRDF of a scattering surface has been replaced by a newly defined function the BDDF (Bi-directional Diffraction Distribution Function) which contains the directional characteristics of the diffraction process at the edge.

A spherical coordinate-system is used in specifying the incoming and outgoing directions from the center of each edge segment.

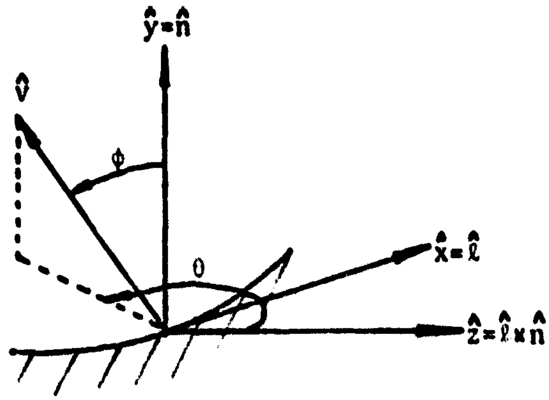

Fig. 25. Local Spherical Coordinate System for Edge Segment.

For an arbitrary unit vector $\hat{v}$:

$$\begin{cases} \hat{v}\cdot\hat{x} = \sin\phi\,\sin\theta & (26) \\ \hat{v}\cdot\hat{y} = \cos\phi & (27) \\ \hat{v}\cdot\hat{z} = \sin\phi\,\cos\theta & (28) \end{cases}$$

We adopt the convention that the subscript "i" refers to the incoming direction and "o" to the outgoing. Also we must define the BDDF according to the power equation

$$\mathrm{BDDF} = \frac{E_c}{E_i} \cdot r_o^{\,2} \tag{29}$$

where E_c is the irradiance at the collector, which is a distance r_o away, and E_i is the irradiance incident onto the edge.

The BDDF will have three separate forms. (Since we assume incoherent addition, each contribution can be treated separately.) The first is the simplest and occurs when the optical path difference is constant across the edge segment. The last two correspond to the two terms of the stationary phase approximation. In all cases there is one factor that is common to all of them:

$$B' = \left[\frac{(\hat{r}_o \times \hat{r}_i)\cdot \ell}{4\pi(1+\hat{r}_o \cdot \hat{r}_i)}\right] \tag{30}$$

The vector operations can be written in terms of the incoming and outgoing angle pairs (ϕ_i, θ_i) and (ϕ_o, θ_o).

$$(\hat{r}_o \times \hat{r}_i)\cdot \ell = \cos\phi_o \sin\phi_i \cos\theta_i - \sin\phi_o \cos\theta_o \cos\phi_i \tag{31}$$

$$\hat{r}_o \cdot \hat{r}_i = \cos\phi_i \cos\phi_o + \sin\phi_i \sin\phi_o \cos(\theta_i - \theta_o) \tag{32}$$

When the O.P.D. across the edge segment of length L is less than a wavelength λ, then

$$\mathrm{BDDF} = B'L \tag{33}$$

which is independent of λ.

Otherwise, the method of stationary phase is employed, and one must know whether a point of stationary phase is located within the segment. This point is located where

$$\mu'(\ell) = \mu'(0) + \mu''(0)\ell + \ldots = 0 \tag{34}$$

ℓ is the arclength distance from the center of the segment. The two derivative terms can be written as:

$$\mu'(0) = -(\hat{r}_o+\hat{r}_i)\cdot\hat{\ell} = -(\sin\phi_i \sin\theta_i + \sin\phi_o \sin\theta_o) \tag{35}$$

$$\mu''(0) = \frac{(\hat{r}_o \times \hat{\ell})^2}{r_o} + \frac{(r_i \times \ell)^2}{r_i} - \frac{(\hat{r}_o+\hat{r}_i)\cdot\hat{n}}{R}$$

$$= \frac{1-(\sin\phi_o \sin\theta_o)^2}{r_o} + \frac{1-(\sin\phi_i \sin\theta_i)^2}{r_i} - \frac{\cos\phi_i+\cos\phi_o}{R} \tag{36}$$

where r_i is the distance to the source, and R is the radius of curvature of the segment. The approximate arclength distance to the stationary phase point is therefore:

$$\ell_s \approx -\frac{\mu'(0)}{\mu''(0)} \tag{37}$$

If $\ell_s > L$, then there is definitely no stationary phase point within the segment. The BDDF now depends on whether this segment is at the endpoint of the integration. In other words, if the adjacent segments on each side of the present one are both illuminated by the source, and seen from the collector, the BDDF is zero for the segment even though radiation falls on it. If only one adjacent path is not possible then:

$$\text{BDDF} = B' \left[\frac{\lambda}{2\pi\mu'(0)}\right]^2 \tag{38}$$

If both adjacent paths are impossible, the BDDF is twice this. In either case, the diffraction is proportional to the square of the wavelength.

The formula for ℓ_s is only approximate and it is important to know precisely whether the stationary phase point is in the interval $|\ell| \le \frac{L}{2}$.

If we knew $\mu'(\ell)$ at the ends of the segment then we would be able to tell by the relative signs of $\mu'(\ell)$ at these points, i.e.,

$$\text{IF} \quad \mu'(-\tfrac{L}{2})\ \mu'(\tfrac{L}{2}) \le 0 \quad \text{then} \quad |\ell_s| \le \tfrac{L}{2}$$

$$\text{IF} \quad \mu'(-\tfrac{L}{2})\ \mu'(\tfrac{L}{2}) > 0 \quad \text{then} \quad |\ell_s| > \tfrac{L}{2}$$

It turns out that $\mu'(\ell)$ can be expressed exactly in terms of the midpoint information for a curved or straight segment. First, define:

$$h(\ ) = \begin{cases} \dfrac{(\frac{R}{r} - \cos\phi)\sin(\frac{\ell}{R}) - \sin\phi\sin\theta\cos(\frac{\ell}{R})}{\sqrt{1 + 2\frac{R}{r}[(\frac{R}{r} - \cos\phi)(1-\cos(\frac{\ell}{R})) - \sin\phi\sin\theta\sin(\frac{\ell}{R})]}} & \text{CURVED EDGE} \\[2ex] \dfrac{\frac{\ell}{r} - \sin\phi\sin\theta}{\sqrt{1 + \frac{\ell}{r}[\frac{\ell}{r} - 2\sin\phi\sin\theta]}} & \text{STRAIGHT EDGE} \end{cases} \tag{39}$$

then

$$\mu'(\ell) = h_i(\ell) + h_o(\ell) \tag{40}$$

If the stationary phase point is definitely in the segment, then by the method of stationary stationary phase:

$$\text{BDDF} = B' \frac{\lambda}{|\mu''(0)|} \tag{41}$$

which varies proportionately with the wavelength. The subdivision of the edge is selected so that there is only one point of stationary phase in any one segment.

6.4 COMPUTER ANALYSIS OF IRAS

6.4.1. Introduction. The analysis of stray radiation due to diffraction in the IRAS system was performed using the PADE computer program, Arizona's version of the GUERAP II program and analytical methods. The combination of the three not only served to provide a cross check but to make up for the limitations of each. The GUERAP II program cannot handle struts or diffracting edges after an optical element. The PADE program was developed to overcome these deficiencies. However, it proved to be too cumbersome in analysis the fine-scale diffraction from the struts and therefore more elegant analytical methods were employed.

6.4.2. PADE Analysis. The figure of merit used in this analysis is the customer's attenuation factor $A(\theta)$. It is defined as the ratio of the detector power for an off-axis source to an on-axis one divided by the solid angle of the detector

$$A(\theta) = \frac{P(\theta)}{\Omega \cdot P(0)} \tag{42}$$

If the irradiance on the image plane is fairly uniform, then $A(\theta)$ is insensitive to the size of the detector since both Ω and $P(\theta)$ are proportional to the area of the detector. For this diffraction analysis, the image plane was divided into 18 equal areas.

The irradiance at the center points of each section due to diffraction is calculated by the PADE program and then multiplied by the area of the section in order to get the total power on the section. (This

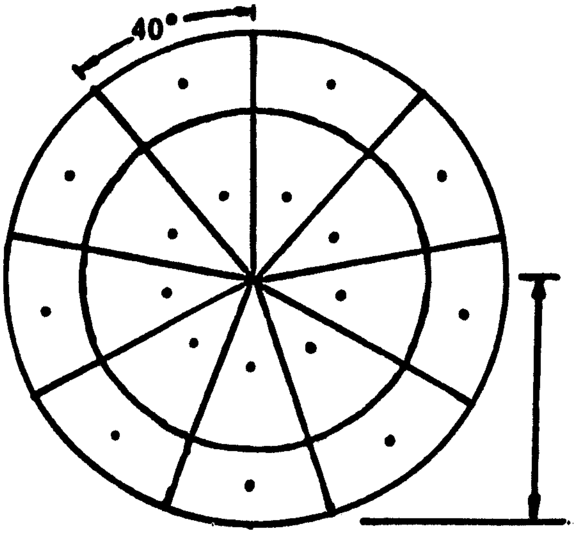

Fig. 26. Sectioned Image Plane.

assumes the irradiance is uniform across the section which is not the case for the sharp peaked diffraction spikes). The power from each section is summed up to get the total power in the image plane. It is this power combined with the solid angle of the entire image plane, $\Omega = \frac{\pi(5.04)^2}{550^2} = 2.6 \cdot 10^{-4}$ which is used to calculate the $A(\theta)$. Essentially we consider the image plane to be a big detector whose output is the average of 18 point detectors. This should be kept in mind when interpreting the results of this analysis.

The diffracting edges used in the analysis of IRAS are shown in Figs. 27, 28, and 29. Figure 29 also defines the azimuthal angle ϕ. Edges with two digit numbers can be seen by the detectors in the image plane. Therefore, as long as they are illuminated by the source the system will be dominated by first-order diffraction. Below $\sim$14° the first order diffraction scales by λ since it is due primarily to contributions from stationary phase points on the circular apertures. Up to about 24° the diffraction will scale as λ^2 since it is the result of the endpoint term of the stationary phase method. The one exception occurs at the peak of a diffraction spike ($\phi = 90°$) from the struts.

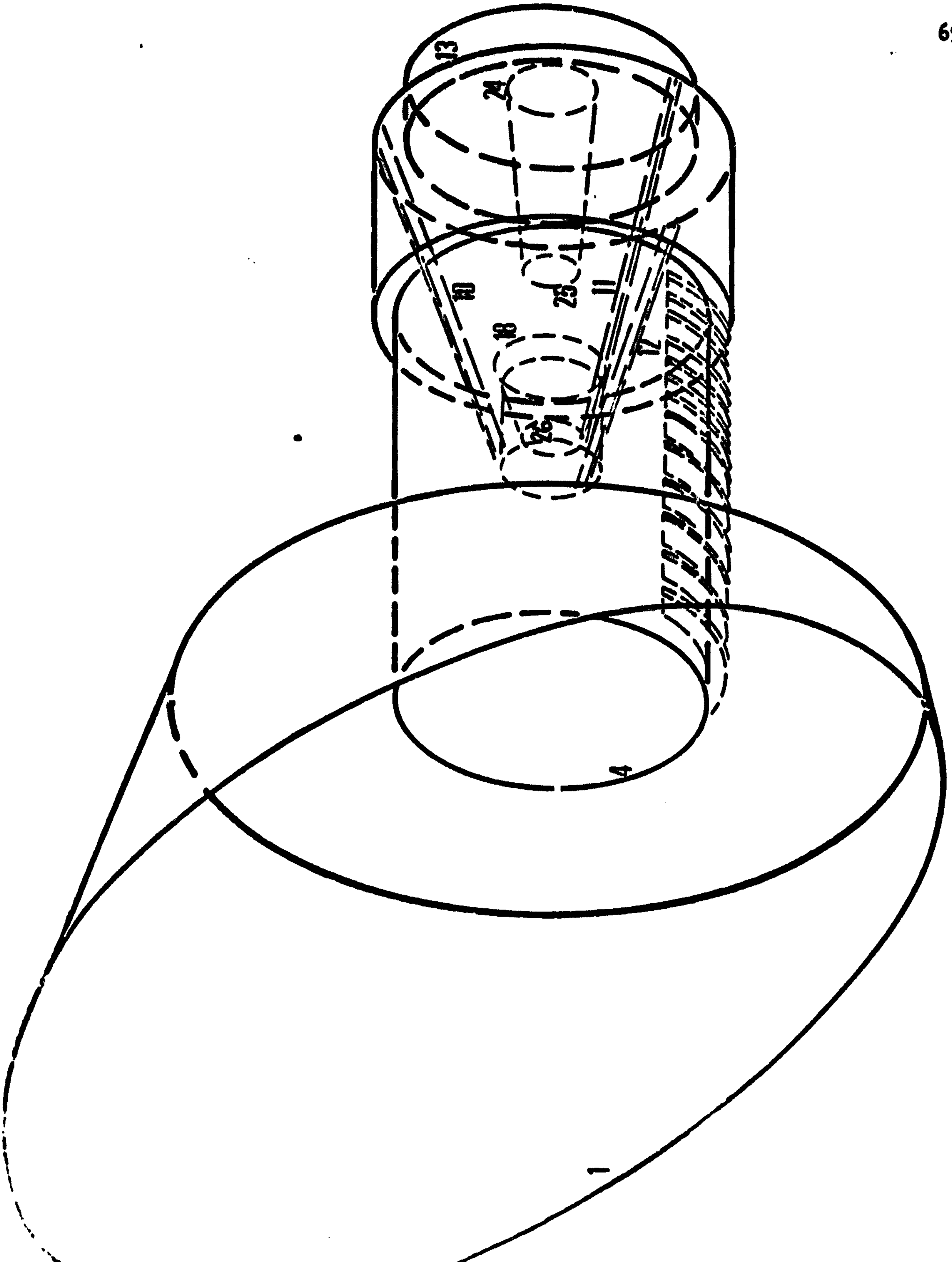

Fig. 27. Diffracting Edges Used in IRAS Analysis (3-D View).

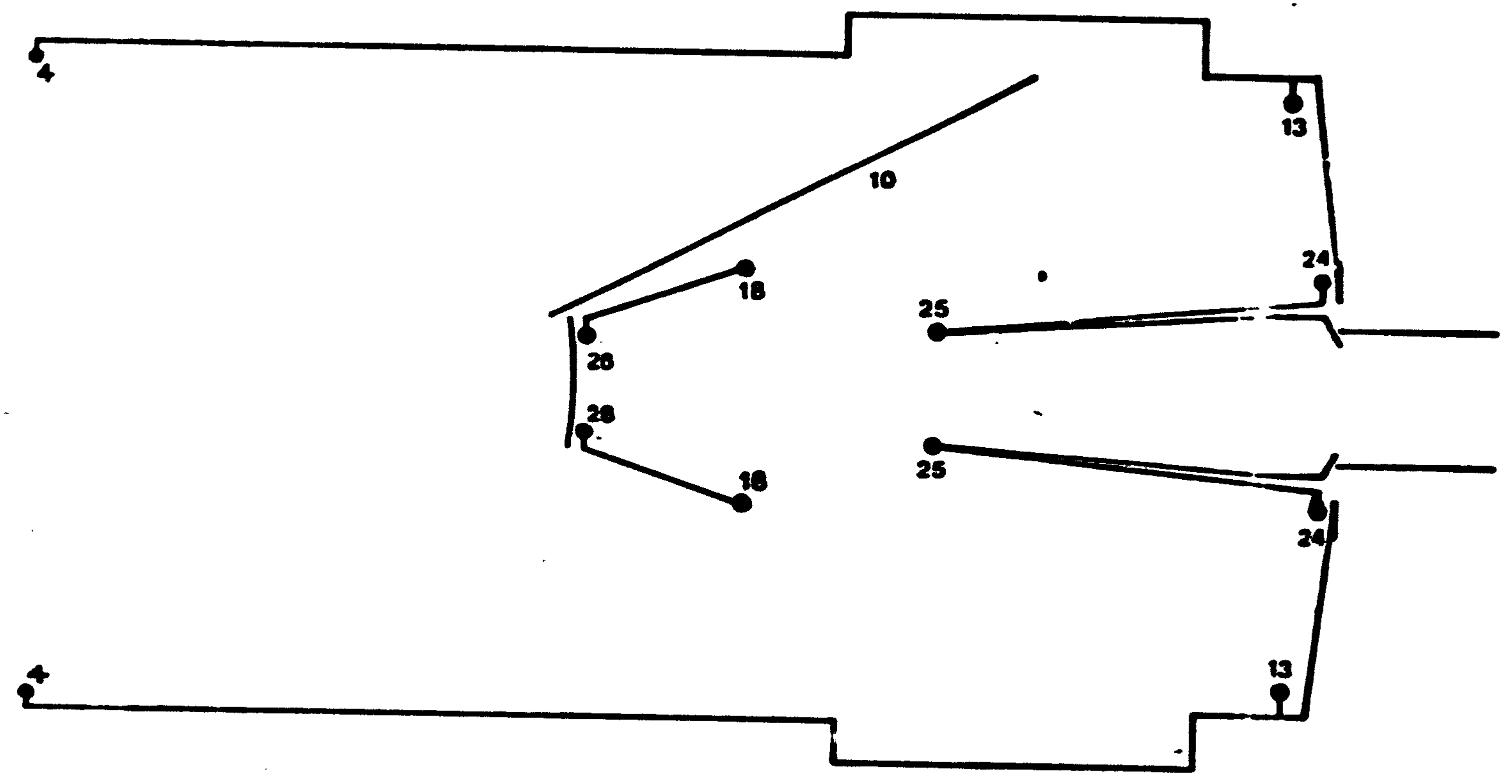

Fig. 28. Diffracting Edges Used in IRAS Analysis (Meridonal Plane).

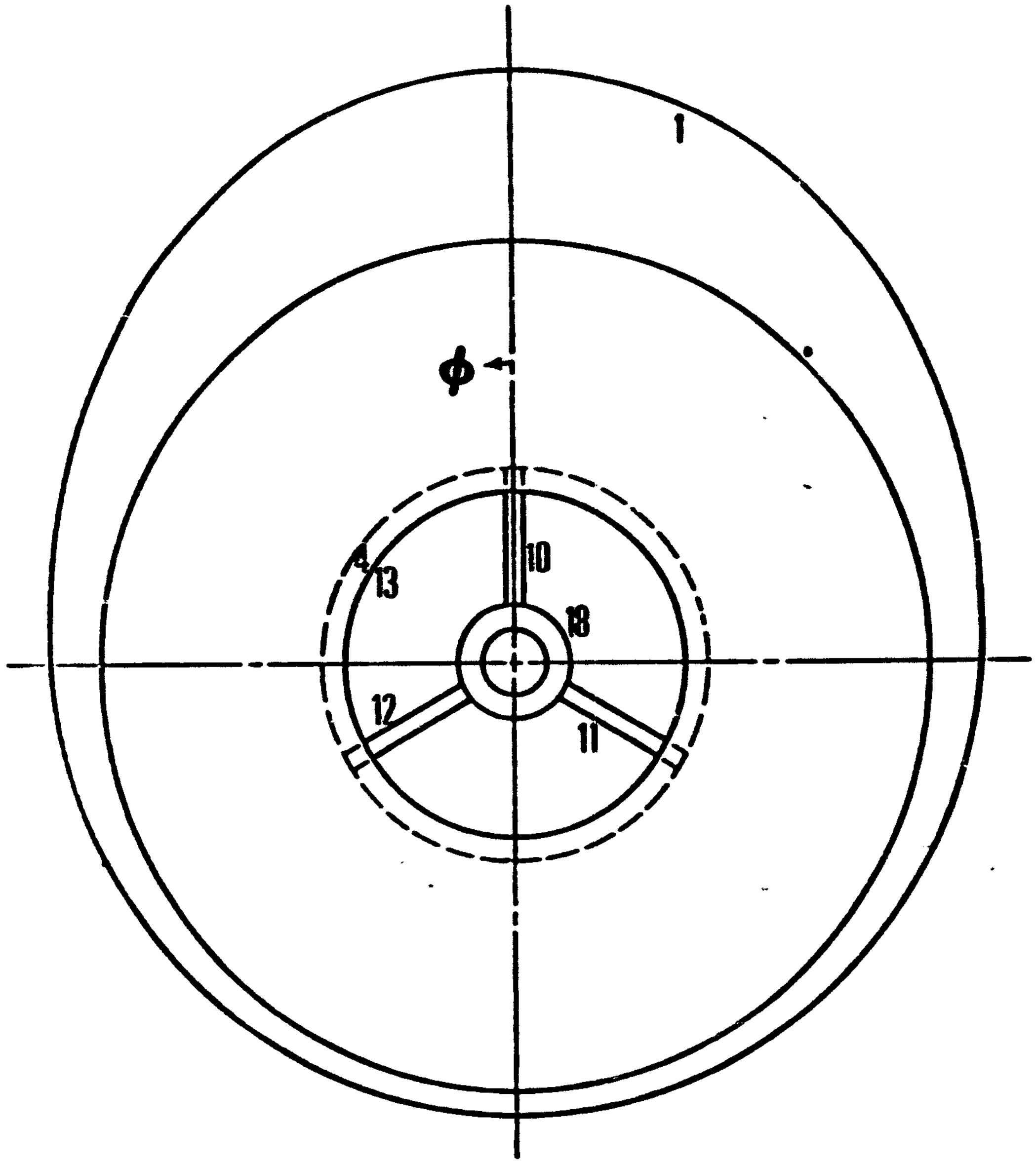

Fig. 29. Definition of Azimuthal Angle.

Due to the point-like nature of our image plane array, the diffraction will be independent of the wavelength in this case.

For source angles greater than 24°, none of the critical edges are illuminated and second-order diffraction dominates. This involves diffracting off the entrance aperture (edge #4) and then proceeding to diffract from the critical two-digit edges. The angle at which the entrance aperture stops receiving energy from the source depends upon the azimuth of the source because of asymmetrical nature of the front of the sunshield. When the source angle is larger than this angle, the dominant diffraction path is from the source to the tilted elliptical shield aperture to the entrance aperture to the critical edges to the detector, i.e., third-order diffraction. No fourth order diffraction paths were considered in this analysis.

The primary analysis was carried out at a wavelength of 102.5μ and for three azimuth angles; 20°, 90° and 180°. The off-axis angles for each azimuth were picked in order to bracket key angles, i.e., where the diffraction goes from one order to the next. The resulting attenuation factors along with the specification are plotted in Fig. 30. All points lie below the spec. except for the 85° off-axis, 180° azimuthal point which is approximately an order of magnitude higher. The three azimuth results are approximately the same up to 45° off-axis after which the asymmetrical shield causes a drop from second to third-order diffraction.

Tables 10,11, and 12 are compilations of the percentage contribution to the energy in the image plane from the critical edges for each azimuth. At 5° off-axis, the distribution for the 20° and 180° azimuths

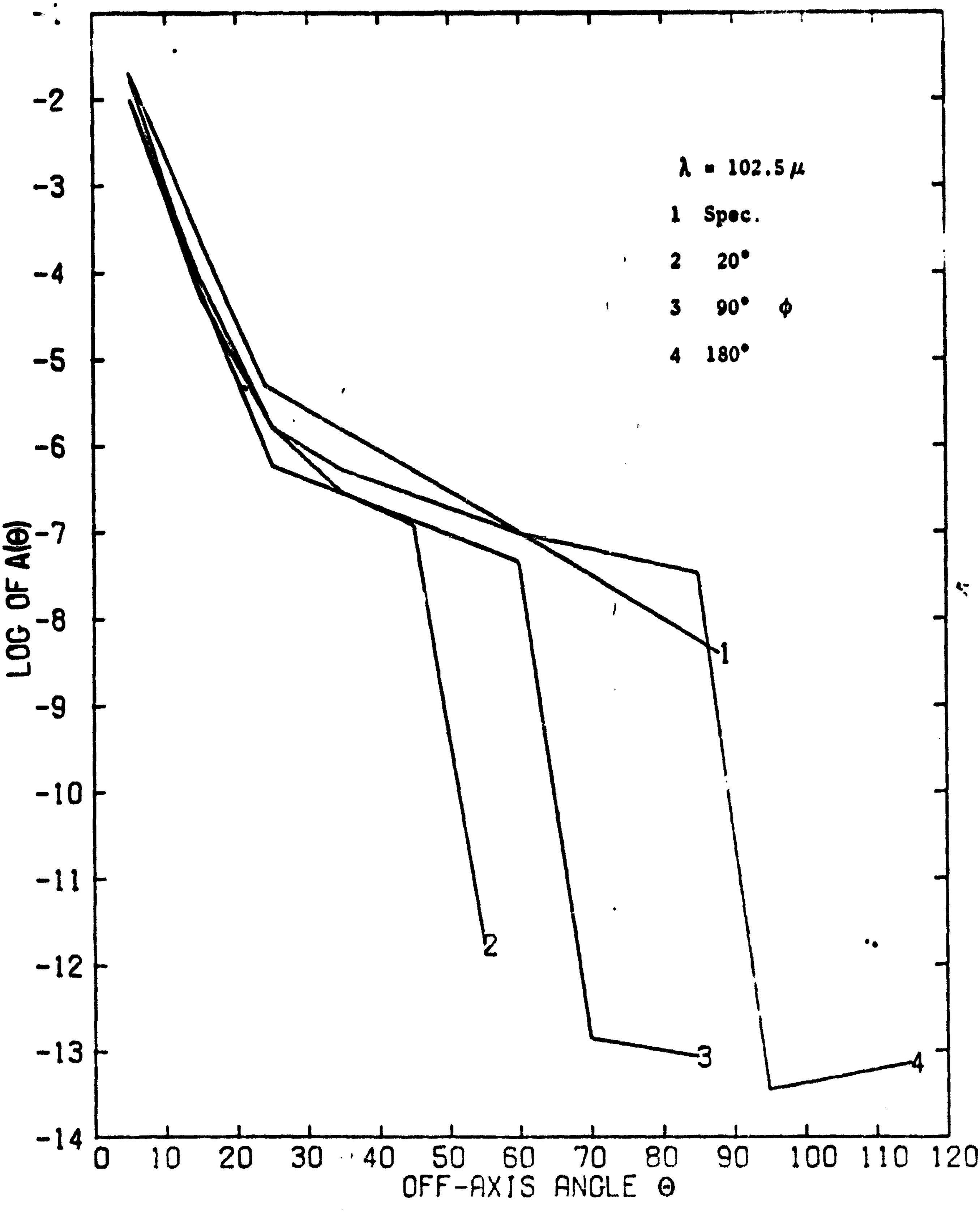

Fig. 30. Attenuation Factor vs. Off-axis Angle for $\lambda = 102.5\mu$.

Table 10. Diffraction Contribution for 20° Azimuth.

Percent of Power Contributed by Each Object as a Function of Off Axis Source Position

OBJECTS/		OFF AXIS POSITION 1	2	3	4	5	6
1	DIFRACT SHIELD EDGE	0.0	0.0	0.0	0.0	0.0	0.0
2	SHIELD APERTURE	0.0	0.0	0.0	0.0	0.0	0.0
3	SHIELD TIP	0.0	0.0	0.0	0.0	0.0	0.0
4	ENTRANCE APT TIP	0.0	0.0	0.0	0.0	0.0	0.0
5	OUTER MAIN BAFFLE	0.0	0.0	0.0	0.0	0.0	0.0
6	MIDDLE MAIN BAFFLE	0.0	0.0	0.0	0.0	0.0	0.0
7		0.0	0.0	0.0	0.0	0.0	0.0
8		0.0	0.0	0.0	0.0	0.0	0.0
9		0.0	0.0	0.0	0.0	0.0	0.0
10	LOWER STRUT EDGE	.0	.0	.0	.0	.0	.7
11	120 RIGHT STRUT EDGE	.0	.0	.0	.0	.0	.0
12	120 LEFT STRUT EDGE	.3	.1	.9	1.2	1.3	.8
13	APERTURE STOP	47.5	.1	98.6	98.6	98.5	97.4
14		0.0	0.0	0.0	0.0	0.0	0.0
15		0.0	0.0	0.0	0.0	0.0	0.0
16	SEC HOUSING	0.0	0.0	0.0	0.0	0.0	0.0
17		0.0	0.0	0.0	0.0	0.0	0.0
18	SEC. BAFF TIP	19.3	99.8	.2	.0	.1	.5
19		0.0	0.0	0.0	0.0	0.0	0.0
20		0.0	0.0	0.0	0.0	0.0	0.0
21		0.0	0.0	0.0	0.0	0.0	0.0
22	OUTER CONICAL	0.0	0.0	0.0	0.0	0.0	0.0
23	PRIMARY MIRROR	0.0	0.0	0.0	0.0	0.0	0.0
24	CENT OBSCUR TIP	27.2	0.0	.2	.1	.1	.5
25	OUTER CONICAL TIP	5.7	0.0	.1	.0	.0	.2
26	SECONDARY EDGE	.0	0.0	.0	.0	.0	.0
27	SECONDARY MIRROR	0.0	0.0	0.0	0.0	0.0	0.0
28		0.0	0.0	0.0	0.0	0.0	0.0
29		0.0	0.0	0.0	0.0	0.0	0.0
30		0.0	0.0	0.0	0.0	0.0	0.0
31	IMAGE	0.0	0.0	0.0	0.0	0.0	0.0
32	POINT SOURCE	0.0	0.0	0.0	0.0	0.0	0.0
	TOTAL POWER	.196E-01	.112E-03	.326E-05	.572E-06	.238E-06	.332E-11
	SOURCE ANG	5.0	15.0	25.0	35.0	45.0	55.0

* INFRARED ASTRONOMICAL SATELLITE (IRAS)
* DIFFRACTION ANALYSIS
* FOR AMES RESEARCH CENTER NASA JUN 21, 1978
* PERKIN-ELMER DESIGN NUMBER 693-10000 BRD
* UNITS ARE CP
* 20 DEG AZIMUTH

Table 11. Diffraction Contributions for 90° Azimuth.

Percent of Power Contributed by Each Object as a Function of Off Axis Source Position

OBJECTS /		OFF AXIS POSITION 1	2	3	4	5	6
1	DIFFRACT SHIELD EDGE	0.0	0.0	0.0	0.0	0.0	0.0
2	SHIELD APERTURE	0.0	0.0	0.0	0.0	0.0	0.0
3	SHIELD TIP	0.0	0.0	0.0	0.0	0.0	0.0
4	ENTRANCE APT TIP	0.0	0.0	0.0	0.0	0.0	0.0
5	OUTER MAIN BAFFLE	0.0	0.0	0.0	0.0	0.0	0.0
6	MIDDLE MA. BAFFLE	0.0	0.0	0.0	0.0	0.0	0.0
7		0.0	0.0	0.0	0.0	0.0	0.0
8		0.0	0.0	0.0	0.0	0.0	0.0
9		0.0	0.0	0.0	0.0	0.0	0.0
10	LOWER STRUT EDGE	38.6	.2	2.1	.0	.7	.6
11	120 RIGHT STRUT EDGE	.0	.0	.0	.0	.1	.1
12	120 LEFT STRUT EDGE	.0	.0	.3	.0	.3	3.3
13	APERTURE STOP	28.0	.1	96.4	99.8	98.1	95.1
14		0.0	0.0	0.0	0.0	0.0	0.0
15		0.0	0.0	0.0	0.0	0.0	0.0
16	SEC HOUSING	0.0	0.0	0.0	0.0	0.0	0.0
17		0.0	0.0	0.0	0.0	0.0	0.0
18	SEC. BAFF TIP	12.1	99.7	.6	.1	.4	.4
19		0.0	0.0	0.0	0.0	0.0	0.0
20		0.0	0.0	0.0	0.0	0.0	0.0
21		0.0	0.0	0.0	0.0	0.0	0.0
22	OUTER CONICAL	0.0	0.0	0.0	0.0	0.0	0.0
23	PRIMARY MIRROR	0.0	0.0	0.0	0.0	0.0	0.0
24	CENT OBSCUR TIP	18.1	.0	.4	.1	.4	.4
25	OUTER CONICAL TIP	3.2	0.0	.2	.1	.1	.2
26	SECONDARY EDGE	.0	0.0	.0	.0	.0	.0
27	SECONDARY MIRROR	0.0	0.0	0.0	0.0	0.0	0.0
28		0.0	0.0	0.0	0.0	0.0	0.0
29		0.0	0.0	0.0	0.0	0.0	0.0
30		0.0	0.0	0.0	0.0	0.0	0.0
31	IMAGE	0.0	0.0	0.0	0.0	0.0	0.0
32	POINT SOURCE	0.0	0.0	0.0	0.0	0.0	0.0
	TOTAL POWER	.328E-01	.133E-03	.117E-05	.901E-07	.271E-12	.167E-12
	SOURCE ANG	5.0	15.0	25.0	60.0	79.0	85.0

* INFRARED ASTRONOMICAL SATELLITE (IRAS)
* DIFFRACTION ANALYSIS
* FOR AMES RESEARCH CENTER NASA JUN 21, 1978
* PERKIN-ELMER DESIGN NUMBER 693-10000
* UNITS ARE CM BRD
* 90 DEG AZIMUTH

Table 12. Diffraction Contributions for 180° Azimuth.

Percent of Power Contributed by Each Object as a Function of Off Axis Source Position

OBJECTS/		OFF AXIS POSITION 1	2	3	4	5	6	7	8
1	DIFRACT SHIELD EDGE	0.0	0.0	0.0	0.0	0.0	0.0	0.0	0.0
2	SHIELD APERTURE	0.0	0.0	0.0	0.0	0.0	0.0	0.0	0.0
3	SHIELD TIP	0.0	0.0	0.0	0.0	0.0	0.0	0.0	0.0
4	ENTRANCE APT TIP	0.0	0.0	0.0	0.0	0.0	0.0	0.0	0.0
5	OUTER MAIN BAFFLE	0.0	0.0	0.0	0.0	0.0	0.0	0.0	0.0
6	MIDDLE MAIN BAFFLE	0.0	0.0	0.0	0.0	0.0	0.0	0.0	0.0
7		0.0	0.0	0.0	0.0	0.0	0.0	0.0	0.0
8		0.0	0.0	0.0	0.0	0.0	0.0	0.0	0.0
9		0.0	0.0	0.0	0.0	0.0	0.0	0.0	0.0
10	LOWER STRUT EDGE	.0	.0	.0	.0	.0	.0	.1	.0
11	120 RIGHT STRUT EDGE	.1	.0	.5	.7	.8	.8	1.0	1.5
12	120 LEFT STRUT EDGE	.1	.0	.5	.7	.8	.8	1.0	1.5
13	APERTURE STOP	47.6	37.8	98.4	98.0	97.9	97.8	96.9	96.3
14		0.0	0.0	0.0	0.0	0.0	0.0	0.0	0.0
15		0.0	0.0	0.0	0.0	0.0	0.0	0.0	0.0
16	SEC HOUSING	0.0	0.0	0.0	0.0	0.0	0.0	0.0	0.0
17		0.0	0.0	0.0	0.0	0.0	0.0	0.0	0.0
18	SEC. BAFF TIP	19.3	62.1	.2	.2	.2	.2	.4	.3
19		0.0	0.0	0.0	0.0	0.0	0.0	0.0	0.0
20		0.0	0.0	0.0	0.0	0.0	0.0	0.0	0.0
21		0.0	0.0	0.0	0.0	0.0	0.0	0.0	0.0
22	OUTER CONICAL	0.0	0.0	0.0	0.0	0.0	0.0	0.0	0.0
23	PRIMARY MIRROR	0.0	0.0	0.0	0.0	0.0	0.0	0.0	0.0
24	CENT OBSCUR TIP	27.2	.0	.2	.2	.2	.2	.4	.3
25	OUTER CONICAL TIP	5.7	.0	.1	.1	.1	.1	.1	.1
26	SECONDARY EDGE	.0	.0	.0	.0	.0	.0	.0	.0
27	SECONDARY MIRROR	0.0	0.0	0.0	0.0	0.0	0.0	0.0	0.0
28		0.0	0.0	0.0	0.0	0.0	0.0	0.0	0.0
29		0.0	0.0	0.0	0.0	0.0	0.0	0.0	0.0
30		0.0	0.0	0.0	0.0	0.0	0.0	0.0	0.0
31	IMAGE	0.0	0.0	0.0	0.0	0.0	0.0	0.0	0.0
32	POINT SOURCE	0.0	0.0	0.0	0.0	0.0	0.0	0.0	0.0
	TOTAL POWER	.196E-01	.180E-03	.327E-05	.104E-05	.195E-06	.669E-07	.693E-13	.142E-12
	SOURCE ANG	5.0	15.0	25.0	35.0	60.0	85.0	95.0	115.0

* INFRARED ASTRONOMICAL SATELLITE (IRAS)
* DIFFRACTION ANALYSIS
* FOR AMES RESEARCH CENTER NASA JUN 21, 1978
* PERKIN-ELMER DESIGN NUMBER 693-10000
* UNITS ARE CM BRD
* 180 DEG AZIMUTH

are nearly identical. The only difference being the expected asymmetric contribution from strut edges 11 and 12 for 20° azimuth. However, these results differ greatly from the 90° azimuth distribution. Now the lower-strut edge #10 is the major contributor instead of the aperture stop. At first glance, this seemed correct since this is the azimuthal angle at which one would expect a long diffraction spike to cross the image plane. However, the diffracted energy is about two orders of magnitude smaller than analytical expressions predicted. This discrepancy is covered in detail in Section 6.5.

At the higher source angles, nearly all the diffracted energy comes from the aperture stop. This is because the source for the critical edges at these angles is the entrance aperture. The diffracted energy from a circular edge is approximately proportional to δ^{-3} where δ is the diffraction angle, i.e., the angle between the incoming and outgoing direction. Since the angle subtended by the image of detector array is small, the outgoing direction is essentially parallel to the optical axis. Therefore, δ is much smaller for the aperture stop than any other critical edge, and the diffraction from it will dominate.

The 102.5μ results can be scaled to produce the other bands. In particular, each data point is scaled by λ^n according to which diffraction order n dominates. The attenuation factors for the mean wavelengths of the other bands are plotted in Figs. 31, 32, 33 and 34. In all cases, the results are near or below the specifications.

6.4.3. GUERAP II Analysis. A diffraction analysis of IRAS was also done using Arizona's version of the GUERAP II diffraction program. The program is based upon the same theory as PADE except that it calculates only the contributions from points of stationary phase and not from the integration end points or edges with constant phase difference across them.[17] For this reason, GUERAP II cannot handle straight edges in general and therefore cannot calculate the diffraction from the struts. Even for points of stationary phase, the actual implementation of the same equation is considerably different in the two codes. GUERAP II considers the diffraction to occur along an astigmatic differential ray while PADE treats the diffracting edge as a psuedo-scattering surface with a specular BRDF. The calculations of the two programs were compared against the analytical solution for first-order diffraction off a circular aperture (see Appendix 3) and all three results differed by less than 1% from each other.

Because of program limitations, GUERAP II also cannot do diffraction off of edges that follow an optical element. (The secondary mirror edge is an example.) None of these edges were the major sources of diffracted energy in the PADE analysis.

Figure 35 is a comparison of the PADE, GUERAP II, and Perkin-Elmer calculations for two different wavelengths. PADE and GUERAP II agree quite well at 5° off-axis where the first-order diffraction off the aperture stop dominates. However, the Perkin-Elmer hand calculation seems to be somewhat low. For the larger source angles, second-order diffraction dominates and the computer calculations differ by nearly an order of magnitude. This is probably a combination of two things.

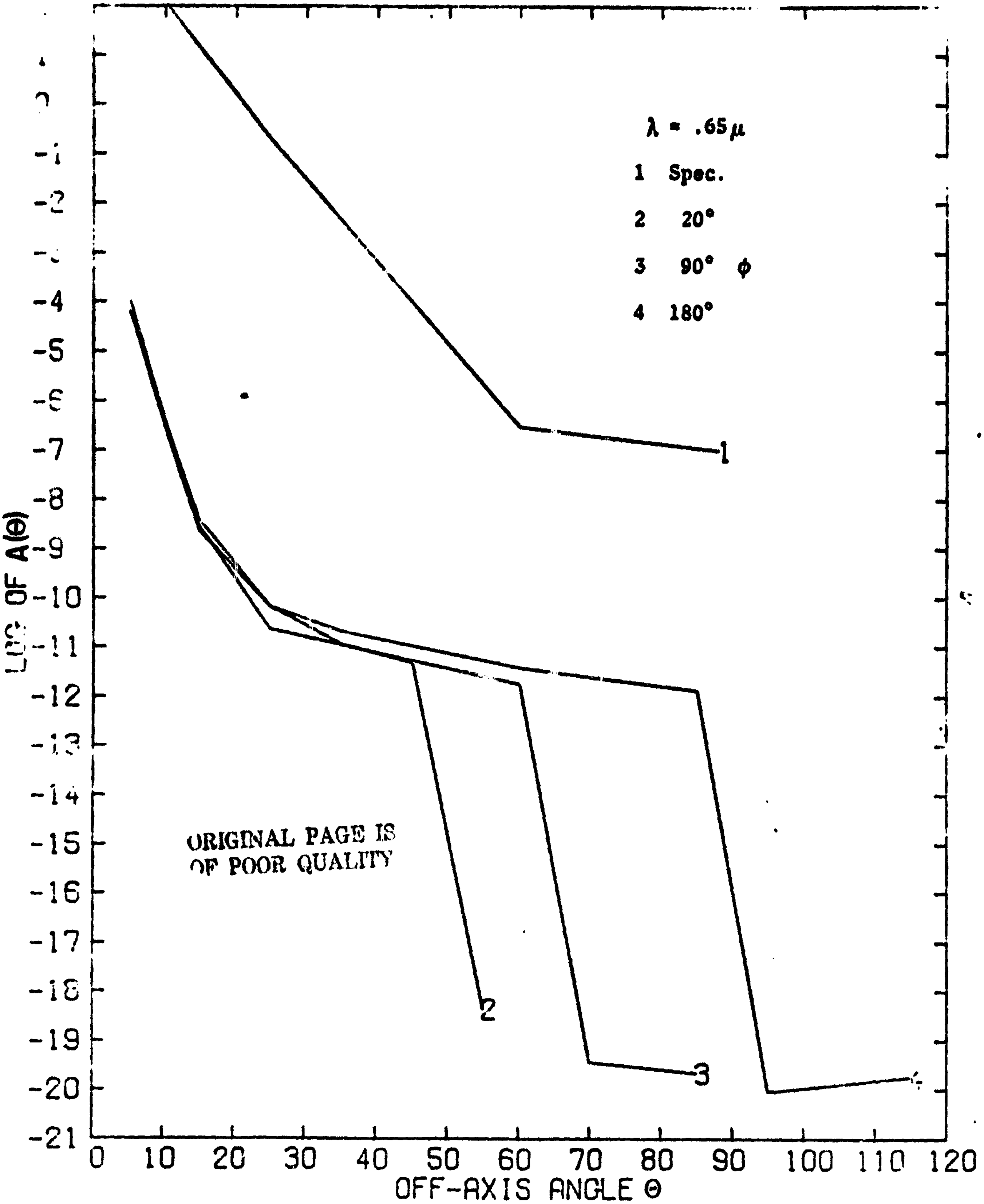

Fig. 31. Attenuation Factor vs. Off-axis Angle for λ = 64.5μ.

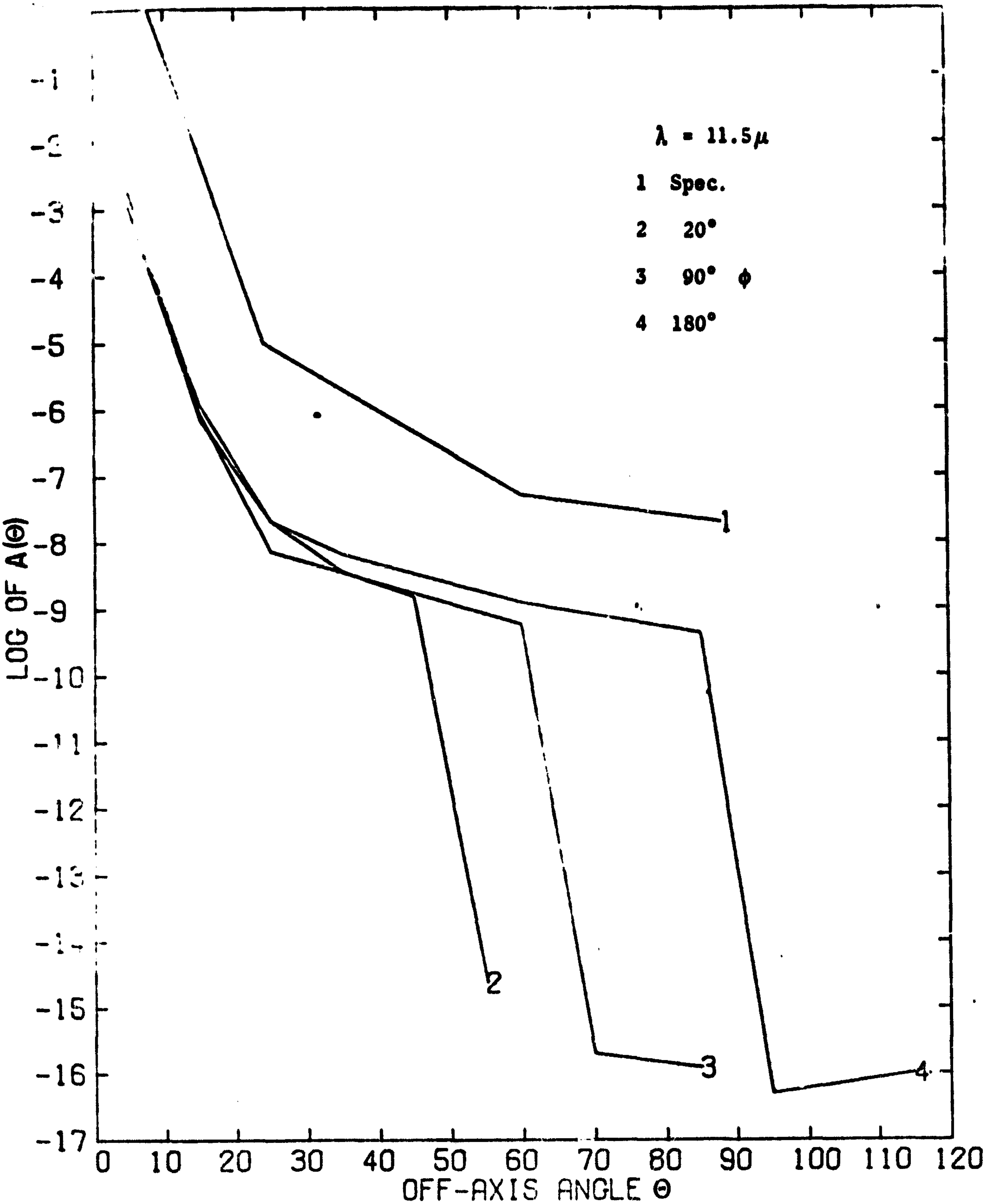

Fig. 32. Attenuation Factor vs. Off-axis Angle for λ = 22.5μ.

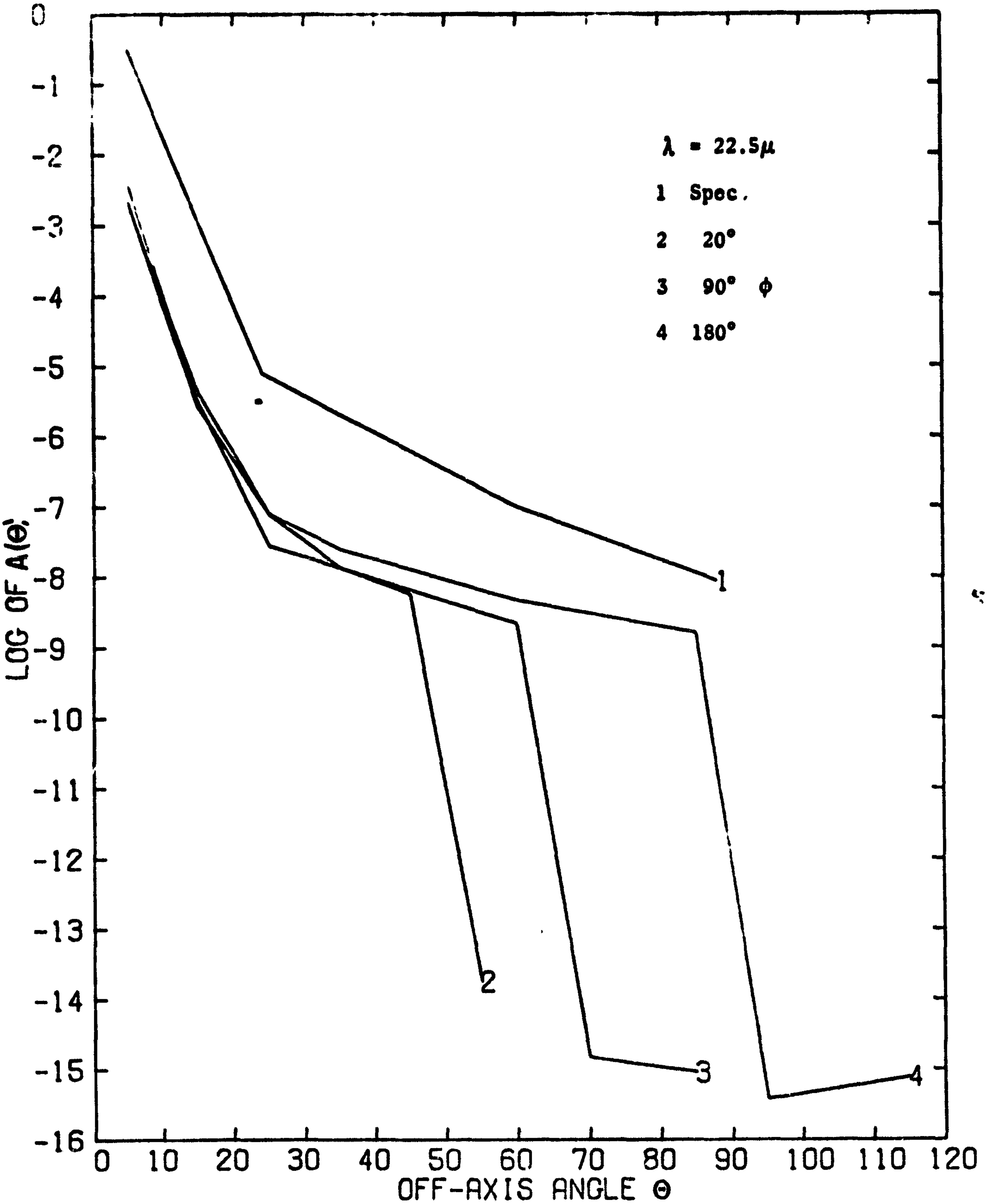

Fig. 33. Attenuation Factor vs. Off-axis Angle for λ = 11.5μ.

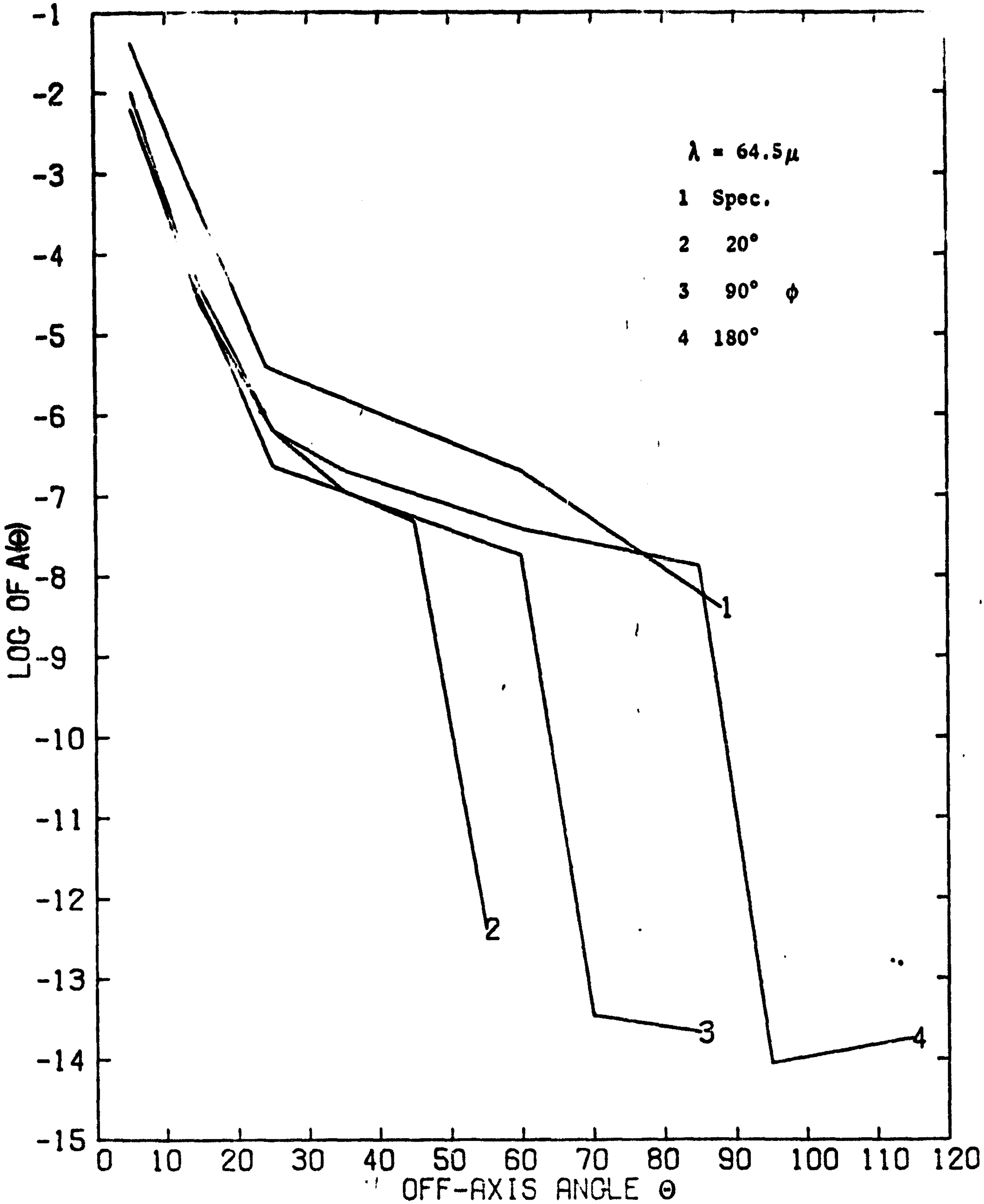

Fig. 34. Attenuation Factor vs. Off-axis Angle for λ = 6.5μ.

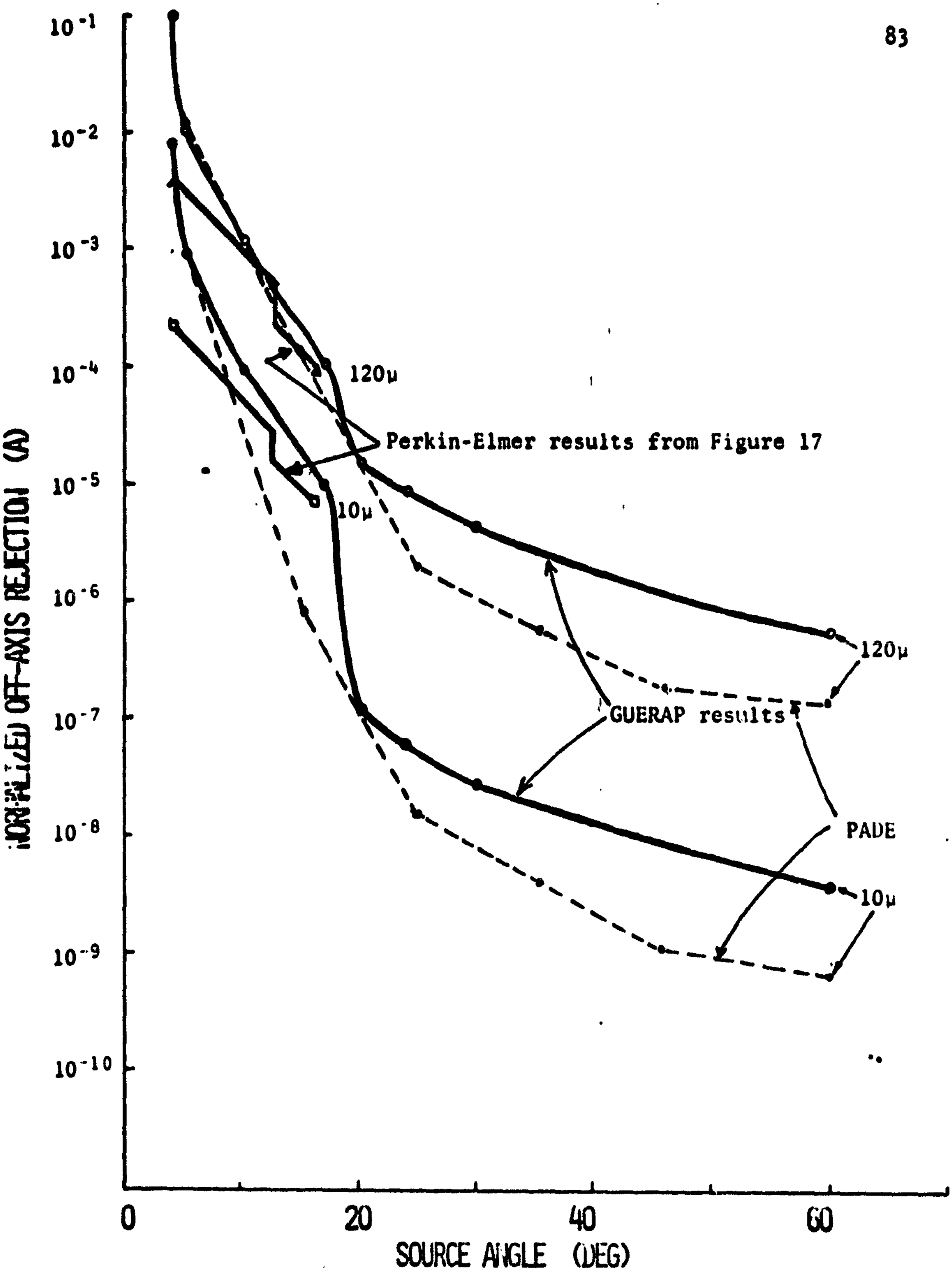

Fig. 35. Comparison of PADE, GUERAP II and Perkin-Elmer's Calculations.

First, the Arizona version of GUERAP II was found to produce inconsistent results for multiple diffraction, although single diffraction tests out fine. Second, due to the quantum nature of the PADE algorithm, its calculation will tend to be low for multiple diffraction. A future version of the program will minimize this effect.

6.5 ANALYTICAL RESULTS FOR STRUTS

6.5.1. Introduction. The diffraction from the struts will produce a sharply peaked pattern in the image plane. It would be economically infeasible to use the computer program to reproduce the fine scale structure of this pattern due to the very small sampling interval that would be required for the azimuthal angle. However, the geometry of the struts permits the use of a modified Fraunhofer approximation to the diffraction integral. Therefore, an accurate analytical expression for the diffraction from an equivalent tilted slit can be found.

6.5.2. Angular Spectrum Approach to Diffraction. The standard Fraunhofer formula expresses the diffraction field in the focal plane perpendicular to the optical axis in terms of a scaled Fourier transform of the aperture function a(x,y).[18]

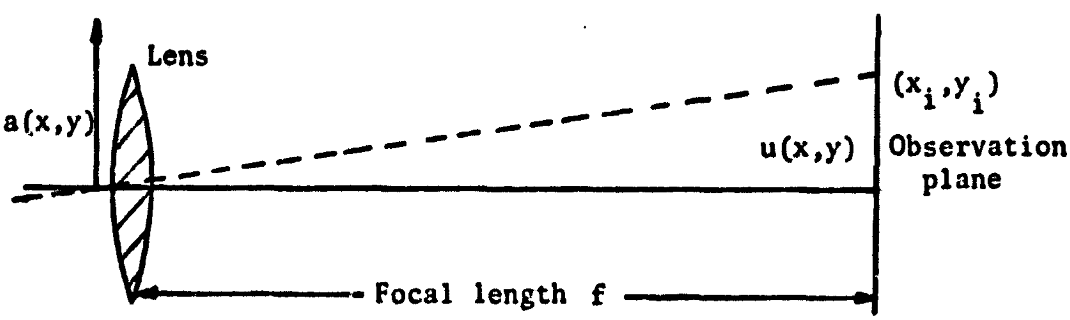

Fig. 36. Usual Fraunhofer Diffraction Geometry.

where

$$u(x,y) \propto A\left(\frac{x-x_i}{f}, \frac{y-y_i}{f}\right) \tag{43}$$

$$A(\xi,\eta) = \iint_{-\infty}^{\infty} a(x,y)\, e^{-ik(\xi x+\eta y)}\, dxdy \tag{44}$$

and (x_i,y_i) are the coordinates of the intersection of the incident ray through the center of the aperture with the observation plane. Note that the diffracted field is shift-invariant, i.e., the pattern shifts along with the incident point but does not change shape around it.

We could easily calculate the diffraction from a rectangular slit using the above formulation. Except that the approximations used in its derivation would restrict us to small regions around the optical axis, i.e., small angles of incidence and diffraction. Tilting the slit by a large angle (≈68°) is equivalent to large incident and diffraction angles, a violation of the usual Fraunhofer assumptions. However, it is possible to find a similar expression for the diffracted field on a hemisphere of radius f centered on the aperture, that is accurate for large angles.[19] This approach is based on the angular spectrum of plane waves and expresses the field in terms of direction cosines instead of spatial coordinates.

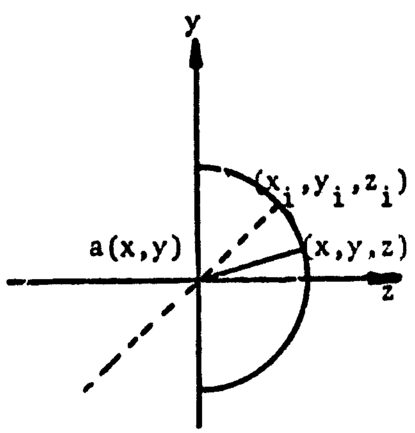

$$\alpha = \frac{x}{f}, \quad \alpha_i = \frac{x_i}{f}$$

$$\beta = \frac{y}{f}, \quad \beta_i = \frac{y_i}{f}$$

$$\gamma = \frac{z}{f}, \quad \gamma_i = \frac{z_i}{f}$$

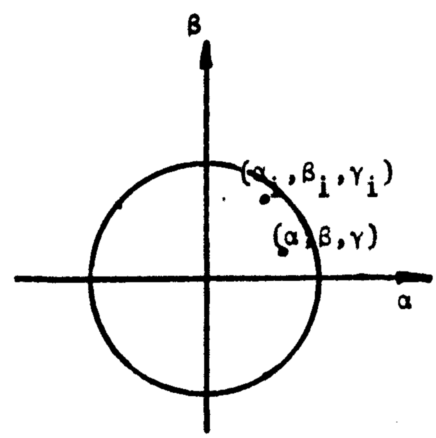

Fig. 37. Real Space

Fig. 38. Direction Cosine Space

The field on the hemisphere is now proportional to:

$$A(\alpha-\alpha_i\ ,\ \beta-\beta_i)$$

and therefore shift-invariant in direction cosine space.

The full expression for the field is given by:

$$u = Q\frac{e^{ikf}}{i\lambda f}\ A(\alpha-\alpha_i\ ,\ \beta-\beta_i) \tag{45}$$

where Q is an obliquity factor that depends on the Green's function used in the basic scalar-diffraction integral. For the Fresnel-Kirchhoff theory

$$G = \frac{e^{ikr}}{r}\quad ,\quad Q = \frac{\gamma+\gamma_i}{2} \tag{46}$$

where γ is the z-direction cosine of the observation point and γ_i of the incident point. In the diffraction theory of Rayleigh and Sommerfeld, the Green's function is selected in order to remove the mathematical inconsistency of the Fresnel-Kirchhoff theory by requiring that only the field and not its normal derivative need to be known at the aperture. The Green's function that accomplishes this vanishes everywhere in the aperture plane:

$$G = \frac{e^{ikr}}{r} - \frac{e^{ik\tilde{r}}}{\tilde{r}} \tag{47}$$

where $\tilde{r}$ is the distance from the point in this aperture to the image formed by the aperture plane of the observation point. This leads to an obliquity factor given simply by:

$$Q = \gamma \tag{48}$$

The difference between the two forms of the obliquity factor can best be shown in a polar diagram for $\gamma_i = 1$.

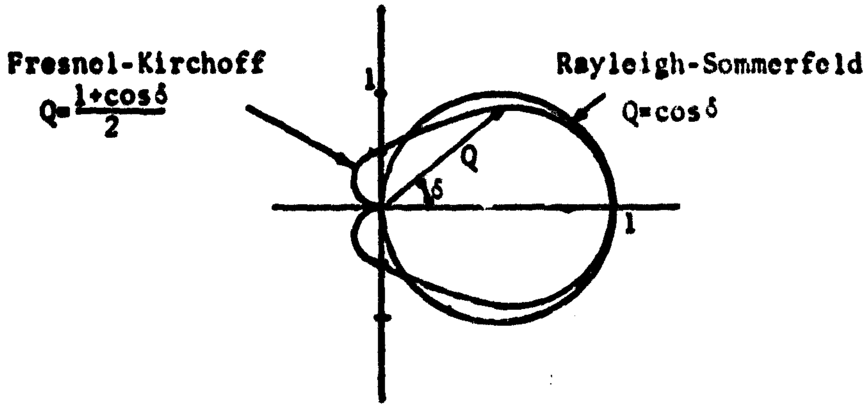

Fig. 39. The Two Different Obliquity Factors.

Substantially different predictions would occur at large diffraction angles. Experimental data in this region is needed to decide between the two. In the absence of such data, we have chosen to use the Fresnel-Kirchhoff obliquity factor since it is based on the same theory as the computer algorithm and therefore will permit checking of the analytical and numerical results.

6.5.3. The Rectangular Slit. The diffraction from one strut can be equivalently represented by its complement, a rectangular slit. The field due to the three struts will be the sum of three properly oriented slits. It will be sufficient for our purposes to consider just the field due to one strut.

The transmission function for a rectangular slit can be written in the form

$$a(x,y) = \mathrm{RECT}\left(\frac{x}{\Delta x}\right) \cdot \mathrm{RECT}\left(\frac{y}{\Delta y}\right) \qquad (49)$$

$$\mathrm{RECT}(x) = \begin{cases} 1 & |x| < \frac{1}{2} \\ \frac{1}{2} & |x| = \frac{1}{2} \\ 0 & |x| > \frac{1}{2} \end{cases}$$

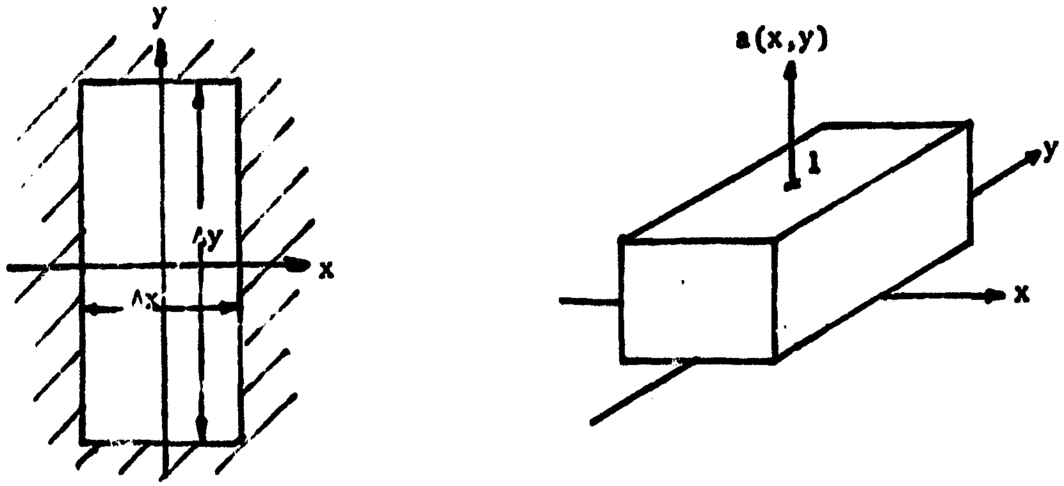

Fig. 40. Transmission Function for Rectangular Slit.

The spectrum of this function is:

$$A(\xi,\mu) = [\Delta x \cdot \mathrm{sinc}(\xi\Delta x/\lambda)] \cdot [\Delta y \cdot \mathrm{sinc}(\eta\Delta y/\lambda)] \tag{50}$$

where

$$\mathrm{sinc}(x) = \frac{\sin(\pi x)}{\pi x} \tag{51}$$

Upon substitution, the diffracted field is found to be:

$$u = \frac{(\gamma+\gamma_i)\Delta x\Delta y}{i2\lambda f} \cdot [\mathrm{sinc}\ \Delta x(\alpha-\alpha_i)/\lambda] \cdot \mathrm{sinc}[\Delta y(\beta-\beta_i)/\lambda] \cdot e^{ikf} \tag{52}$$

and the irradiance is given by:

$$E = \left\{\frac{(\gamma+\gamma_i)\Delta x\Delta y}{2\lambda f} \cdot \mathrm{sinc}[\Delta y(\alpha-\alpha_i)/\lambda] \cdot \mathrm{sinc}[\Delta y(\beta-\beta_i)/\lambda]\right\}^2 \tag{53}$$

If $\Delta y >> \Delta x$, then the diffraction pattern has the form of straight short and long diffraction spikes in direction cosine space. However, the spikes will appear curved when projected on the hemisphere depending on how the observer is oriented with respect to the plane of the aperture.

The direction cosines can be expressed in terms of the off-axis and azimuthal angles, θ and ϕ respectively.

C-2

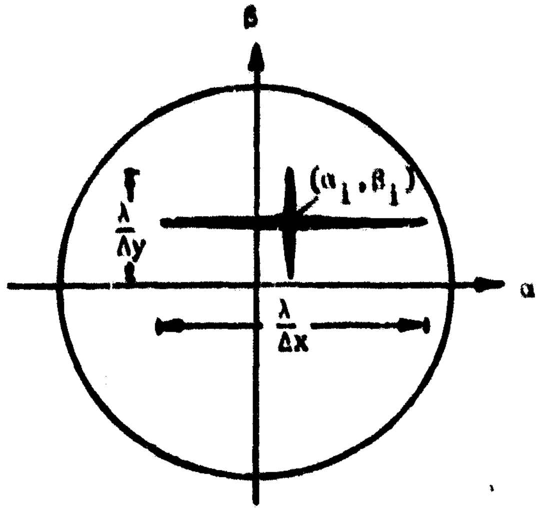

Fig. 41. Diffraction Spikes in Direction Cosine Space.

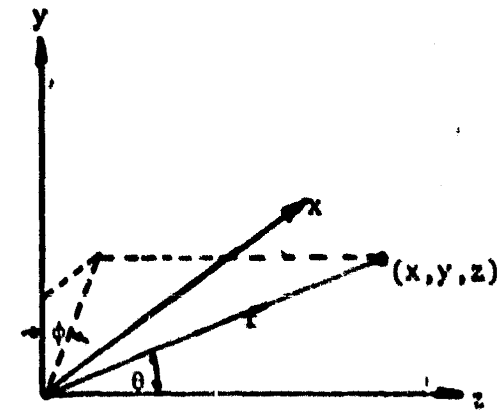

Fig. 42. Definition of System Off-axis and Azimuth Angles.

$$\alpha = \frac{x}{f} = \sin\theta\sin\phi \tag{54}$$

$$\beta = \frac{y}{f} = \sin\theta\cos\phi \tag{55}$$

$$\gamma = \frac{Y}{f} = \cos\theta$$

The equation of the long spike is:

$$\beta = \beta_i \tag{57}$$

For an on-axis detector $\theta=0$, therefore this condition becomes

$$\beta_i = \sin\theta_i\cos\phi_i = 0 \tag{58}$$

If the source is off-axis, i.e., $\theta = 0$, then the detector will pick up the spike when

$$\cos\phi_i = 0 \tag{59}$$

or for source azumuthal angles $\phi_i = \pm 90°$. The two halves of the spike are diametrically opposed since $\phi_i^+ - \phi_i^- = 180°$.

The peak of the long spike can be expressed in terms of the attenuation factor $A(\theta)$ for a small infinitesimal on-axis detector of area A_o. Let A_o be the area of the collecting aperture, then

$$A(\theta) = \frac{P(\theta)}{\Omega_o \cdot P(0)} = \frac{|f \cdot u|^2}{A_o} \qquad \begin{cases} \Omega = \dfrac{A_o}{f^2} \\ P(\theta) \propto A_o |u|^2 \\ P(0) \propto A_o \end{cases} \tag{60}$$

with

$$\beta = \beta_i \ , \ \alpha = 0 \ , \ \alpha_i = \sin\theta_i \ , \ \gamma_i = \cos\theta_i \tag{61}$$

$$A(\theta_i) = \frac{1}{A_o} \left\{ \frac{(1+\cos\theta_i)\Delta x \Delta y}{2\lambda} \ \mathrm{sinc}[\Delta x \cdot \sin(\theta_i)/\lambda] \right\}^2 \tag{62}$$

The envelope of this is:

$$\frac{1}{A_o} \left[\frac{(1+\cos\theta_i)\Delta y}{2\pi \cdot \sin\theta_i} \right]^2 = \frac{1}{A_o} \left[\frac{\Delta y}{2\pi \cdot \tan(\theta_i/2)} \right]^2 \tag{63}$$

substituting in the following values:

$$\begin{cases} \theta_i = 5° \\ \Delta y = 20\text{cm} \\ A_o = 2400\text{cm}^2 \end{cases} \qquad A(\theta_i) = 2.21 \tag{64}$$

It is important to point out that the envelope of the spike is rigorously independent of wavelength only for a point detector.

6.5.4. The Tilted Strut. The value of $A(\theta_i)$ calculated from the analytical expression is about three orders of magnitude larger than that calculated by the PADE program under the same conditions. At first, it was thought that one of the calculations must be in error. However, it turns out the discrepancy is due to the fact that the tilt of the strut was not taken into account in the analytical solution.

Tilting the strut or aperture plane is equivalent to a rotation of the incident and observation points. Let w be the angle of rotation of the strut.

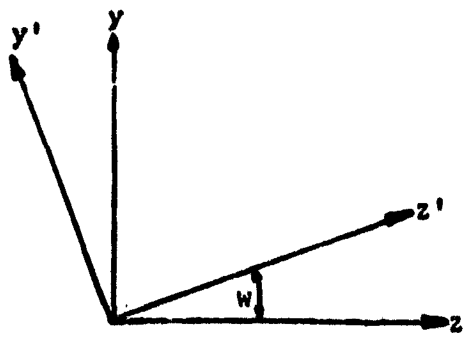

Fig. 43. Coordinate System Rotation.

Then the new coordinate system is related to the old by:

$$x' = x \tag{65}$$

$$y' = y \cos w - z \sin w \tag{66}$$

$$z' = y \sin w + z \cos w \tag{67}$$

The new direction cosines in terms of the original off-axis and azimuthal angles become:

$$\alpha = \sin\theta \sin\phi \tag{68}$$

$$\beta = \sin\theta \cos\phi \cos w - \cos\theta \sin w \tag{69}$$

$$\gamma = \sin\theta \cos\phi \sin w + \cos\theta \cos w \tag{70}$$

and the condition for an on-axis detector being at the peak of the long spike is again

$$\beta = \beta_i \quad \text{with} \quad \theta = 0 \tag{71}$$

this becomes

$$-\sin w = \sin\theta_i \cos\phi_i \cos w - \cos\phi_i \sin w \tag{72}$$

or

$$\cos\phi_i = \frac{\sin w(1-\cos\phi_i)}{\cos w \sin\phi_i} = -\tan w \tan(\phi_i/2) \tag{73}$$

Therefore, the source azimuthal angle at which this would occur is a function of both the tilt of the strut and the off-axis angle:

$$\phi_i = \cos^{-1}[\tan w \cdot \tan\phi_i/2] \tag{74}$$

for $\theta = 5°$ and $w = 68°$

$$\phi_i = \pm 96.2° \tag{75}$$

The spike has shifted about 6° in azimuth due to the tilt of the strut and no longer forms a straight line since $\phi_i^+ - \phi_i^- \neq 180°$.

The PADF calculation was redone using the azimuthal angle determined precisely from the above formula and the value of $A(\theta_i)$ agreed closely with the analytical result.

6.6 CONCLUSIONS AND RECOMMENDATIONS

The diffraction due to the circular aperture is in most instances below the specification. However, the diffraction spikes from the struts are well above the spec's. Also their spatial characteristics will make them hard to differentiate from astronomical point sources. A possible solution to the strut problem is to serrate their edges in order to break up the phase addition across them. This is, in effect, an apodization technique which will not reduce the total energy diffracted by the strut, but will redistribute it in a smoother manner.

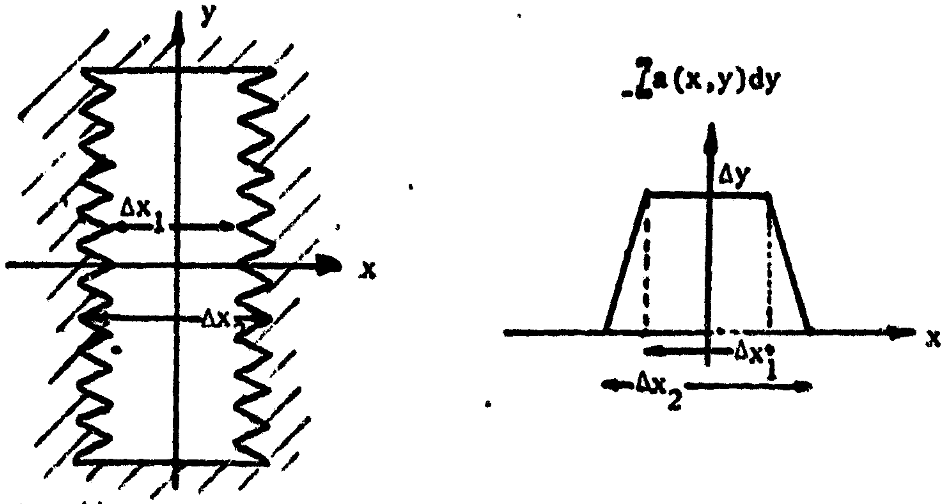

Fig. 44. Apodization with Serrated Edges.

The transmission function is effectively tapered such that $A(\theta)$ falls as $(\sin\theta)^{-4}$ instead of $(\sin\theta)^{-2}$ along the spike. A more detailed calculation[20] could be carried out to precisely determine what will be gained by serrating the struts.

If the stop of the system is shifted to the secondary mirror, the strut diffraction is unaffected. However, this should result in lowering the circular diffraction by making second order diffraction takeover at a smaller off-axis angle. The exact effect is hard to estimate since there is a possibility that more diffracting edges, i.e., the main baffle vanetips, might start to contribute. A more detailed calculation is needed.

7.0 COMBINED SCATTER AND DIFFRACTION RESULTS

The combined effects of scatter and diffraction are shown in Figs. 45 to 49. Tables 13 to 17 show the A(θ) values and percentages due to each method of propagation. Only at very large off-axis angles are the diffraction effects dominate, although they are significant at some other angles in some of the bands. These results do include the diffraction from the struts. However, these off-axis angles are in the meridional plane (azimuth = 180°), on the earth's side of the sunshield.

For certain azimuthal positions the diffraction from the struts will cause locally high peaks in the A(θ) values, which are not accounted for in these figures.

7.1 DIFFRACTED, THEN SCATTERED RADIATION

The effect of radiation which is first diffracted to and then scattered from the critical objects (secondary baffle and aperture stop) was not directly evaluated. However, an analysis of the APART and PADE outputs indicate the following:

1. Diffraction, then scatter, effects at 25° off-axis is not a significant propagation path (less than 1%).
2. Diffraction-scatter effects at 60° are comparable to or higher (10x) than the multiple scatter effects.

These results are preliminary and are based on the average incident irradiance, at the apertures or critical objects, which can vary considerably due to obscurations. It is possible that this type of propagation will be of some significance at angles greater than 40° where three consecutive black scattering surfaces are involved.

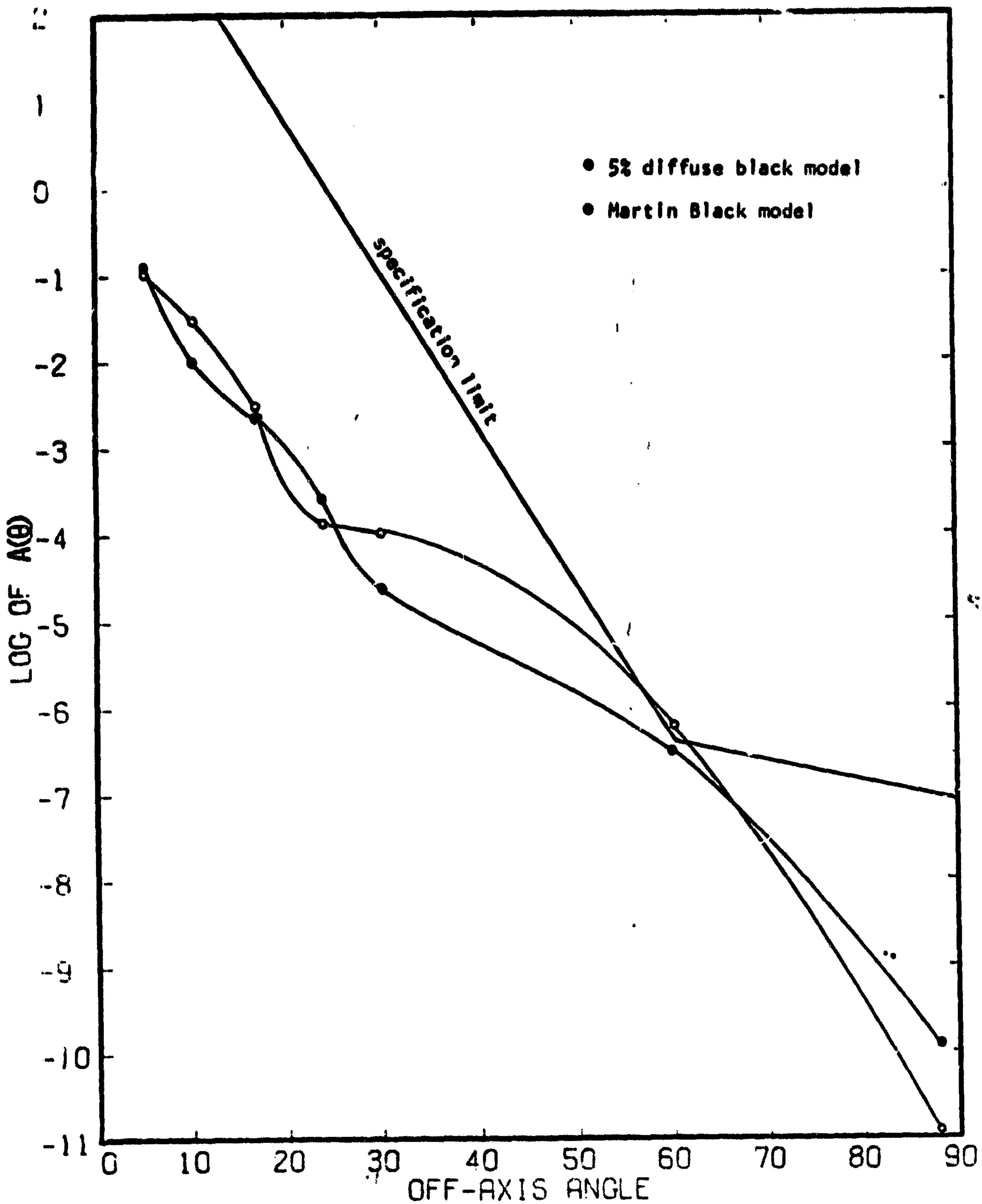

Fig. 45. 0.4-0.9μ Band, Scatter and Diffraction Combined.

Table 13. 0.4 - 0.9μ band Scatter and Diffraction

θ	5	10	17	24	30	60	88	98	108
Diffraction	6.3E-5	4.E-7	3.2E-9	6.3E-11	3.2E-11	3.5E-12	1.1E-12	1.E-20	1.4E-20
5% Diffuse	1.37E-1	1.10E-3	2.73E-3	2.65E-4	2.98E-7	4.63E-2	1.25E-11	9.62E-11	5.04E-11
Martin Black	1.12E-1	3.00E-2	2.43E-3	1.65E-4	1.33E-8	5.76E-8	3.76E-12	3.20E-11	1.95E-11

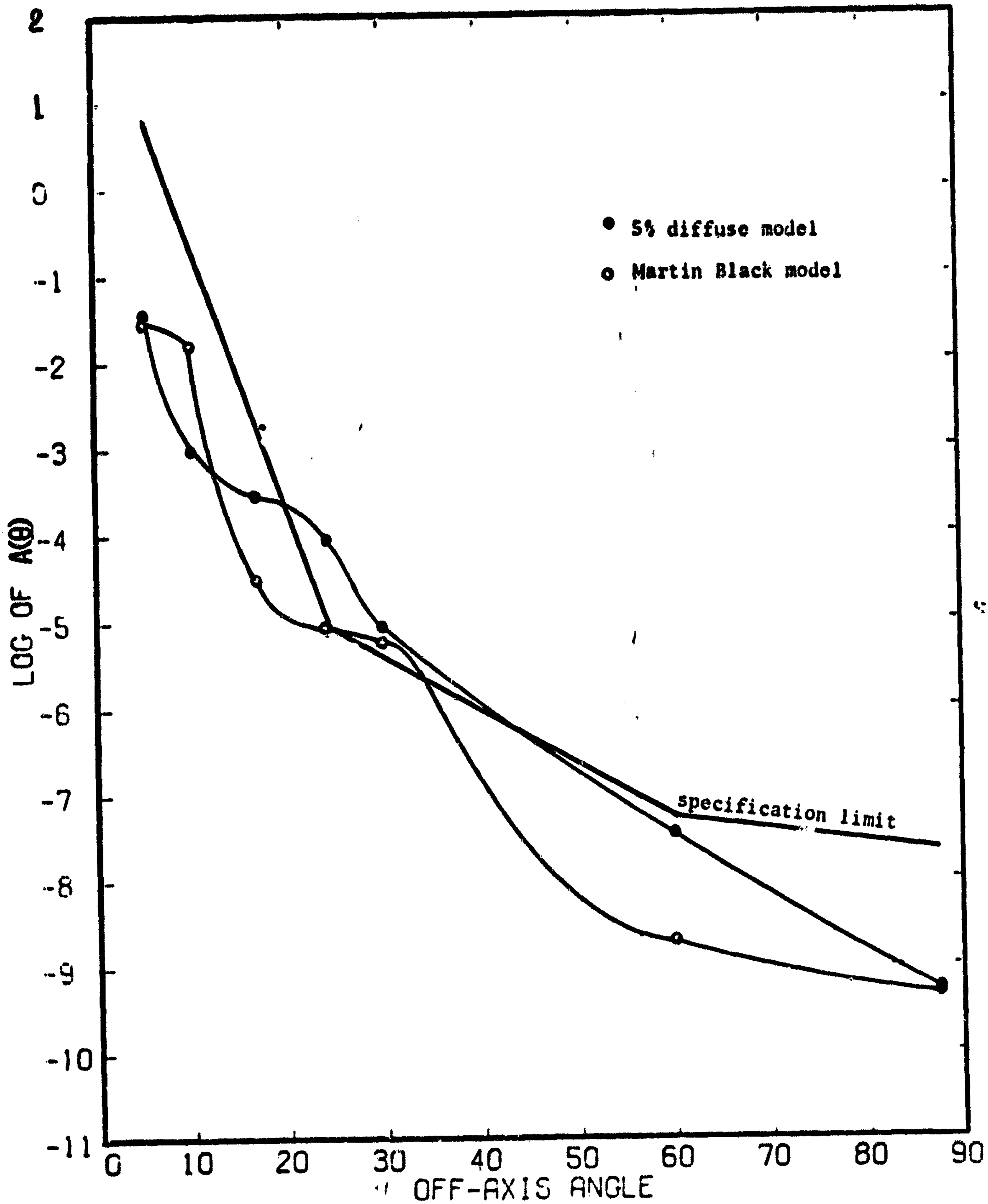

Fig. 46. 8 - 15μ Band, Scatter and Diffraction Combined.

Table 14. 8-15μ Band Scatter and Diffraction.

θ	5	10	17	24	30	60	88
Diffraction	1.3E-3	3.2E-5	1.3E-6	1.8E-8	1.E-8	1.3E-9	5.E-10
5% Diffuse	3.7E-2	8.8E-4	3.3E-4	9.5E-5	1.1E-5	4.2E-8	1.5E-11
∑	3.8E-2	9.1E-4	3.3E-4	9.5E-5	1.1E-5	4.33E-8	5.15E-10
% Diffraction	4.	4.	0.	0.	0.	3.	97.
% Scatter	96.	96.	100.	100.	100.	97.	3.
Martin Black	2.9E-2	1.9E-2	3.04E-5	1.4E-5	7.7E-6	8.2E-10	3.2E-13
∑	3.03E-2	1.9E-2	3.17E-5	1.4E-5	7.7E-6	2.12E-9	5.0E-10
% Diffraction	4.	0.	4.	0.	0.	61.	100.
% Scatter	96.	100.	96.	100.	100.	39.	0.

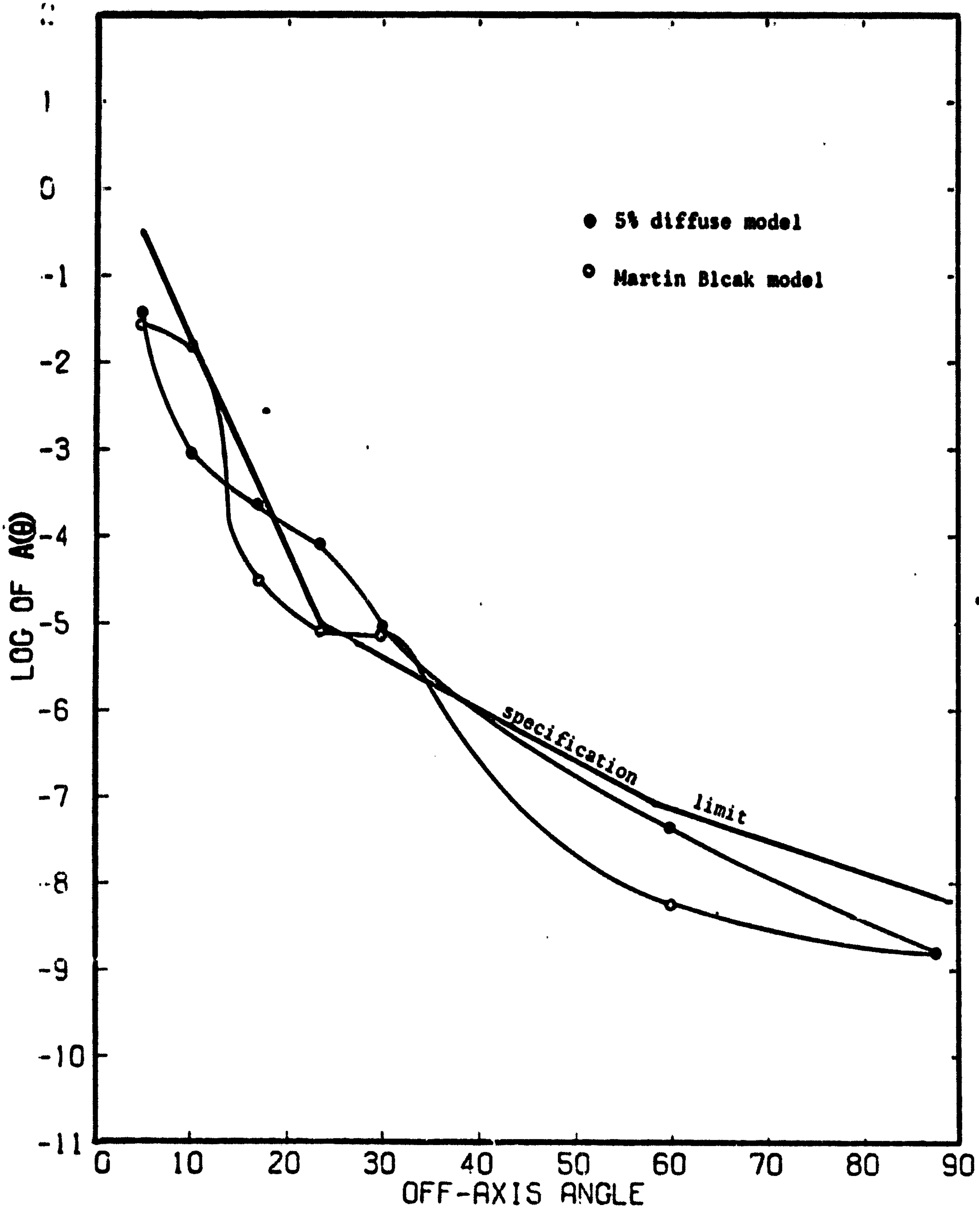

Fig. 47. 15 - 30μ Band, Scatter and Diffraction Combined.

Table 15. 15-30μ Band Scatter and Diffraction.

θ	5	10	17	24	30	60	88
Diffraction	2.E-3	1.E-4	4.E-6	8.E-8	4.E-8	5.E-9	1.6E-9
5% Diffuse	3.7E-2	8.8E-4	2.7E-4	9.5E-5	1.03E-5	4.2E-8	3.5E-11
$\sum$	3.9E-2	9.8E-4	2.7E-4	9.5E-5	1.03E-5	4.7E-8	1.6E-9
% Diffraction	5.	10.	0.	0.	0.	12.	98.
% Scatter	95.	90.	100.	100.	100.	88.	2.
Martin Black	2.9E-2	1.9E-2	2.5E-5	1.4E-5	7.6E-6	8.2E-10	3.2E-13
$\sum$	3.1E-2	1.9E-2	2.9E-5	1.4E-5	7.64E-6	8.8E-9	1.6E-6
% Diffraction	6.	0.	14.	0.	0.	86.	100.
% Scatter	94.	100.	86.	100.	100.	14.	0.

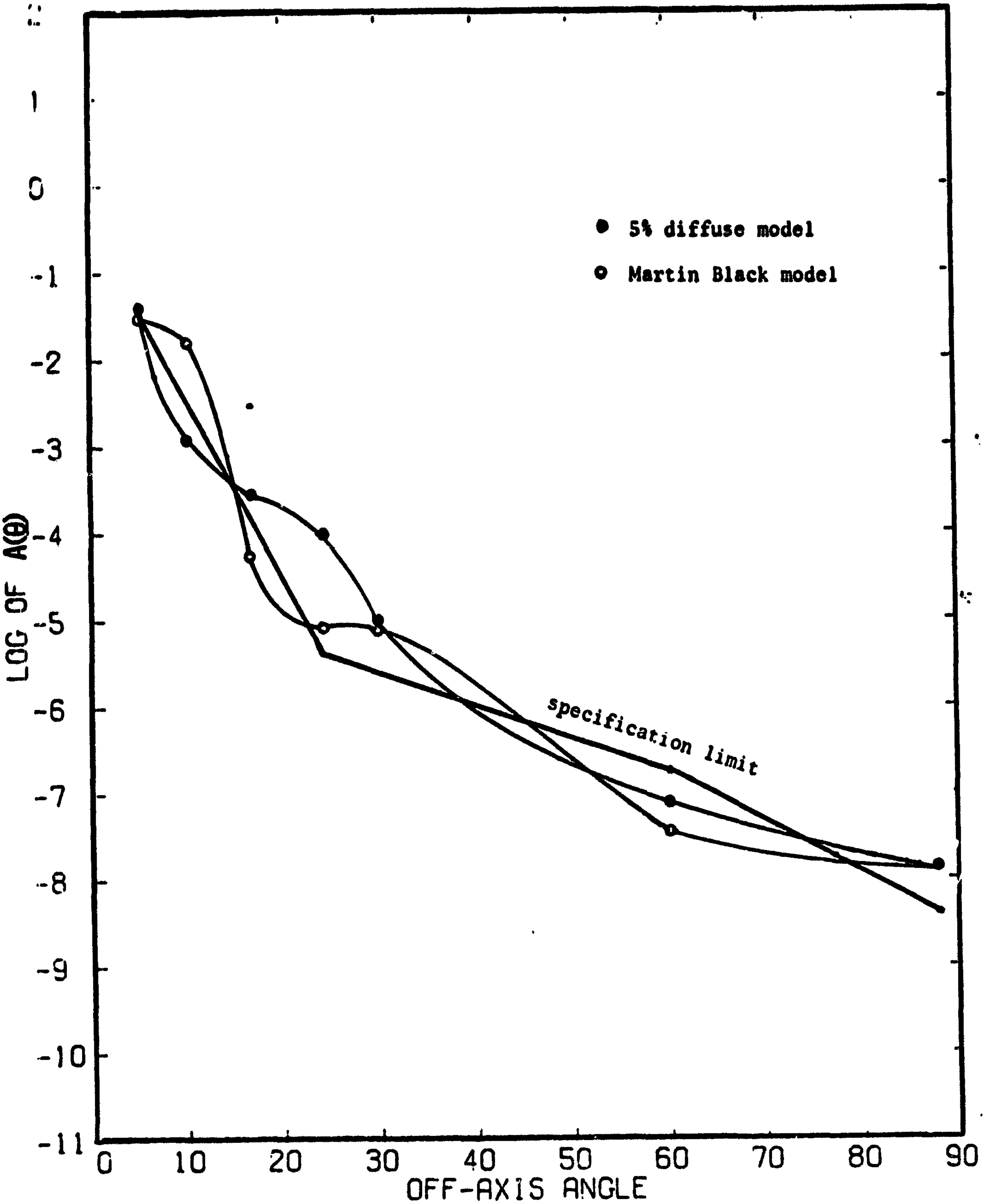

Fig. 48. 48 - 81μ Band, Scatter and Diffraction Combined.

Table 16. 48-81μ Band Scatter and Diffraction.

θ	5	10	17	24	30	60	88
Diffraction	6.3E-3	4.5E-4	2.8E-5	7.0E-7	4.0E-7	3.5E-8	1.4E-8
% Diffuse	3.7E-2	8.8E-4	2.6E-4	9.5E-4	9.8E-5	4.2E-8	1.5E-11
$\sum$	4.3E-2	1.33E-3	2.9E-4	9.6E-5	9.8E-5	7.7E-8	1.4E-8
% Diffraction	15.	34.	10.	7.	0.	45.	100.
% Scatter	85.	66.	90.	93.	100.	55.	0.
Martin Black	2.9E-2	1.9E-2	2.3E-5	1.4E-5	6.9E-6	8.2E10	3.2E-13
$\sum$	3.5E-2	1.9E-2	6.1E-4	1.4E-5	7.3E-6	3.6E-8	1.8E-13
% Diffuse	18.	0.	46.	0.	5.	97.	100.
% Scatter	82.	100.	54.	100.	95.	3.	0.

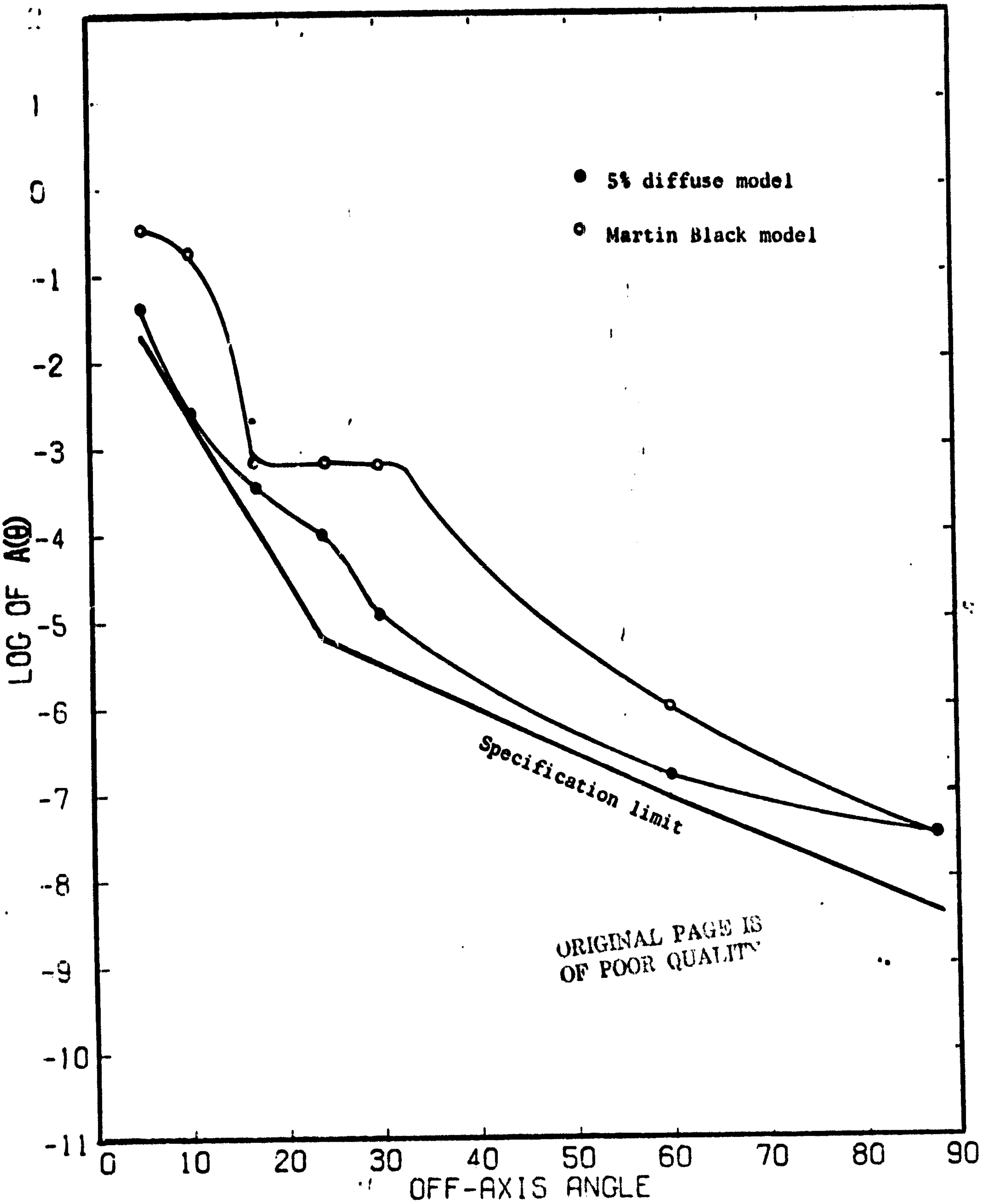

Fig. 49. 87 - 118μ Band, Scatter and Diffraction Combined.

Table 17. 87-118μ Band Scatter and Diffraction.

θ	5	10	17	24	30	60	88
Diffraction	1.E-2	1.E-3	8.E-5	2.E-6	1.E-6	1.E-7	3.2E-8
5% Diffuse	3.7E-2	8.8E-4	2.6E-4	9.5E-5	1.1E-5	4.2E-8	1.5E-11
$\sum$	4.7E-2	1.9E-3	3.4E-4	9.7E-5	9.9E-5	1.4E-7	3.2E-8
% Diffraction	21.	53.	24.	2.	1.	71.	100.
% Scattering	79.	47.	76.	98.	99.	29.	0.
Martin Black *10	2.9E-1	1.9E-1	7.2E-4	7.2E-4	6.9E-4	8.2E-7	3.2E-10
$\sum$	3.0E-1	1.9E-1	8.0E-4	7.2E-4	6.9E-4	9.2E-7	3.2E-8
% Diffraction	3.	0.	10.	0.	0.	11.	99.
% Scattering	97.	100.	90.	100.	100.	89.	1.

8.0 SUMMARY AND CONCLUSIONS

The stray-light analysis comparison with PE shows very strong agreement, even though the resolution and number of surface elements were more elaborate in the present analysis to account for many fine structures in the system. There is a considerable difference in the $A(\theta)$ when a 5% diffuse is compared to Martin's black coating. The $A(\theta)$ values are usually lower with Martin Black; the exception being at 10°.

The forward scatter off the secondary baffle, the backscatter off the aperture stop and diffraction from the aperture stop, secondary baffle, and the struts are the major contributors of unwanted energy.

The primary scattering object, which causes the $A(\theta)$ values to be higher than the spec line, is the forward scatter off the secondary baffle. This requires a redesign. There are two choices possible:

1. Shift the stop location to the secondary mirror. The forward scatter path would be eliminated. In addition, the scatter path from the original stop and structures would also be eliminated along with the diffraction effects from the present aperture stop. The diffraction contribution from the secondary mirror (the new stop) would increase some, but it will not be as much as the present values from the stop near the primary. This is the recommended solution. The expected result is an estimated decrease in the $A(\theta)$ value by a factor of 100.
2. Redesign the secondary baffle. PE originally recommended a more cylindrical design for the secondary baffle. This recommendation is on sound principles and should have been implemented.

By making the baffle more cylindrical, one or two vanes can be used to block out almost all of the forward near-specular scatter from the secondary--the major path at almost all angles.

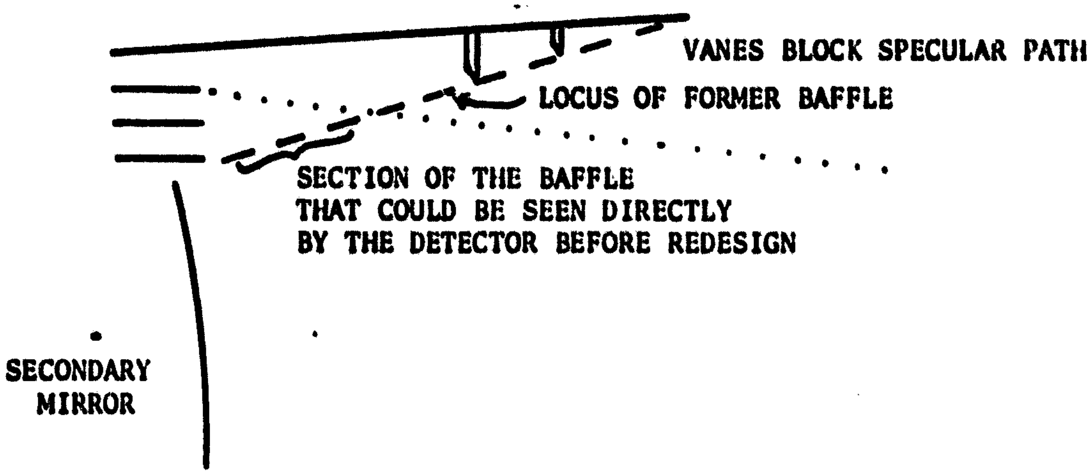

Fig. 50. The More Cylindrical Secondary Baffle.

The direct back scatter to the detectors can also be reduced by having the incident energy fall on the cylindrical wall which is out of the field of view of the detectors.

This change will not alter the backscatter from the aperture stop nor its diffraction effects. However, diffraction is a major problem only at large off-axis angles, and aperture backscatter is a problem only in the 17° to 24° range.

It should be obvious that both improvements are desirable. The result of making both changes would leave the diffraction from the secondary baffle and the spikes from the struts as problem areas. As discussed in the section on diffraction, these are localized effects. Also, it <u>may</u> be possible to dissipate the energy in the spike over a broader collector area. It would probably keep the diffracted energy at least closer to the spec line if not below it.

The overall design is not an optimum one for stray-light suppression; Cassegrain designs seldom are. In an ideal baffled system, the detectors see only the imaging surfaces and the cavity in its immediate location, which does not receive significant amounts of unwanted energy. This usually involves some type of reimaging system, with field stops and Lyot stops. Then the A(θ) values are determined by 3rd order diffraction (and higher) or by scatter from the imaging elements.

The following has been reserved for last with hopes that it would carry the greatest lasting impact. The BRDF values used were taken at 10.6 μ and extrapolated to 120 μ. Over this range the "hemispherical diffuse" has increased by more than a factor of 20. It is highly unlikely that the BRDF profiles remain anywhere near constant over this range. It is STRONGLY recommended that high priority be placed on having BRDF measurements made at long wavelengths; both on Martin Black and on the mirrors! Then the values used and calculated in this report can be related to the measured data to determine the actual performance of the system at the long wavelengths.

REFERENCES

1. Statement of Work #2-27282, dated April 27, 1978, for contract award NAS2-9966, issued by NASA-Ames Research Center.

2. IRAS Specification #2-26412

3. APART I input data from R. J. Noll, Perkin-Elmer letter no. 78-IRAS-157, Mag 12, 1978.

4. Noll, R. J., letter #78-IRAS-157 from Perkin-Elmer.

5. Infrared Astronomy Satellite (IRAS) Optical Subsystem (OSS) Off-axis Rejection Analysis, Perkin-Elmer Report No. 13616, Norwalk, Conn.

6. Ibid.

7. Ibid.

8. Georgia Tech Eng. Dept. Measurement.

9. Measured Data on Emissivity of Martin Black.

10. Sunshade Configuration, W. P. Deveraux, Report No. IRAS. WPD. 8256, Ball Brothers Research Corp., 2-2-78.

11. Goodman, J. W., Introduction to Fourier Optics, McGraw-Hill (1968) pg. 39.

12. Wolf, E., and E. W. Marchand, "Comparison of the Kirchhoff and the Rayleigh-Sommerfeld Theories of Diffraction at an Aperture," JOSA 54 (1964) pg. 587.

13. Sommerfeld, A., Optics, Academic Press (1954) pg. 249.

14. Wolf, E., and M. Born, Principles of Optics, Pergamon Press (1975) pg. 449.

15. Rubinowicz, A., "The Miyamoto-Wolf Diffraction Wave," Progress in Optics, Vol. IV, J. Wiley & Sons (1965) pg. 205.

16. Papoulis, A., System and Transforms with Application in Optics McGraw-Hill (1968) pg. 222.

17. Perkin-Elmer Corp. GUERAP II User's Guide SAMSO TR 73-309 (1974) pg. 56.

REFERENCES, Cont.

18. Gaskill, J. D., Linear Systems, Fourier Transform and Optics, J. Wiley & Sons (1978) pg. 375.

19. Harvey, J. E., Light-scattering Characteristics of Optical Surfaces, Ph. D. dissertation, University of Arizona (1976) pg. 30.

20. Peters, P. J., "Aperture Shaping - A Technique for the Control of the Spatial Distribution of Diffracted Energy," SPIE Proc. Vol. 107 (1977) pg. 63.

N81-29966

D2

APPENDIX A

A.0 SURFACE SCATTER MODELS

A.1 MIRROR SCATTER

The mirror scatter model used by Perkin-Elmer is

$$BRDF = \frac{1.75 \times 10^{-5}}{\theta} \qquad \text{(A-1)}$$

where θ is expressed in radians. This model has a θ^{-1} dependence on the scattering angle. This model yields satisfactory results at the 10.6μ wavelength as it tends to parallel other measured data we have seen. The θ dependence, however, changes with samples and wavelength. The shape of a typical scattering function also changes with the θ as can be seen in Fig. A1. Here, we notice that the scattering function becomes asymmetrical with incidence angle. The asymmetry can be removed when the data is replotted in a new coordinate set α, β, as shown below. The α,β coordinates and the measurement hemisphere is illustrated in Fig. A2. It has been shown by Harvey (1976) that scatter data from smooth samples is linear-shift invariant and can be plotted as a single profile of the BRDF in β-β_o space. We have taken the PE mirror scatter model and replotted it in β-β_o with their λ^{-2} scaling to use as the visible wavelengths BRDF (Fig. A3).

In our analysis, we have used PE's BRDF only scaled to the Harvey type β-β_o plot, however, we feel that it has several shortcomings. First, the wavelength scaling does not fit with the θ dependence they have chosen. Harvey has derived a scaling law which accounts for the magnitude and the grating effect (i.e., narrow-angle scatter at short wavelengths is a

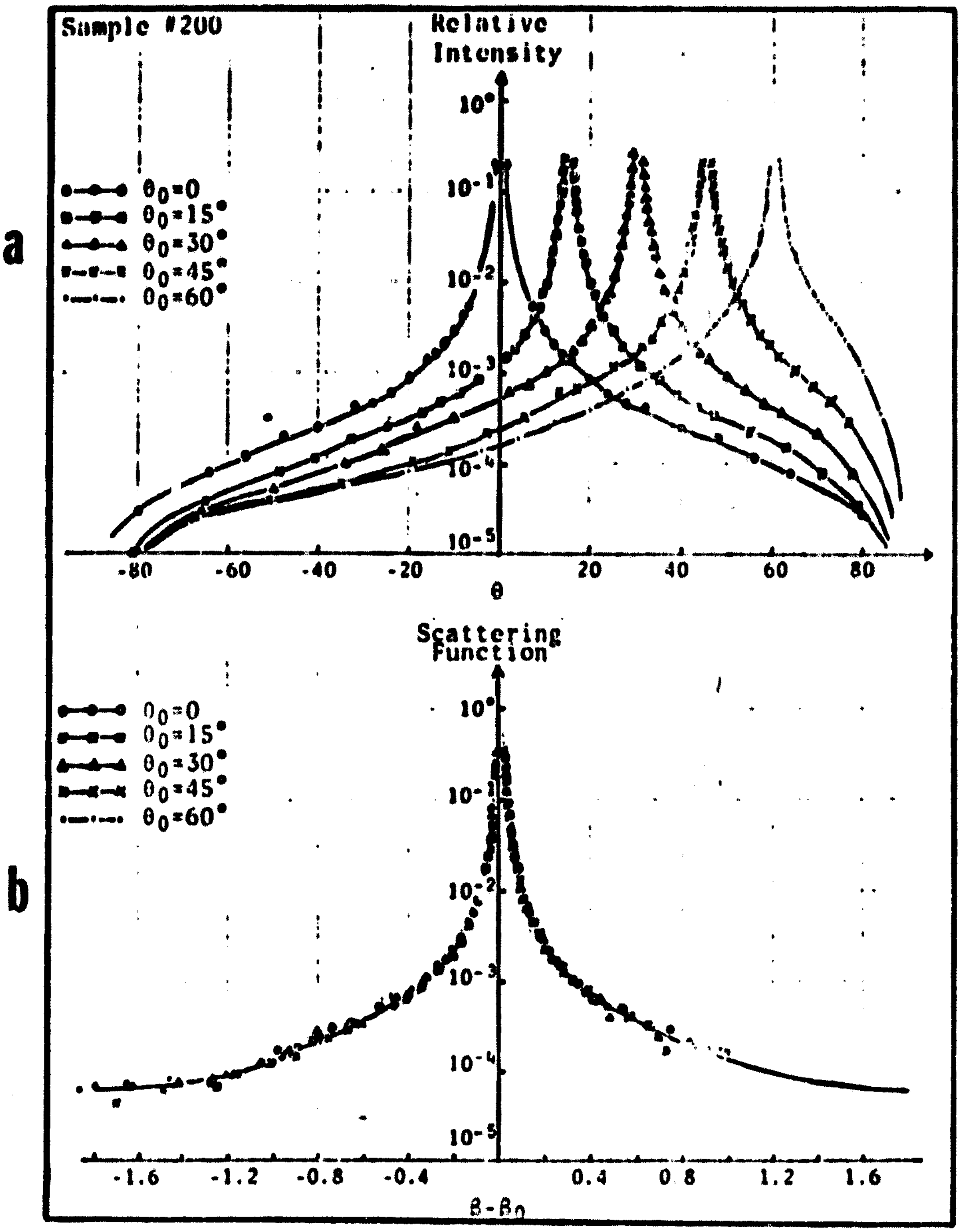

Fig. A1. Illustration of the Importance of the Coordinate System within which the Scattering Process is Discussed.

(a) Relative intensity plotted vs. scattering angle.
(b) Scattering function plotted vs. $\beta-\beta_0$.

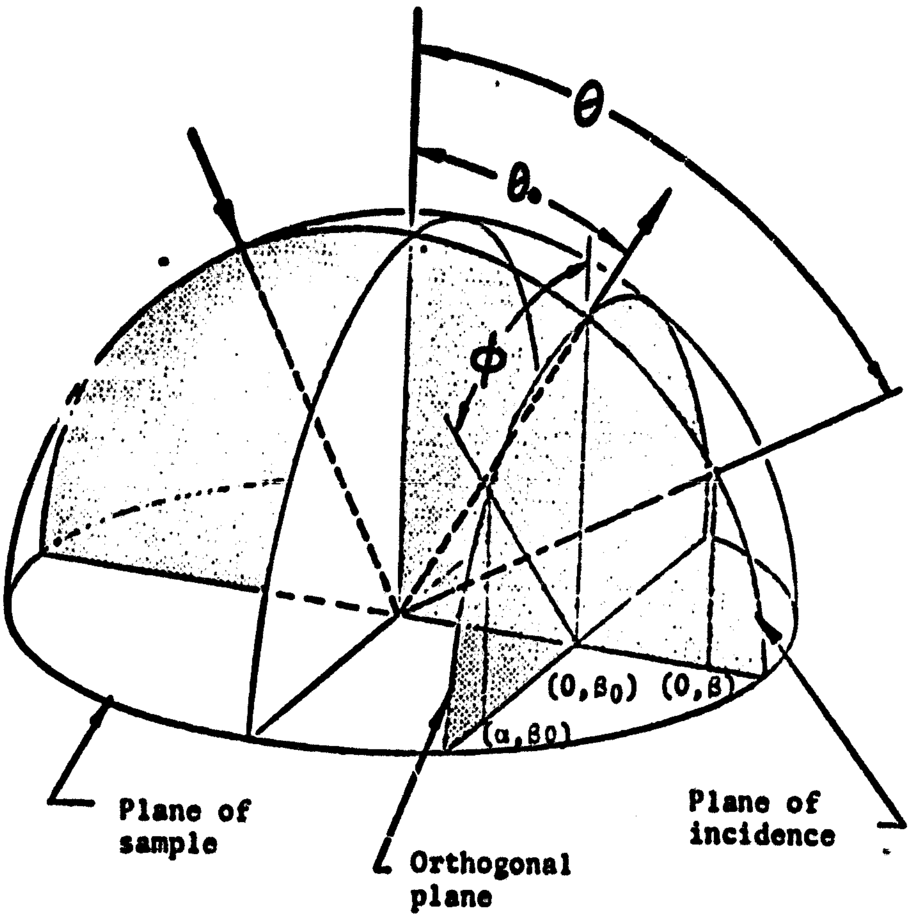

Fig. A2. Geometrical Configuration of Two Principal Planes in which the Scattered Light Field was Sampled.

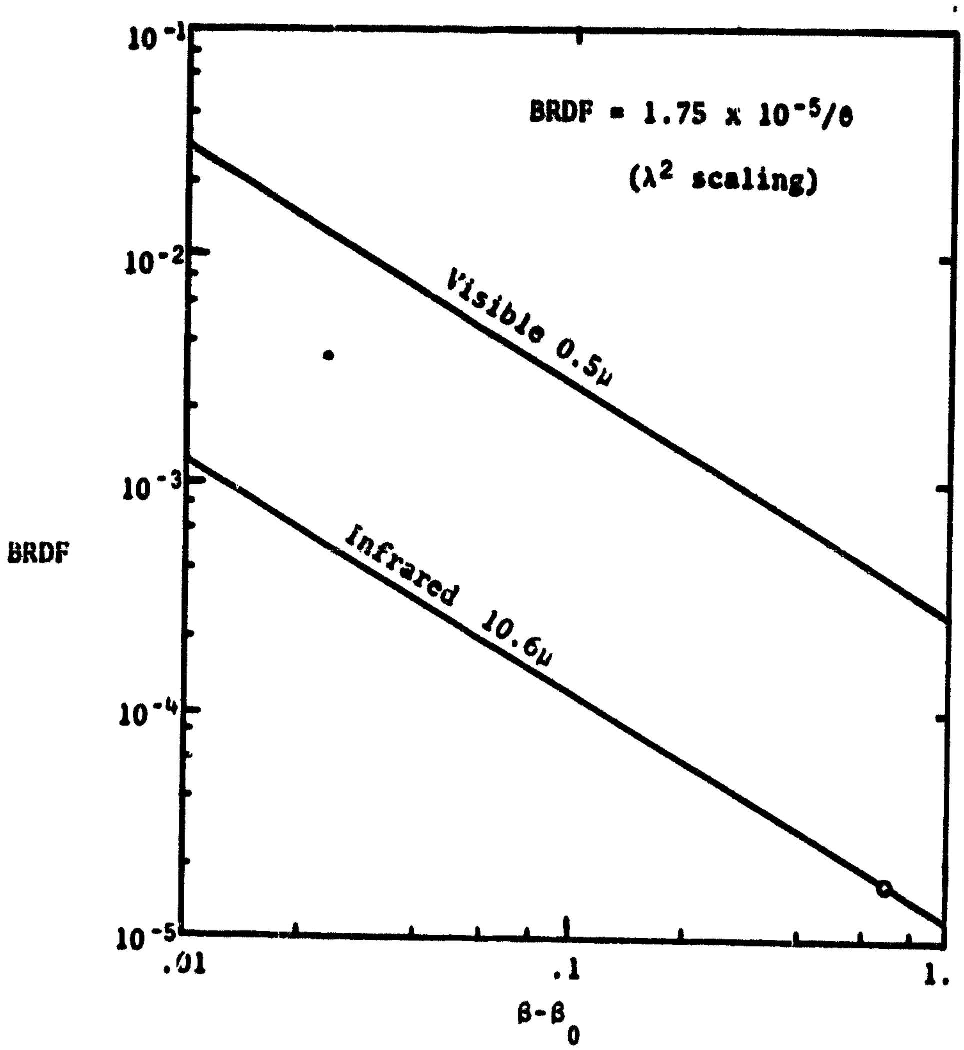

Fig. A3. BRDF of the Mirrors Used by APART.

predictor of wide-angle scattering at longer wavelengths). The scaling law is

$$S(\alpha,\beta;a\lambda) = \frac{1}{a^4} S(\frac{\alpha}{a}, \frac{\beta}{a}; \lambda) \quad \text{(A-2)}$$

where "a" is the wavelength change of the scaling. From this form, one can derive a λ scaling law that is a function of the slope of the BRDF as expressed in $\beta-\beta_o$ space;

$$S \approx (\beta-\beta_o)^m \quad \text{m is the slope of the BRDF curve} \quad \text{(A-3)}$$

from the scaling law,

$$S(a\beta) = \frac{1}{a^4}\left(\frac{\beta-\beta_o}{a}\right)^m$$

$$S(a\beta) = \frac{1}{a^{4+m}} (\beta-\beta_o)^m$$

$$S(a\beta) = \frac{1}{a^{4+m}} S(\beta) \quad \text{(A-4)}$$

Thus, for the Perkin-Elmer slope of θ^{-1}, the scaling law should have been $1/\lambda^3$. We feel, however, that the slope of the BRDF curve should have been more like $\theta^{1.8}$ to θ^{-2} which yields a scaling law of $1/\lambda^2$. This slope is more in line with those that we have seen for visible scattering data. The effect of using PE's scaling law is that the visible BRDF's seem to be pessimistic for near and large-angle scattering (Fig. A4). With the analysis of the IRAS system based upon these scattering BRDF's, any tests on a real model will be subject to the BRDF's of the mirrors actually used and may vary considerably with the analysis presented here.

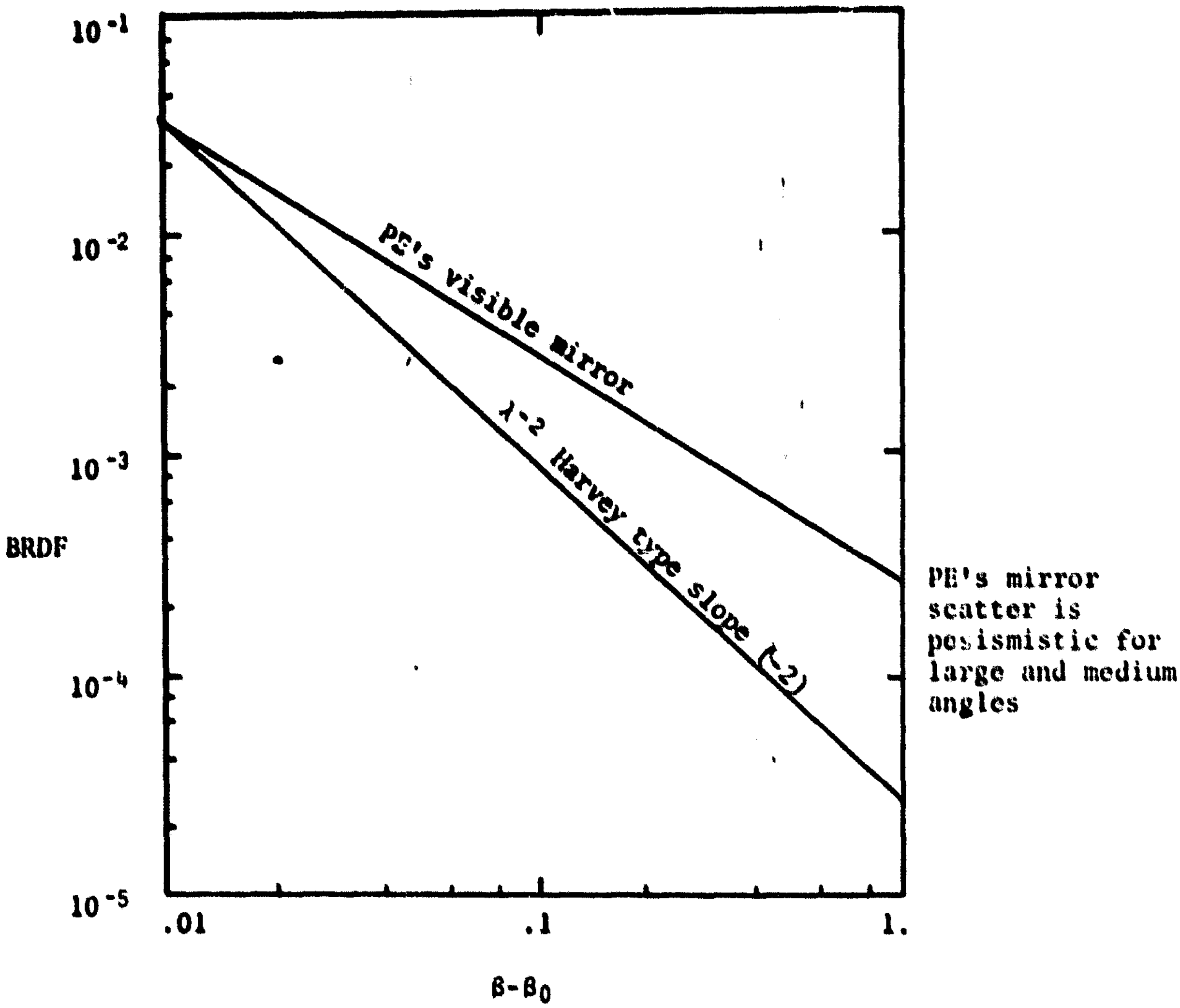

Fig. A4. BRDF at Visible Wavelengths as Arrived at by PE Scaling Law and λ^{-2} Scaling Law.

When scaling to longer wavelengths, another effect of the scaling may occur; the roll-off or "shoulder" to the BRDF curve may be shifted to larger angles for much longer wavelengths. The roll-off is usually not seen for visible and near IR wavelengths, because it occurs at very small angles (Fig. A5), but could be shifted far enough over to be picked up at the much longer IR bands. The only effect of this would be to lower the mirror scattering even more than the λ^2 wavelength scaling law suggests. At longer wavelengths the mirror-scatter contribution is negligible at most source angles, so this effect would make the mirror's contribution even less. Figure A6 illustrates the shoulder that is observed on some mirror samples.

A.2 BLACK SURFACE SCATTER

Perkin-Elmer used a 5% Lambertian reflectivity for their analysis. We have repeated the analysis with that reflectivity as well as using a mathematical model of Martin Black for comparison. The Martin Black model is based upon measured data on several samples. The key difference between a Lambertian model and the Martin Black model is that the real surfaces have higher BRDF's for non-normal incidence angles than do Lambertian surfaces.

This difference can have profound effects on the resultant scattered light in a system, depending on the scattering angles and vanes used on the baffles. Differences of up to two orders-of-magnitude have been noted on previous analyses where the two scattering models have been used. The use of the 5% diffuse model is an attempt to account for this large forward scattering, but yields pessimistic results when used for

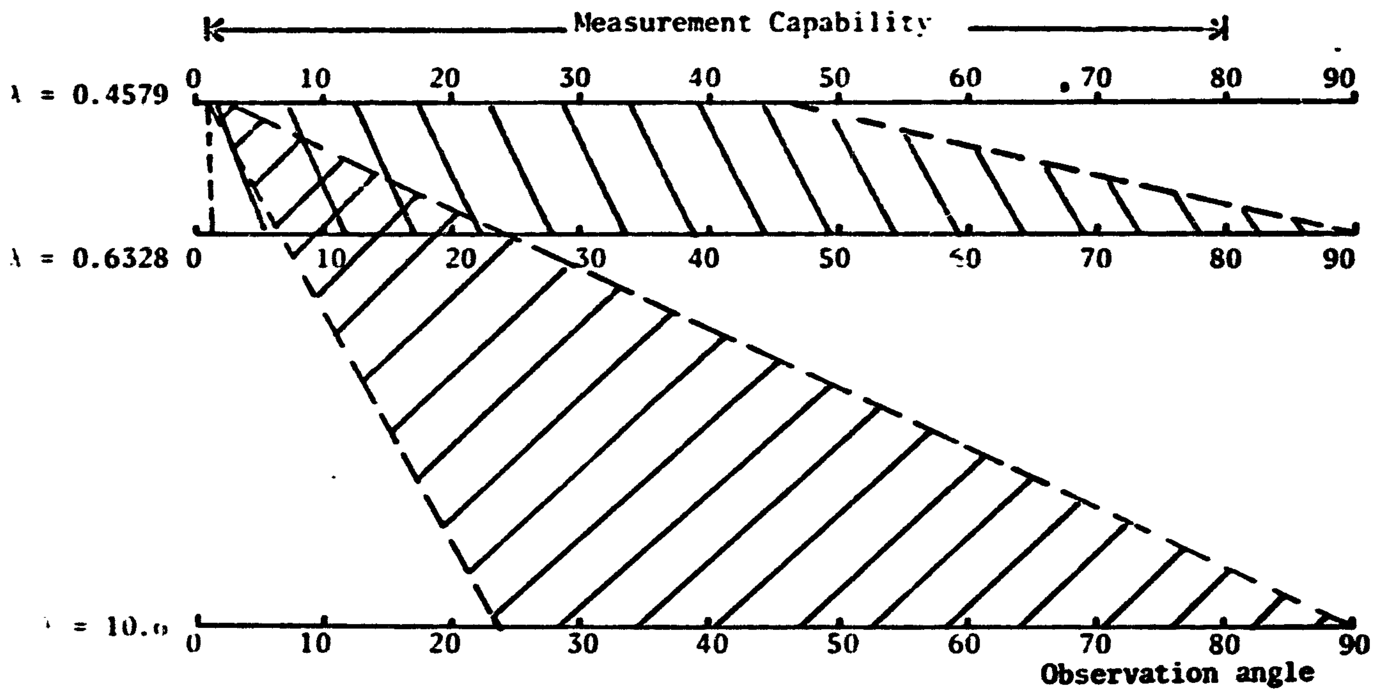

Fig. A5. Diagram Illustrating the Effects of the Wavelength Scaling Law.

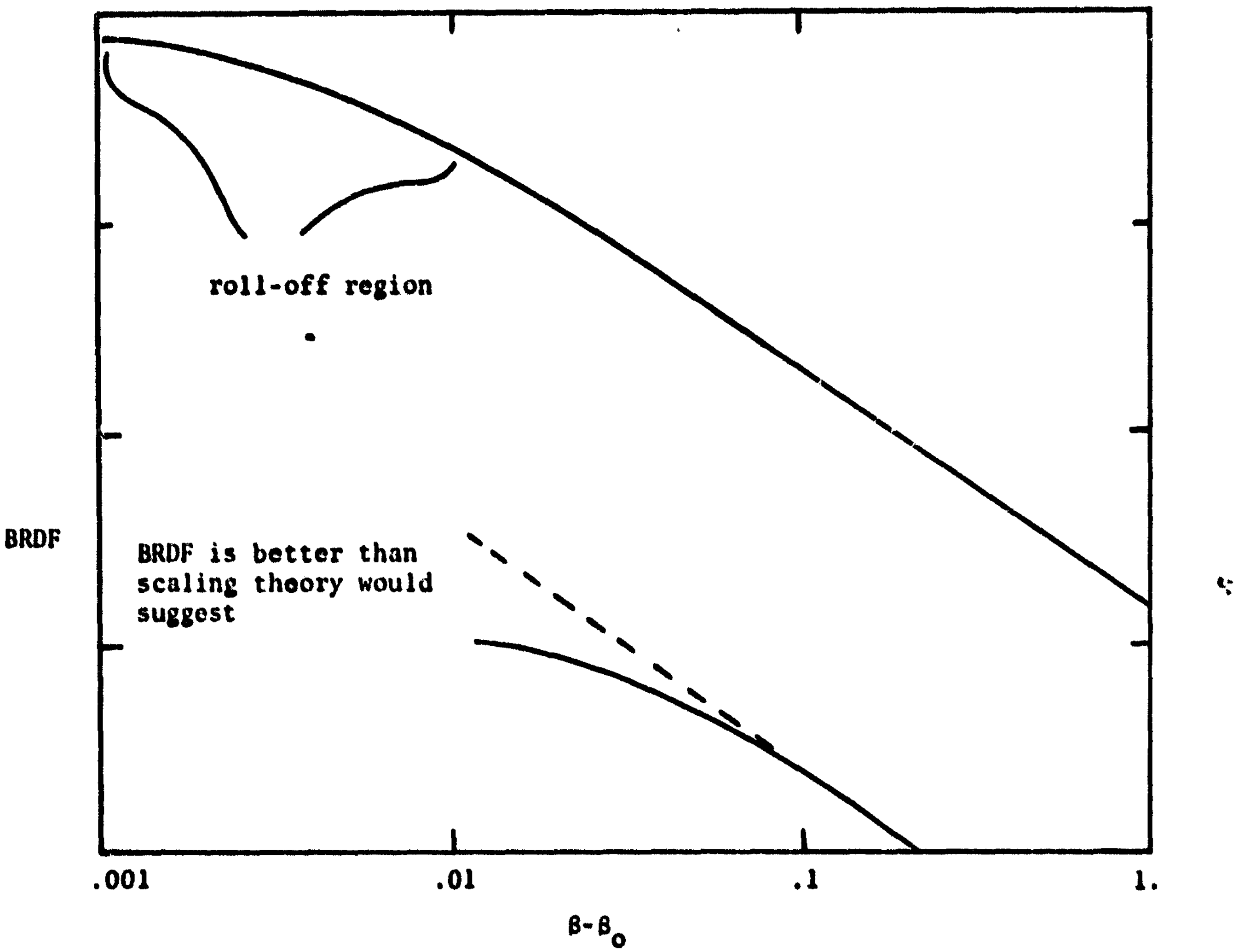

Fig. A6. Roll-off Region Shifted to Larger Angles when Wavelength Is Larger.

scattering from near-normal surfaces. At near-normal angles of incidence Martin Black has an equivalent reflectivity of 0.5% instead of the 5% that the PE data would suggest.

<u>Details of the Martin Black Scattering Model</u>

The scattering model is based on measured data from two Martin Black samples (Figs. A7 and A8). The backscatter is modeled as linear in $\beta-\beta_o$ space with an ordinate value predicted by the following equation for $\beta-\beta_o = 0.01$

$$\mathrm{BRDF} = 10^{\left[3.\left(e^{\frac{-|\theta-\pi/2|^{3.5}}{1.28}}-1.\right)\right]} \tag{A-5}$$

The slope of the backscatter curve is determined by a minimum BRDF input for the $\beta-\beta_o = 1.0$. This same slope is also used for the linear fall-off in α of α,β space.

The magnitude of increase in the BRDF for forward-scattering angles as a function of the incident angle θ_i is:

$$\mathrm{Log}(\Delta\mathrm{BRDF}) = 0.2 + 0.6\left(\frac{\theta_i}{\pi/2}\right)^4 \tag{A-6}$$

an increasing function with θ_i. The functional form of the forward scatter from the $\beta-\beta_o = 0.01$ to the maximum forward scatter angle is a quadradric function fit to the two end points;

$$\mathrm{BRDF}(\beta-\beta_o) = \mathrm{BRDF}(\beta-\beta_o=0.01) + \left[0.2 + 0.6\left(\frac{\theta_i}{\pi/2}\right)^4\right] * \left[\frac{\beta-\beta_o}{1-\beta_o}\right]^2;\ \text{for } \alpha-\alpha_o = 0. \tag{A-7}$$

An artist's conception of the surface contours of this rather complicated scattering function is shown in Fig. A9 for a θ_i of about 30°. A new three-dimensional scattering function is formed for each incident

Note: The forward scatter characteristics of this sample were used in the APART Martin Black model

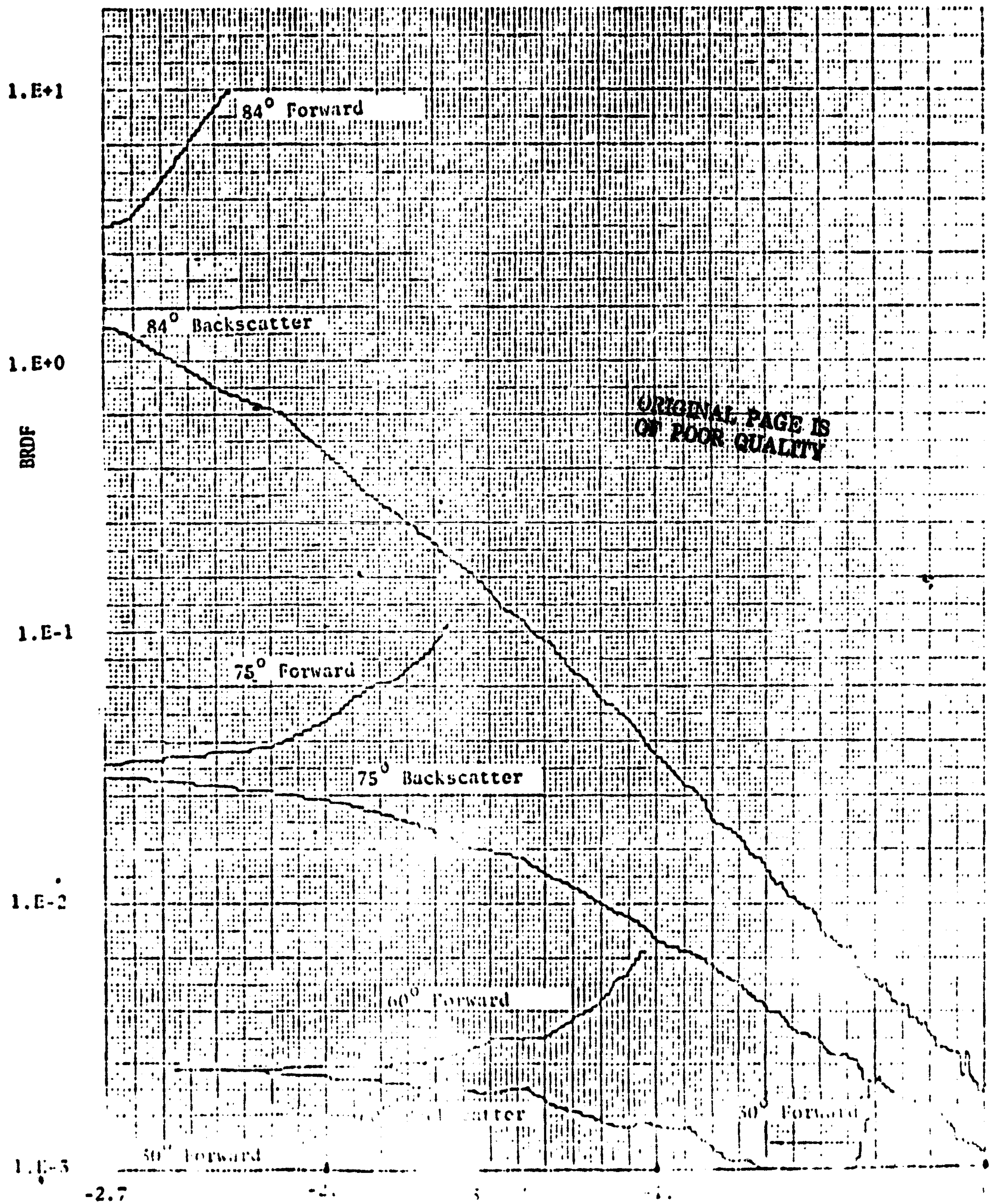

Fig. A7. Martin Black BRDF Data.[3] Helium-Neon 6328A.

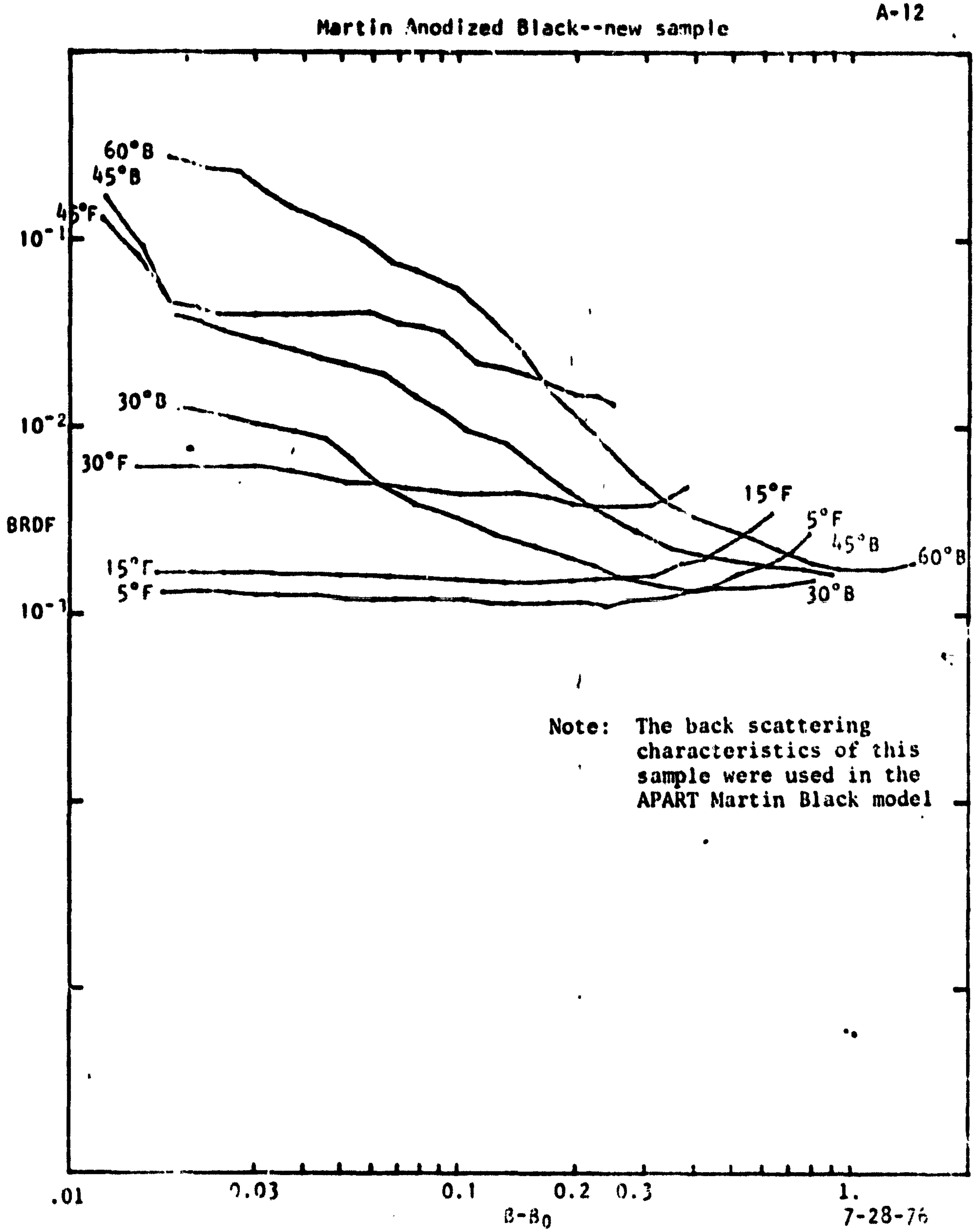

Fig. A8. University of Arizona 10.6μ Measurements of Martin Black.

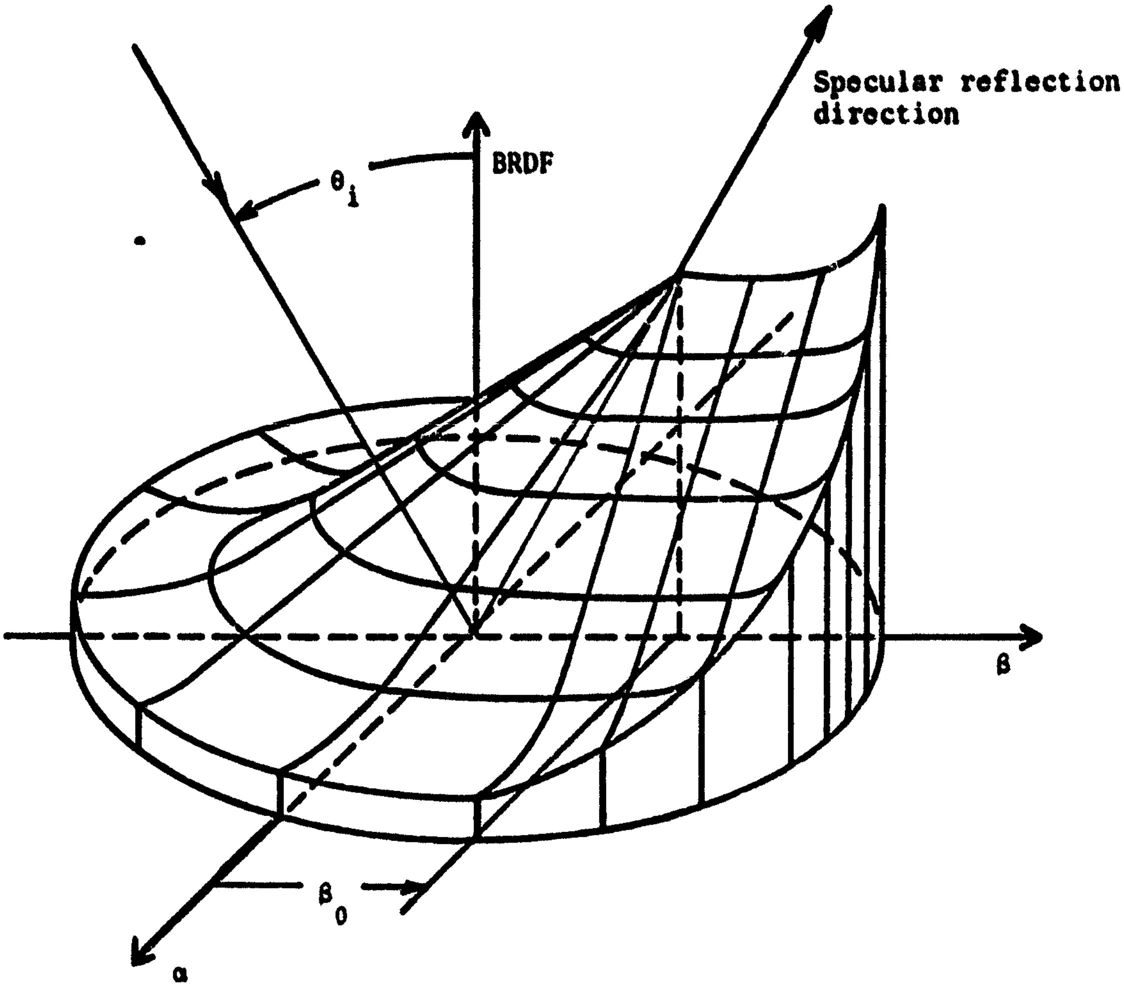

Fig. A9. Three-dimensional BRDF Model for Martin Black.

angle on a surface. When the Martin Black model is used in APART, this function is calculated for each previous source:source:collector combination. The BRDF as calculated by the APART model is plotted for several θ_i in Fig. A10.

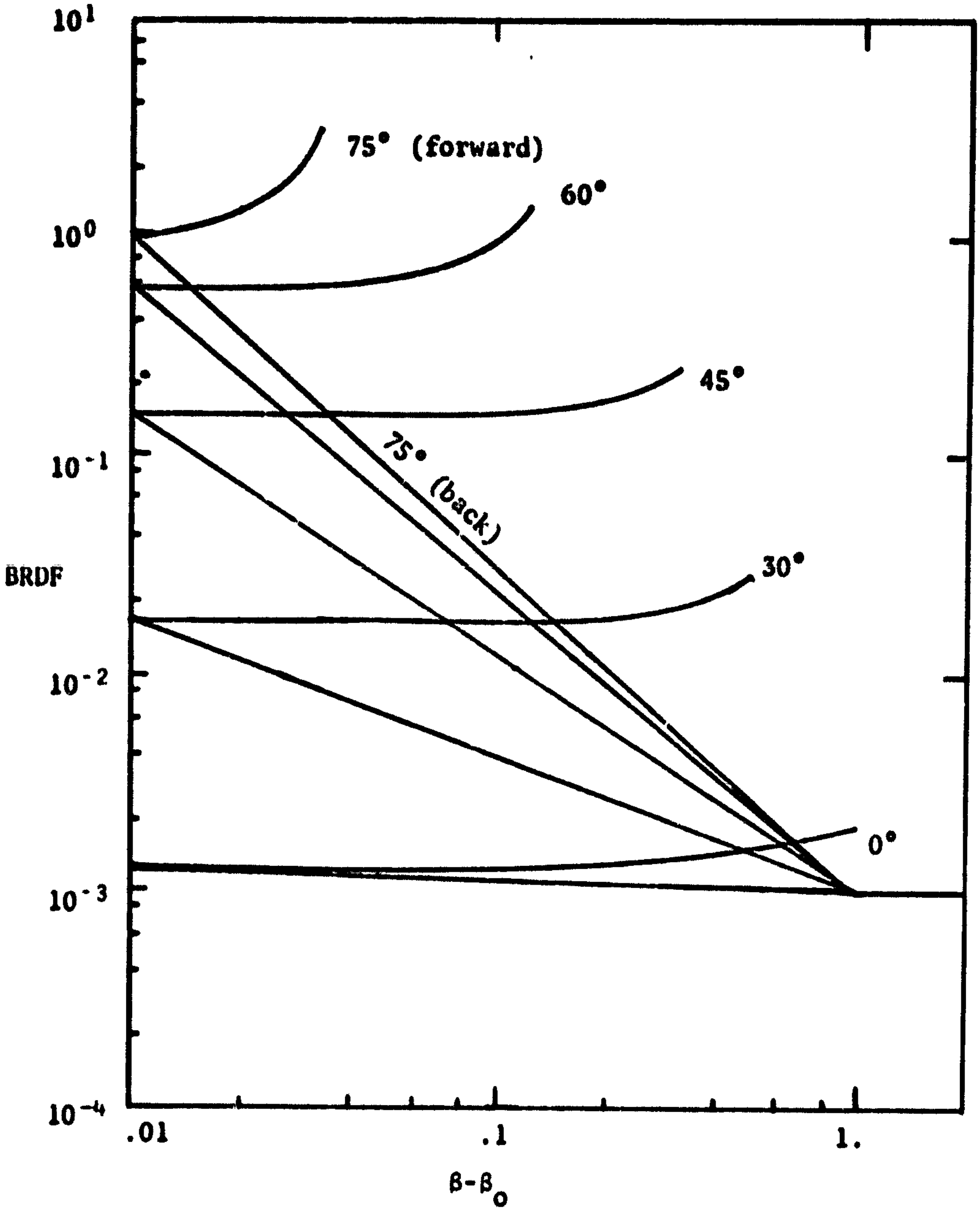

Fig. A10. BRDF of Martin Black Model.

APPENDIX B

B.0 COMPARISON OF BOUNDARY WAVE AND STATIONARY PHASE RESULTS WITH CLASSICAL DIFFRACTION SOLUTIONS.

The following analytical results were derived during the development of the PADE program for the purpose of comparing the results of the theory on which it is based with more established methods. Some of the solutions were also used as test cases for debugging the computer code.

B.1 THE SEMI-INFINITE PLANE (STRAIGHT EDGE)

There are very few closed form rigorous solutions of Maxwell's equations. One such is Sommerfeld's solution of the perfectly conducting, infinitely thin, semi-infinite sheet. The geometry and angle definitions are shown in Fig. B1

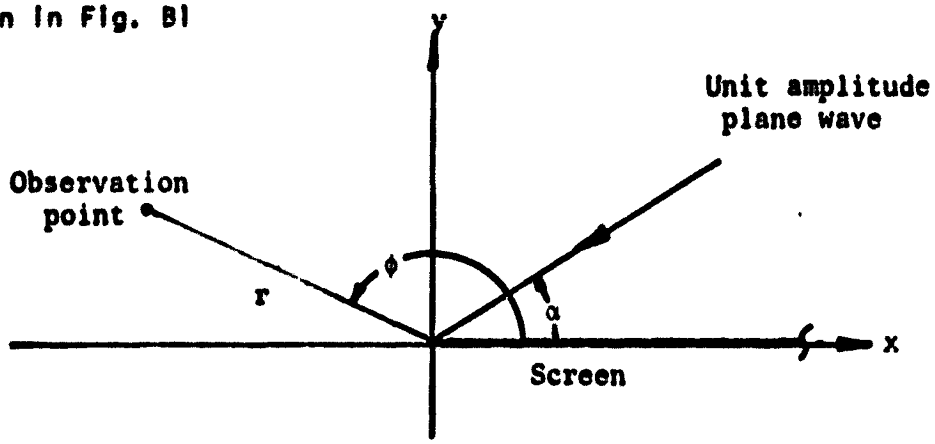

Fig. B1. Polar Coordinate System for Semi-Infinite Plane.

The Z-component of the electric field at the observation point is given by:

$$u(r,\phi,\alpha) = U(r,\phi-\alpha) \mp U(r,\phi+\alpha) \tag{B-1}$$

where

$$U(r,\psi) = \frac{1-i}{2} \int_{-\infty}^{\rho} e^{\frac{i\pi\tau^2}{2}} d \quad \text{and} \quad \rho = 2\sqrt{\frac{kr}{\pi}} \cdot \cos\frac{\psi}{2} \tag{B-2}$$

The first term represents the diffraction of the incident wave while the second term is due to the reflected wave. The minus sign is taken when the incident electric field vector is parallel to the plane of the screen. The plus sign corresponds to a polarization perpendicular to the screen.

For $r \gg \lambda$, the Fresnel integral U can be accurately represented by the first term of its asymptotic expansion. This is equivalent to applying the method of stationary phase to U. As a result, the total field u can be split into a geometrical and diffracted component, i.e.,

$$u = u_G + u_D \tag{B-3}$$

where

$$u_G = \begin{cases} e^{-ikr\cos(\phi-\alpha)} - e^{-ikr\cos(\phi+\alpha)} & 0 \le \phi < \pi-\alpha \\ e^{-ikr\cos(\theta-\alpha)} & \pi-\alpha < \phi < \pi+\alpha \\ 0 & \pi+\alpha < \phi \le 2\pi \end{cases} \tag{B-4}$$

and

$$u_D = \left[\mathrm{SEC}\left(\frac{\phi-\alpha}{2}\right) \mp \mathrm{SEC}\left(\frac{\phi+\alpha}{2}\right)\right] \cdot \frac{1}{4}\sqrt{\frac{2}{\pi kr}}\; e^{i(kr + \pi/4)} \tag{B-5}$$

It was this result that led Rubinowicz to seek a rigorous splitting into geometrical and diffracted components of the general scalar Kirchhoff field. How does his boundary wave result compare with the Sommerfeld solution? To make this comparison, one must realize that Kirchhoff theory deals with "black" or perfectly absorbing and not perfectly conducting or reflecting screens. By neglecting the effects of the reflected wave, the Sommerfeld solution can be modified for a "black" screen to yield:

$$u_G = \begin{cases} e^{-ikr\cos(\phi-\alpha)} & 0 < \phi < \pi + \alpha \\ 0 & \pi + \alpha < \phi < 2\pi \end{cases} \tag{B-6}$$

$$u_D = \mathrm{SEC}\left(\frac{\phi-\alpha}{2}\right) \frac{1}{4} \cdot \sqrt{\frac{2}{\pi kr}}\; e^{i(kr + \pi/4)} \tag{B-7}$$

Note that the field is now independent of incident polarization.

The corresponding boundary wave solution contains the same geometrical field. However, the diffracted field is given by:

$$u_D = -\frac{1}{4\pi} \int_{-\infty}^{\infty} \frac{e^{ikr}\;(\hat{r}\times\hat{\rho})\cdot\hat{z}}{4\pi r\;(1+\hat{r}\cdot\hat{\rho})}\,dz \tag{B-8}$$

which can be approximated by applying the method of stationary phase:

$$u_D = \frac{\sin(\phi-\alpha)}{4\pi r\cos(\phi-\alpha)} \cdot \sqrt{\frac{2\pi r}{k}}\; e^{i(kr + \pi/4)}$$

$$= -\,\mathrm{TAN}\left(\frac{\phi-\alpha}{2}\right) \cdot \frac{1}{4}\sqrt{\frac{2}{\pi kr}}\; e^{i(kr + \pi/4)} \tag{B-9}$$

The two solutions differ by only an obliquity factor which is a function of the angle from the incident direction:

$$\delta = \phi - \alpha \tag{B-10}$$

Figure B2 is the plot of the two obliquity factors as a function of the diffraction angle δ.

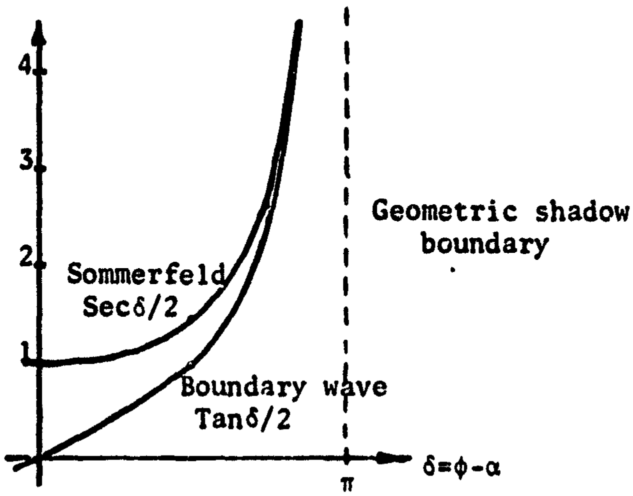

Fig. B2. Comparison of Sommerfeld and Boundary-wave Obliquity Factors.

Both solutions go to infinity at the boundary of the geometrical field. The biggest difference between the magnitudes of the two solutions occurs in the "back" diffraction direction, i.e., $\delta = 0$.

B.2 NEAR-FIELD ON-AXIS DIFFRACTION FROM A CIRCULAR APERTURE (OR OBSTACLE).

Even when one proceeds to a scalar theory, exact closed form solutions of diffraction problems are far and few between. In most cases the Fresnel or Fraunhofer approximations must be employed. One geometry that permits one to carry out the integration is when a circular aperture is illuminated by plane wave incident normal to the aperture and the observation point lies on a line normal to the aperture that passes through its center.

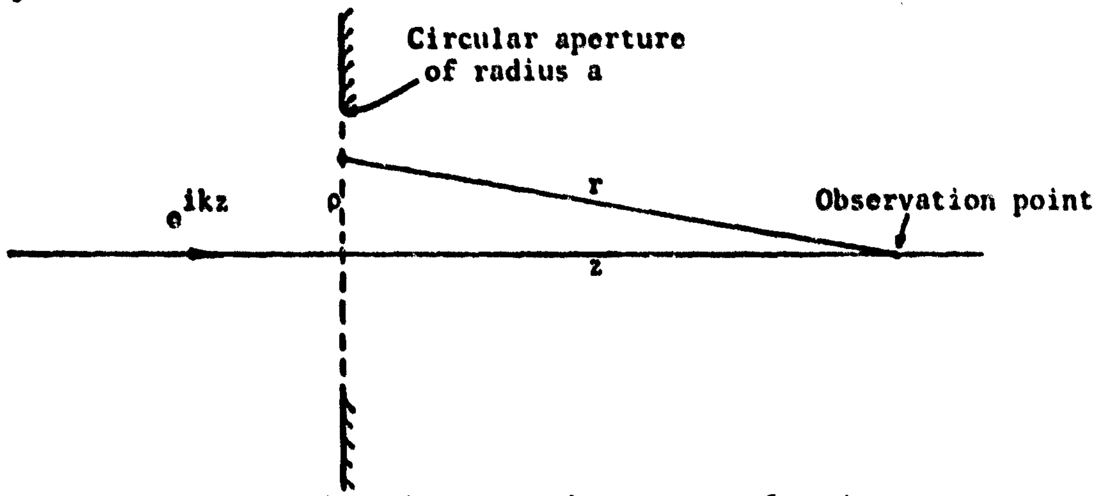

Fig. B3. Rotationally Symmetric Geometry for the Circular Aperture.

The total diffraction field is found by integrating Kirchhoff's formula over the area of the aperture.

$$u = \frac{1}{4\pi} \iint_A \left[\frac{e^{ikr}}{r} \frac{\partial u}{\partial n} - u \frac{\partial}{\partial n} \frac{e^{ikr}}{r} \right] d\sigma \qquad \text{(B-11)}$$

For this particular geometry this reduces to:

$$u = \frac{1}{2} e^{ikz} \int_0^a \frac{e^{ikr}}{r} \left[\frac{z(ik - \frac{1}{r})}{r} - ik\right] \rho d\rho \qquad \text{(B-12)}$$

After some work and integrating by parts:

$$u = e^{ikz} - \frac{1}{2}\left(1 + \frac{z}{d}\right) e^{ikd} \quad , \quad d = \sqrt{a^2 + z^2} \qquad \text{(B-13)}$$

The interesting thing to note here is that this rigorous scalar result ends up to be the sum of the incident wave and a wave that appears to originate from the edge of the aperture.

This result can be obtained with a lot less work by using the boundary wave formulation. The field is now given by

$$u = u_G + u_D = e^{ikz} + u_D \qquad \text{(B-14)}$$

where

$$u_D = -\frac{1}{4\pi} \int_0^{2\pi} \frac{e^{ikr}}{r} \frac{(\hat{r} \times \hat{\rho}) \cdot \ell}{(1 + \hat{r} \cdot \hat{\rho})} a d\theta$$

$$= -\frac{1}{4\pi} \frac{e^{ikd}}{d} \frac{a/d}{(1 - a/d)} a \int_0^{2\pi} d\theta$$

$$= -\frac{1}{2} \frac{a^2}{d^2(1 - z/d)} e^{ikd} \qquad \text{(B-15)}$$

Therefore

$$u = e^{ikz} - \frac{1}{2} \frac{a^2}{d^2(1 - z/d)} e^{ikd} \qquad \text{(B-16)}$$

This does indeed agree with the previous result since it can be shown that

$$\frac{a^2}{d^2(1 - z/d)} = \left(1 + \frac{z}{d}\right) \qquad \text{(B-17)}$$

It is worth noting at this point, that a different result would be obtained if the Rayleigh-Sommerfeld theory was employed. In this case:

$$u = e^{ikz} - \frac{z}{d} e^{ikd} \qquad (B-18)$$

Again the only difference is in the obliquity factor of the edge diffracted wave.

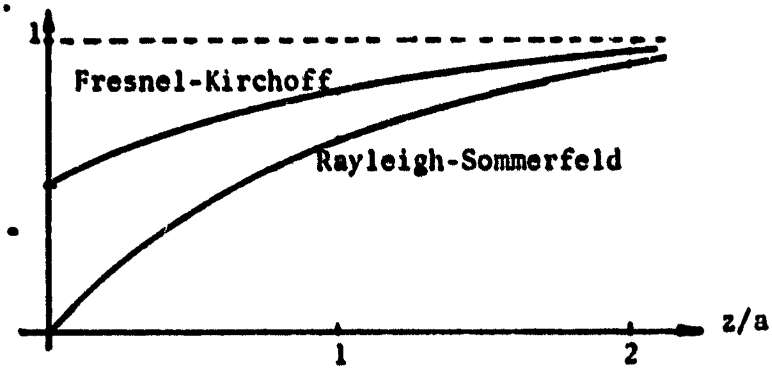

Fig. B4. Comparison of Fresnel-Kirchhoff and Rayleigh-Sommerfeld Obliquity Factors.

However, experimental measurements on relatively large apertures indicate that the Kirchhoff result is more accurate than the Rayleigh-Sommerfeld, even though the Kirchhoff theory is mathematically inconsistent.

It is now a trivial matter to obtain the field from a circular obstacle using the boundary wave formulation. With $u_G = 0$, it follows that

$$u = u_D = -\frac{1}{2}\left(1 + \frac{z}{d}\right) e^{ikd} \qquad (B-19)$$

The relative irradiance is equal to the squared modulus.

$$E = \frac{1}{4}\left(1 + \frac{z}{d}\right)^2 \qquad (B-20)$$

Therefore, the on-axis point behind a circular obstacle is always bright, as is well-known from observation. However, for the circular aperture, the irradiance at the on-axis point will go to zero at certain locations due to the interference of the incident field with the edge diffracted wave.

B.3 FAR-FIELD ON-AXIS DIFFRACTION FROM OBLIQUELY ILLUMINATED APERTURES

Wide-angle, far-field diffraction can be accurately described using the angular spectrum approach. If $a(x,y)$ is the aperture transmittance at $z=0$, then

$$u = \frac{\gamma+\gamma_i}{2} \frac{e^{ikr}}{i\lambda r} A(\alpha-\alpha_i \, , \, \beta-\beta_i) \tag{B-21}$$

and

$$A(\xi,\eta) = \iint_{-\infty}^{\infty} a(x,y) \, e^{-ik(\xi x+\eta y)} \, dxdy \tag{B-22}$$

and (α,β,γ) are the direction cosines of the observation point and $(\alpha_i, \beta_i, \gamma_i)$ of the intersection of the incident ray through the center of the aperture with the observation hemisphere of radius r.

B.3.1 The Rectangular Aperture.

For a rectangular aperture, the transmission function is:

$$a(x,y) = \mathrm{RECT}(\frac{x}{\Delta x}) \cdot \mathrm{RECT}(\frac{y}{\Delta y}) \tag{B-23}$$

therefore

$$A(\xi,\eta) = [\Delta x \cdot \mathrm{sinc}(\Delta x\xi/\lambda)] \cdot [\Delta y \cdot \mathrm{sinc}(\Delta y\eta/\lambda)] \tag{B-24}$$

where $$\mathrm{sinc}(x) = \frac{\sin(\pi x)}{\pi x}$$

The field is:

$$u = \frac{(\gamma+\gamma_i)\Delta x\Delta y}{2 \, i\lambda r} \, e^{ikr} \cdot \mathrm{sinc}[\Delta x(\alpha-\alpha_i)/\lambda] \cdot \mathrm{sinc}[\Delta y(\beta-\beta_i)/\lambda] \tag{B-25}$$

Consider the simplified geometry of Fig. B5.

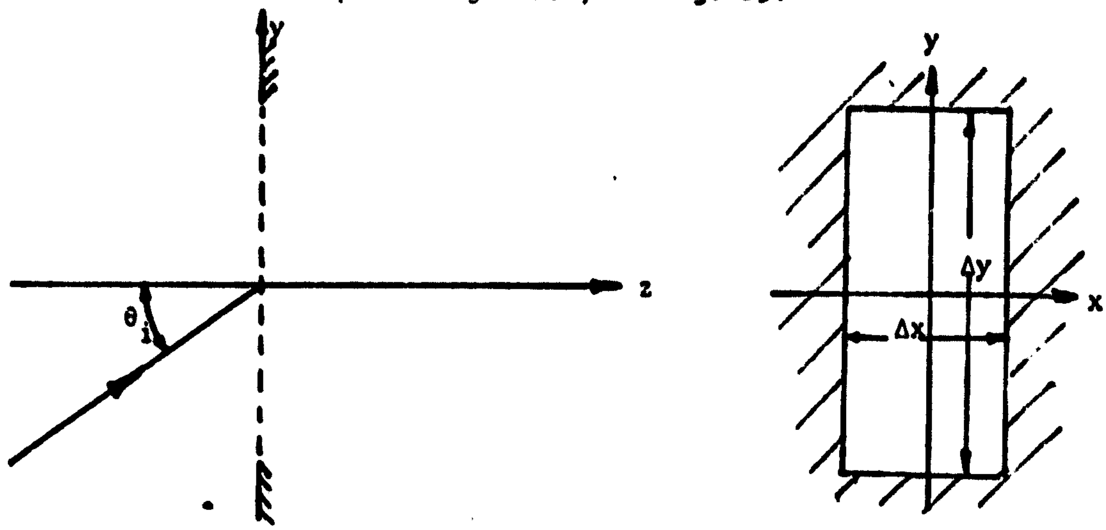

Fig. B5. Obliquely Illuminated Rectangular Aperture.

$$\text{where} \quad \begin{cases} \alpha = \alpha_i = \beta = 0 \\ r = z \\ \gamma = 1 \\ \beta_i = \sin\theta_i \\ \gamma_i = \cos\theta_i \end{cases} \tag{B-26}$$

Then, the expression for the field becomes

$$u = \frac{(1+\gamma_i)\ \Delta x}{i2\pi z\beta_i} \cdot \sin[k\beta_i\Delta y/2]\ e^{ikz} \quad . \tag{B-27}$$

Again, one can arrive at the same result without any complicated integration by applying the boundary wave formulation. First, note that the $(\hat{i}\times\hat{\rho})\cdot\hat{\ell}$ factor is zero for the two vertical edges, therefore they do not contribute to the diffracted field for this particular geometry.

For the top horizontal edge (#1)

$$(\hat{r}\times\hat{\rho})\cdot\hat{\ell} = \sin\theta_i = \beta_i \tag{B-28}$$

$$\hat{r}\cdot\hat{\rho} = -\cos\theta_i = -\gamma_i \tag{B-29}$$

$$r+\rho = z + \beta_i\,\Delta y/2 \tag{B-30}$$

Its contribution to the diffracted field is:

$$u_1 = \frac{1}{4\pi}\int_{-\Delta x/2}^{\Delta x/2} \frac{e^{ik(z+\beta_i\Delta y/2)}}{z}\,\frac{\sin\theta_i}{1-\cos\theta_i}\,dx$$

$$= -\frac{\beta_i\,\Delta x}{4\pi z(1-\gamma_i)}\,e^{ik(z+\beta_i\Delta y/2)} \tag{B-31}$$

Similarly for the bottom edge (#2)

$$u_2 = \frac{\beta_i\,\Delta x}{4\pi z(1-\gamma_i)}\,e^{ik(z+\beta_i\Delta y/2)} \tag{B-32}$$

The total diffracted field is the sum of the contributions from the two edges.

$$u = u_1 + u_2 = \frac{\beta_i\,\Delta x}{i2\pi z(1-\gamma_i)}\cdot\sin(k\beta_i\Delta y/2)e^{ikz} \tag{B-33}$$

Using the fact that $\beta_i^2 + \gamma_i^2 = 1$, one can show that $\frac{\beta_i}{1-\gamma_i} = \frac{1+\gamma_i}{\beta_i}$ and therefore the results of the two different methods are in exact agreement.

B.3.2 Circular Aperture

Consider now a circular aperture.

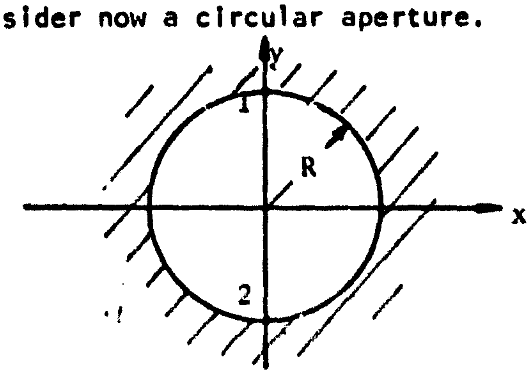

Fig. B6. Obliquely Illuminated Circular Aperture.

The transmission function is:

$$a(x,y) = \mathrm{CYL}\left(\frac{\sqrt{x^2+y^2}}{R}\right) = \begin{cases} 1 & (x^2+y^2) < R^2 \\ 0 & (x^2+y^2 > R^2 \end{cases} \tag{B-34}$$

Its transform

$$A(\xi,\eta) = \frac{R\ J_1\ (kR\sqrt{\xi^2+\eta^2})}{\sqrt{\xi^2+\eta^2}} \tag{B-35}$$

The diffracted field in the case of the geometry of the preceding section is therefore given by:

$$u = \frac{(1+\gamma_i)R}{i2\pi z\beta_i}\ J_1\ (kR\beta_i)\ e^{ikz} \tag{B-36}$$

In order to do the boundary wave calculation, it will be necessary to apply the principle of stationary phase to the integral around the edge of the aperture. For a circular aperture, the points of stationary phase correspond to the intersection of the aperture edge with a plane normal to it that passes through the source point, the center of the aperture, and the observation point. In this case, the points of intersect lie in the y-z plane. The two points of stationary phase are $(x,y) = 0 \pm R)$.

We can now proceed as in the previous section by noting that:

$$u''(\ell) = \frac{d^2}{d\ell^2}\ (r+\rho) = \frac{\beta_i}{R} \tag{B-37}$$

The contribution from the maximum o.p.d. point (#1) is:

$$u_1 = \frac{\beta_i}{4\pi z(1-\gamma_i)}\sqrt{\frac{R\lambda}{\beta_i}}\ e^{ik[z+R\beta_i]}\ e^{-i\pi/4} \tag{B-38}$$

Similarly for the minimum o.p.d. point:

$$u_2 = -\frac{\beta_i}{4\pi z(1-\gamma_i)}\sqrt{\frac{R\lambda}{\beta_i}}\; e^{ik[z-R\beta_i]}\; e^{i\pi/4} \tag{B-39}$$

The total field is:

$$u = u_1 + u_2 = \frac{\sqrt{\lambda R\beta_i}}{12\pi z(1-\gamma_i)}\; \sin(kR\beta_i - \pi/4)\; e^{ikz} \tag{B-40}$$

The two results are not in exact agreement but it can be shown that the second solution is a very good approximation to the first when $kR\beta_i >> 1$. The Bessel function can be approximated quite well by the first term of its asymptotoc expansion under this condition, i.e.,

$$J_1(x) \approx \sqrt{\frac{2}{\pi x}}\, \sin(x-\pi/4) \qquad x >> 1 \tag{B-41}$$

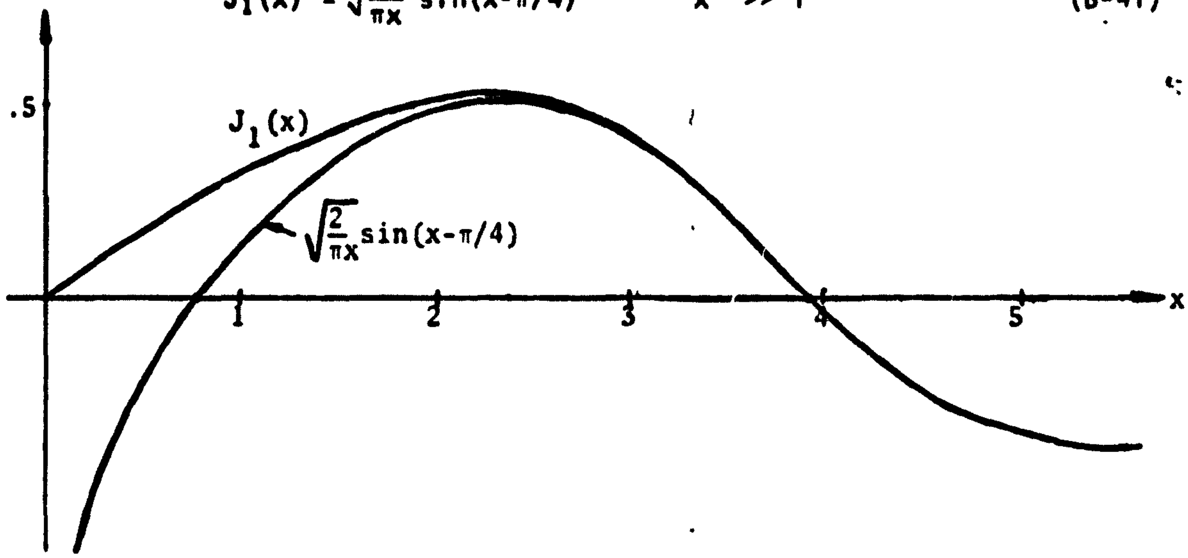

Fig. B7. Approximation to the First-order Bessel Function.

This combined with the fact that:

$$\frac{1+\beta_i}{\sqrt{\beta_i}^{\,3}} = \frac{\sqrt{\beta_i}}{1-\gamma_i}$$

transforms the first expression into the second.

B.3.3 Rotated Square Aperture

We will now treat the problem of a rotated square aperture. In particular, an aperture rotated 45° to yield a diamond.

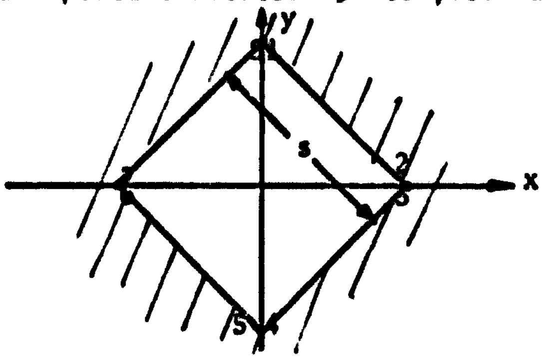

Fig. B8. Obliquely Illuminated Diamond Aperture.

In this case,

$$A(0,\eta) = \iint_{-\infty}^{\infty} a(x,y)\, e^{-ik\eta y}\, dxdy$$

$$= \int_{-\infty}^{\infty} \tilde{a}\,(y)\, e^{ik\eta y}\, dy \qquad \text{(B-42)}$$

$$\tilde{a}(y) = \int_{-\infty}^{\infty} a(x,y)\, dx = S\,\sqrt{2}\cdot \mathrm{TRI}(y\sqrt{2}/S) \qquad \text{(B-43)}$$

Therefore

$$A(0,\eta) = S^2 \cdot \mathrm{sinc}^2[s\eta/\lambda\sqrt{2}] \qquad \text{(B-44)}$$

and

$$u = \frac{(1+\gamma_i)\lambda}{\pi^2\, z\beta_i}\, \sin^2 (k\beta_i\; S/2\sqrt{2})\; e^{ikz} \qquad \text{(B-45)}$$

Again, we must use the method of stationary phase in order to solve the problem by the boundary wave technique. However, there are no points on the edge of this aperture for which the optical path is a maximum or minimum. Therefore the dominant contribution to the integral comes from the endpoints. Since the integration is broken up into four parts (one for each edge), there will be eight (8) different contributions to the integral (two endpoints per integral). Referring to Fig. B8, we find that for each endpoint:

Endpoint	$(\hat{r}\times\hat{\rho})\cdot\hat{\ell}$	$(\hat{r}+\hat{\rho})\cdot\hat{\ell}$	$(r+\rho)$
1	$\beta_i/\sqrt{2}$	$-\beta_i/\sqrt{2}$	$Z+\beta_i S/\sqrt{2}$
2	$\beta_i/\sqrt{2}$	$-\beta_i/\sqrt{2}$	Z
3	$-\beta_i/\sqrt{2}$	$-\beta_i/\sqrt{2}$	Z
4	$-\beta_i/\sqrt{2}$	$-\beta_i/\sqrt{2}$	$Z-\beta_i S/\sqrt{2}$
5	$-\beta_i/\sqrt{2}$	$\beta_i/\sqrt{2}$	$Z-\beta_i S/\sqrt{2}$
6	$-\beta_i/\sqrt{2}$	$\beta_i/\sqrt{2}$	Z
7	$\beta_i/\sqrt{2}$	$\beta_i/\sqrt{2}$	Z
8	$\beta_i/\sqrt{2}$	$\beta_i/\sqrt{2}$	$Z+\beta_i S/\sqrt{2}$

Therefore

$$u = \frac{\lambda e^{ikz}}{8\pi^2 z(1-\gamma_i)}\left[e^{ik\beta_i S/\sqrt{2}}-1-1+e^{-ik\beta_i S/\sqrt{2}}+e^{ik\beta_i S/\sqrt{2}}-1-1+e^{ik\beta_i S/\sqrt{2}}\right]$$

Combining terms, yields

$$u = \frac{\lambda}{\pi^2 z(1-\gamma_i)}\sin^2(k\beta_i S/2\sqrt{2})\, e^{ikz} \tag{B-46}$$

Since

$$\frac{1+\gamma_i}{\beta_i^{\,2}} = \frac{1}{1-\gamma_i} \tag{B-47}$$

This agrees exactly with the angular spectrum calculation even though we have used the stationary phase approximation. It turns out that stationary phase approximation as applied to the end points of the integration is the same as the linear phase approximation used in the angular spectrum approach.

APPENDIX C

APART, A FIRST-ORDER DETERMINISTIC STRAY RADIATION ANALYSIS PROGRAM

Steven R. Lange, Robert P. Breault, and Alan W. Greynolds
Optical Sciences Center, University of Arizona
Tucson, Arizona 85721

Abstract

The APART code (Arizona's Paraxial Analysis of Radiation Transfer) is a deterministic stray radiation analysis program capable of yielding quantitative descriptions of systems along with insight into the scattering mechanism present. APART uses y-ȳ geometrical optics to image primarily rotationally symmetrical systems. APART provides a sectional power map of the internal surfaces of a system and identifies "critical" objects seen from the image. Vane structures are modeled by configuration factors. Once the geometrical configuration factor between the internal objects has been calculated and stored, nonstructural changes to the system can be analyzed without re-running the complete program.

Introduction

The problem of analyzing scattered radiation in a sensor system is difficult because of the multiplicity of object configurations among which scattered energy can be transferred and because of the variation of the scattering characteristics of the surfaces. Any quantitative analysis of scattered energy within a system will involve an overwhelming number of calculations. One solution to this problem is to minimize the number of calculations in a manner that develops user insight into the scattering mechanisms involved in the system. One does not want just a number at the end of the analysis but also the knowledge of the significant factors involved that make up the number and how system changes affect the number. APART was developed to separate the problem into a logical sequence of procedures and calculations that develops user insight for improvement of the system and to minimize the computational effort.

Overview

APART is composed of three sub programs called: Program One, Program Two, and Program Three, which together perform four functions. These programs (Figure 1) communicate with each other by disk files containing system information and the results of calculations. The programs can be run separately or in one job sequence. Program One contains the code for two separate calculations: a scan from the image and the imaging of all objects in each space. The remaining programs must be executed sequentially, although one program may be executed many times before the next is executed.

Scan from Image

The first step in an APART analysis is to have the program "look out" from the image to determine which objects are seen either directly or in reflection. This calculation serves two functions: First, it will check for any design flaws that might be in the system. For example, one flaw might be an improperly designed baffle that allows energy from a stray radiation source to directly reach the detector. Program One scans from a selected image point outward to determine all objects that are seen from that image point. The program divides the length of the objects seen from the image into five sections and determines the position and angle at which each section is seen. APART also outputs a two-dimensional printer plot of the objects as they appear when projected onto the exit pupil of the system. With the combination of these outputs, one can quickly determine the status of the design. Redesign can take place at this point in the analysis at practically no cost to the user.

The second function served by Program One is to find the "critical" objects. These are the objects that scatter directly to the image and will be the sources at the final level of scatter. Thus, they have a "critical" effect on the system performance. The second to the last level of scatter is also partially determined; scattered radiation will be traced only to these "critical" objects. The final determination of the scattering paths is the linking of the objects that receive the initial unwanted energy to the critical objects, or to surfaces that scatter to the critical objects. A "level of scatter" is a scatter, or set of scatters, whereby radiation is transferred to another object. The other object may be the same one seen in reflection or even another part of the same object. Vane structure on an object will alter the number of scatters that will make up one level of scatter. The concept of levels of scatter is very important to the understanding of Program Three execution and will be explained further under "Program Three Calculations."

The scan from the image calculation is independent from the remainder of APART and can be rerun as many times as necessary to eliminate the design flaws or reduce the number of critical objects. Once the user is satisfied with the design as analyzed so far, he may continue the APART analysis.

Imaging All Objects in Each Space

The purpose of this step in the APART analysis is to identify the power transfers to be calculated later in the analysis. For very simple systems without any optical elements, one can write these transfers without any computer analysis. However, when one is considering a system with several imaging elements, it is not clear whether an object can transfer power to another through several optical elements. Program One helps in

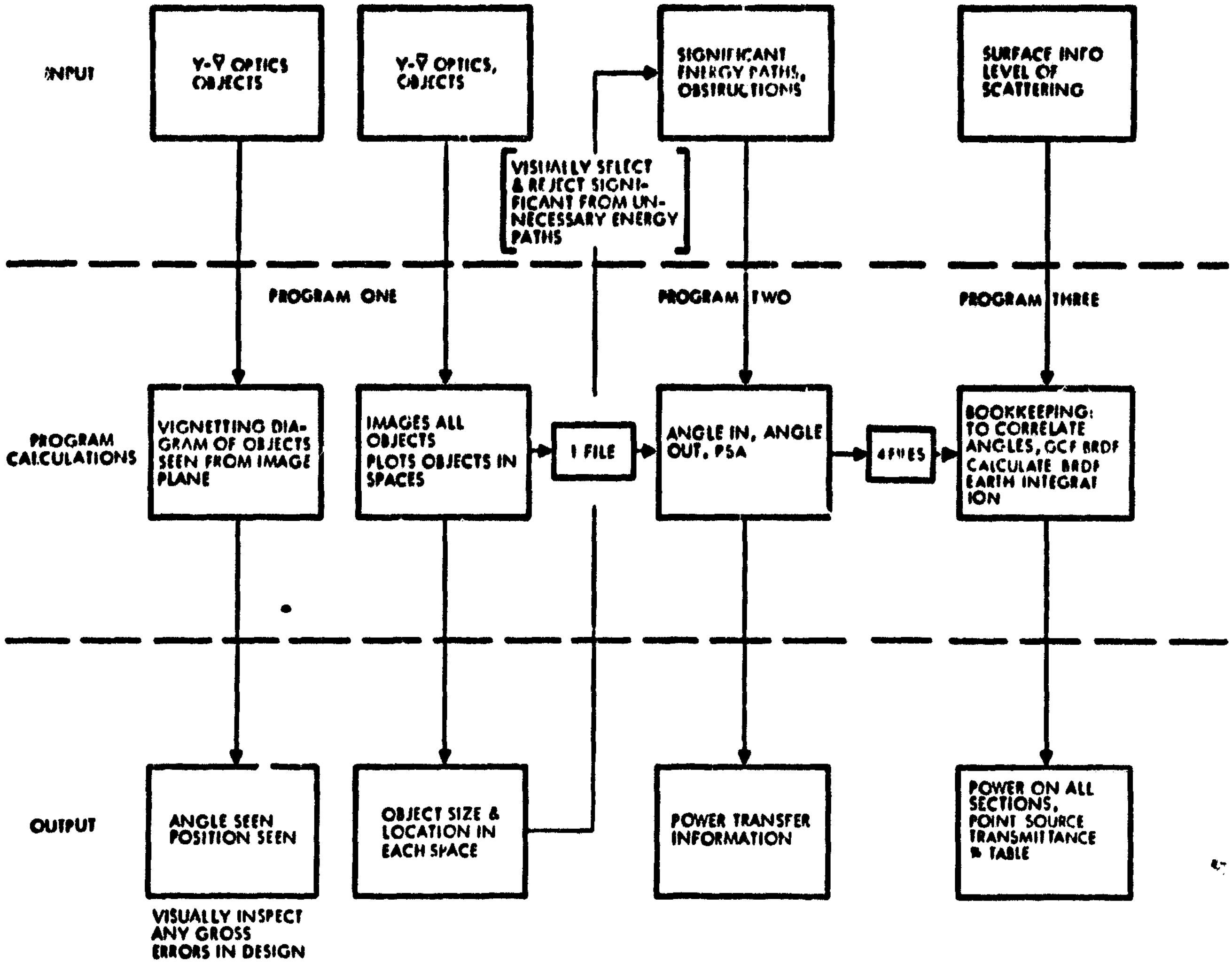

Fig. 1. Flow diagram of the APART program.

this determination by calculating the magnification and position of each object as it appears from each space within a system. The program plots this information from each space and, with the aid of a straight edge, can tell if power could transfer from one object to another. It is also easy to determine which objects might obscure any of the power to be transferred between the two objects. Several obscurations can block any or all of the beam, and these must be determined for input into the next program.

It is much more efficient to have the user select the objects that can be irradiated by the stray radiation source and select the paths that radiation can follow to reach the critical objects rather than have the computer blindly calculate every possible power transfer. By manually selecting the power transfers, one is doing a task quite simple for a human, and avoiding a very difficult, lengthy calculation for the computer. The other advantages in this interaction are that much computer time is saved by limiting the number of power transfers to be calculated, and the user gains insight into which power transfers are possible within a system and which surfaces can most influence the energy reaching the image.

Y-Ȳ Imaging Technique

Throughout Program One and Two imaging calculations are needed. To do this imaging, APART uses the first-order geometrical optics tool--the y-$\bar{y}$ diagram.[1,2] The y-$\bar{y}$ technique is much faster than other geometrical optical techniques. It allows the imaging of objects with a minimum of calculations regardless of the number of intervening imaging elements. APART must calculate the imaged location and the magnification of surfaces and obscurations to do the power transfer calculations. With the y-$\bar{y}$ technique, this is as simple as finding the intersection of two lines and calculating an area. Consider the y-$\bar{y}$ diagram for a simple mirror or lens with the object at minus infinity and the stop at the optical element (Figure 2). The distances between planes in the system, or points in the diagram, are given by the formula

$$t_{12} = n\,(y_1\bar{y}_2 - \bar{y}_1 y_2)/\mathcal{H} \qquad (1)$$

where $\mathcal{H}$ is the Lagrange invariant of the system and n is the index of refraction for the space in the system or the line in the diagram.

Imaged heights are calculated by constructing a "conjugate" line from the origin through the point to be imaged to the line representing the space into which the object is to be imaged (Figure 3). The intersection of the conjugate line and the image line gives the y' and $\bar{y}'$ points of the imaged plane. The imaged distance can be calculated using Equation (1), and the magnification is given by the ratio of the y or $\bar{y}$ values:

$$m = y'/y \text{ or } \bar{y}'/\bar{y}. \tag{2}$$

This technique is valid for any objects in any space within the system. Thus, the imaging involves quick calculations that avoid trigonometric and square root functions that are significantly more time consuming to calculate when compared to multiplication and division.

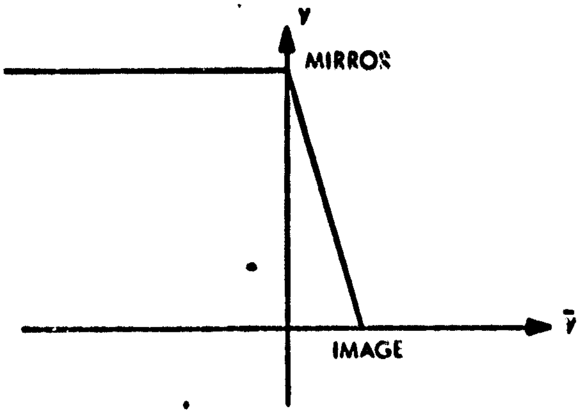

Fig. 2. Y-$\bar{Y}$ diagram of a one-mirror system.

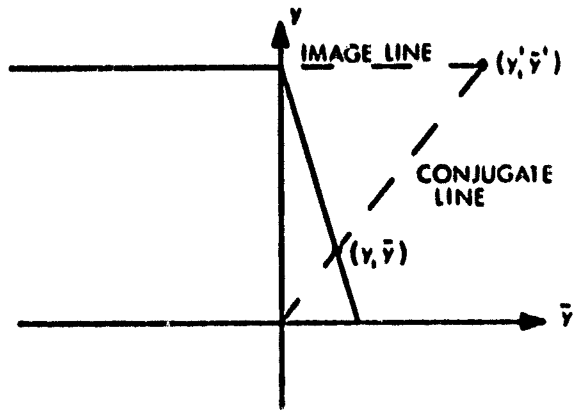

Fig. 3. Imaging of point $(y,\bar{y})$ into space one.

Power Transfer Calculations

Program Two calculates some of the factors leading up to the power transfer calculation in Program Three. Program Two divides all of the objects in the system into sections and if requested, into further subsections. APART calculates the power transfer from these sections to sections through the system to arrive at the total transferred energy.

Power Transfer Equations

The equation that relates power transfer from one section to another is

$$dP_c = [L_s(\theta,\phi)\, dA_s \cos(\theta_s)\, dA_c \cos(\theta_c)]/R^2_{sc} \tag{3}$$

where dP_c is the incremental amount of power transferred, $L_s(\theta,\phi)$ is the bidirectional radiance of the source section, dA_s and dA_c are the elemental areas of the source and collector, θ_s and θ_c are the angles that the line of sight from the source to the collector makes with the respective surface normals, and θ and ϕ are the projected and azimuthal angles.

The total power P_c on the collector section is found by the integration in closed form of a double integral over the areas of the source and collector and then by the evaluation of the resultant algebraic expression:

$$P_c = \iint([L_s(\theta,\phi)\cos(\theta_s)\cos(\theta_c)]/R^2_{sc})\, dA_s\, dA_c. \tag{4}$$

APART does a numerical integration by subdividing the objects into elemental sections that are small when compared to the distance between them. The integrals are evaluated as sums over the source and collector sections:

$$P_c = \sum_{A_c}\sum_{A_s}([L_s(\theta,\phi)\cos(\theta_s)\cos(\theta_c)\,\Delta A_s \Delta A_c]/R^2_{sc}). \tag{5}$$

The bidirectional reflectance distribution function (BRDF) is defined as

$$\mathrm{BRDF}(\theta_i,\phi_i;\theta_o,\phi_o) = \frac{L(\theta_o,\phi_o)}{E(\theta_i,\phi_i)} \tag{6}$$

where $E(\theta_i,\phi_i)$ is the bidirectional irradiance onto the source surface, and "i" and "o" refer to the incident (i) or scattered (o) direction of the ray. APART considers the radiance over the elemental area of the source as a constant and uses the BRDF to calculate the power incident on the collector as a function of the power incident on the source.

Multiplying and dividing Equation (3) by $E(\theta_i,\phi_i)$ and dropping the angular dependence for convenience yields

$$dP_c = \frac{L}{E} (E\, dA_s) \frac{\cos\theta_s \cos\theta_c\, dA_c}{R^2}. \tag{7}$$

Equation (7) has been separated into three terms that can be rewritten as

$$dP_c = \mathrm{BRDF}\; dP_s \cdot \mathrm{GCF}. \tag{8}$$

One can recognize the BRDF [as defined in Equation (6)] and dP_s as the power on the incremental source area and a new term called the geometrical configuration factor (GCF):

$$\mathrm{GCF} = \frac{\cos\theta_s \cos\theta_c\, dA_c}{R^2}. \tag{9}$$

When the power transfer equation has been written in the three-part form of Equation (8), the following qualitative statements can be made:

1) When only the coatings (BRDF) are varied to evaluate their effects on a system, the GCF does not change and it can be calculated once and stored for subsequent analysis.
2) When the system is not changed and only the source off-axis angle is altered in the analysis, the GCF remains fixed.
3) If an object in a system is altered in its size or shape, only transfers to or from this object, or transfers where it was used as an abscuration will need to be recalculated.

Program Two calculates the GCF between all previously determined source-collector combinations. Program Two also calculates and stores the angle information necessary for the calculation of the BRDF in Program Three. Thus, by storing this information, the computer time to do a number of analyses of a system is reduced tremendously.

Program Two divides objects into pi sections and axial, or z, sections. The reasons for this type of division will become apparent when symmetry rules are used. The program could divide the objects into hundreds of sections, but the storage problems in core become insurmountable, so APART limits the number of divisions of an object to 66. If more accuracy is desired, each section of each object may be further subdivided into as many subsections as one desires. Figure 4 illustrates how a cone can be divided. The result of the angle and GCF calculation between the subsections is averaged over one section-to-section transfer and stored for Program Three's use. Thus, problems such as accurately determining the shadow of a cone onto a cone can be handled with as much accuracy as desired.

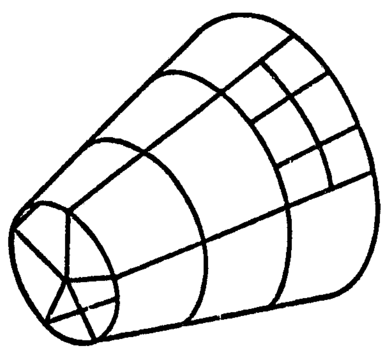

Fig. 4. Sections and subsections on a cone.

Symmetry Considerations

When objects within a system are rotationally symmetrical about the optical axis, APART can use the symmetry to further reduce the necessary GCF and angle calculations. One can see in Figure 5a that the transfer from pi section three to pi section one involves only an angle sign change from the pi section three to pi section five transfer. This use of symmetry eliminates 2/5 of the calculations. Furthermore, the above use of symmetry can be rotated, as in Figure 5b. The above transfers are the same as the transfer from pi section two to pi sections four or five. Thus, to completely specify a power transfer between objects with one z section and five pi sections, only three calculations are necessary. Twenty five calculations would be necessary for similarly sectioned objects that were asymmetrical.

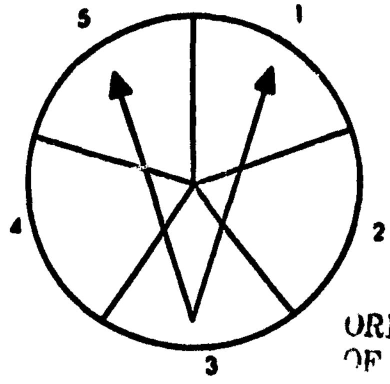

Fig. 5a

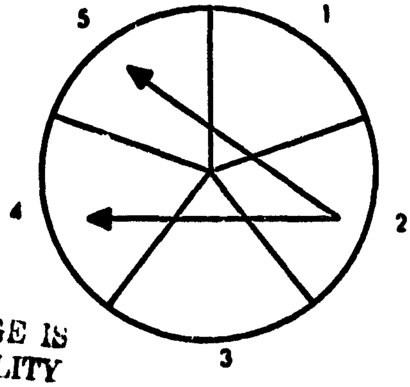

Fig. 5b

APART also uses this same type of symmetry when calculating the subsection-to-subsection transfers. Symmetry occurs here when the number of pi subsections on the source section equals the number of pi subsections on the collector section. This use of symmetry reduced the computer time for a three-by-three subsection transfer to about half of what it would have been with no symmetry.

Obstructions

Program Two considers obstructions when calculating the GCF. The obstructions, imaged or not, are handled in essentially the same manner as imaged objects. The vector from the source point to the collector point is used to determine the (x,y) intercept in the plane of an aperture or disk, where the intercept must be respectively inside or outside for power to pass. All obscurations are handled in a binary manner for the transfer between subsections to subsections. However, the average over a section-to-section transfer will result in a more realistic determination of the shadow. Obstructing conical sections pose additional problems because of their three-dimensional character. A ray now has the possibility of being blocked, passing around the cone, or passing through the cone. If the ray passes through both ends of the cone, the ray is not obstructed. Obviously, if the ray passes through one end and not the other, it fails. For the last case of a ray passing outside both cone ends, a further check must be made: from the source point, two planes can be drawn tangent to the obstructing cone, establishing a trapezoidal plane in space when intersected with the two cone ends. The ray is now checked for its position inside or outside of the trapezoid and, in conjunction with the other two tests, will determine the power transfer.

Now that the power transfers have been identified and the GCF and angle information for them calculated and stored, the APART analysis needs to calculate the remaining terms in Equation (8) and determine the resultant scatter throughout the system.

Program Three Calculations

Program Three has two main functions: to calculate the BRDF for each section within the system for the angles needed and to calculate the power increments throughout the system. The result is the amount of power on all of the objects and insight into how this power got there.

Surface Scatter Calculations

APART can accept BRDF values for a surface in a number of ways. First, actual data can be input in a tabled form. The data will be linearly interpolated for the angles actually encountered in Program Three. Second, the program can use any one of several models for the BRDF of the surface. The accuracy and speed of the models over the table lookup approach depend upon the coating, the cost, and the time to make sufficient measurements to fill the table.

The simplest model for surface scatter is a Lambertian model. Here, one inputs the total hemispherical reflectivity of the surface as a coating type for the surfaces on which it is to be used. The BRDF term in Equation (8) is a constant, and the calculation is finished. Because Lambertian scattering needs no angular information in Program Three, one can have Program Two ignore the lengthy surface angle calculations for these transfers, saving even more computer time.

Laboratory measurements of mirror surfaces have tended to indicate that a "smooth" mirror surface has a well-behaved linear shift-invariant BRDF function.(3) This function is linear when plotted on log-log paper with the ordinate being the BRDF and the abscissa being $(\beta-\beta_0)$ where β is the sine of the angle of scattering and β_0 is the sine of the specular angle. A typical example is shown in Figure 6. The program models this function by reading in the ordinate intercept at $\beta-\beta_o$ = 0.01 and the slope as plotted on the log-log paper. Average observed data can be input, or the results of a measurement program on the actual mirrors in a sensor can be used if the data are plotted and input as described.

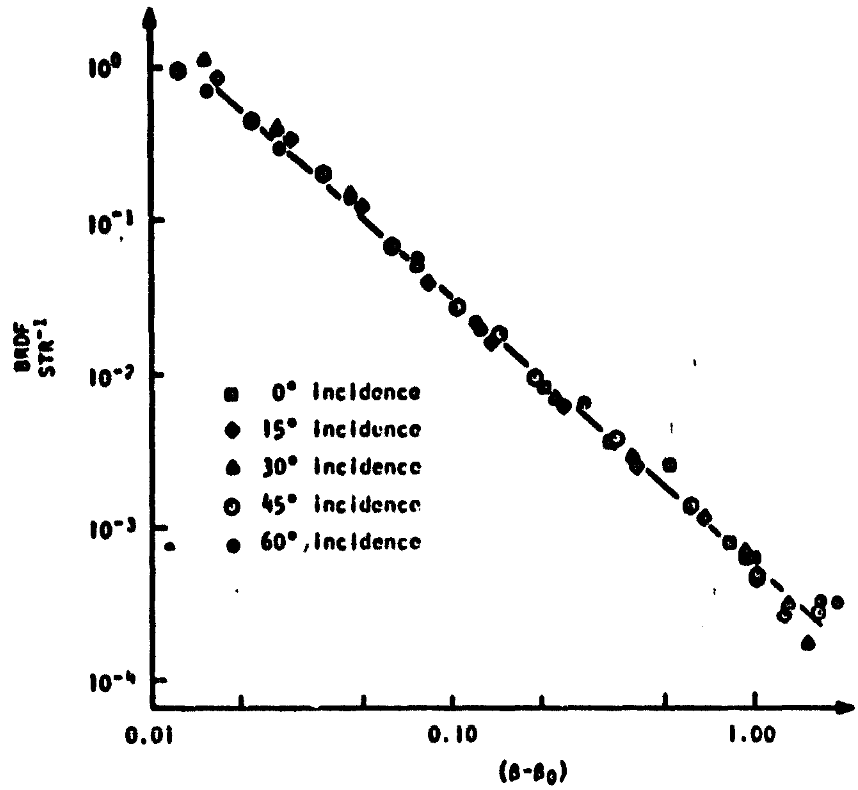

Fig. 6. BRDF of an average mirrbr.

For rougher surfaces that do not follow the linear shift-invariant properties observed on mirrors, there is a model called "blacks." This routine also utilizes data plotted in the Harvey-Shack manner described for the mirror surfaces above. These types of coatings are more similar to diffuse black surfaces like Martin Black or 3M Black Velvet than they are to mirrors. Measured data from these types of surfaces indicate that the slopes and starting points for small angle scattering change with the incident angle. Thus, the input for the program model includes a factor for the change in slope as a function of the incident angle and a factor for the change in BRDF at $\beta-\beta_0$ = 0.01. The calculations for this type of model are much longer than for the Lambertian model, and this model is intended to be used as a final analysis tool for a very accurate description of a sensor.

The addition of vanes to a surface is handled in a unique fashion. Up to this point in the analysis, all surfaces were treated as cylinders or disks. Cones that have vanes designed onto the baffle cones are considered to be conical sections with the cone being located at the locus of vane tips. Vanes could be handled by inputting each side of a vane as a disk, with a cylinder to separate the vanes. This would include a large number of objects in the system and a tremendous number of angle and GCF calculations in Program Two. Vanes, as handled by APART, need only one angle and GCF calculations per section. Program Three knows, for a given transfer, what the angle into the surface and the angle out of the surface will be. For the vaned surface, as well as any other model, the program calculates the apparent reflectivity of the surface for those angles. To handle vaned surfaces, Program Three utilizes configuration factor geometry to calculate the power transfers within the vanes resulting in the BRDF of the vaned section. Thus, APART replaces a vaned object with an equivalent nonvaned surface that has an associated highly unsymmetrical BRDF. The input parameters necessary to describe a vaned surface include: the angle at which the vanes are tilted, their depth below the locus of vane tips, their spacing, their diffuse reflectivity, and their distance from the optical axis.

All vaned surfaces will have edges on the vanes, and these edges are also handled in a unique manner. As was previously mentioned, APART knows the angle radiation is hitting a surface, and the angle radiation will leave the section on its way to the collector. Thus, for a toroidal edge, the illuminated and "seen" part of the edge can be easily calculated. The arc length of the overlap can also be calculated. The arc length, along with a correction factor for the angle at which the illuminated portion of the edge is seen, is assumed to be a cylinder just as in the vaned surface calculation. An apparent reflectivity is calculated for the small cylinder representing the arc length and is added to the vane reflectivity as calculated above. Thus, all edges within a system are calculated in a deterministic manner. The input parameters for this surface model are the diffuse reflectivity of the edges and the radius of curvature of the edge tip. APART can handle different reflectivities and edge radii for vane tips located in different sections of the same object.

Thus, APART can utilize a variety of measured data to calculate the BRDF of the surfaces. Now two of the variables in Equation (8) have been calculated for a given section-to-section transfer. All that remains in the analysis is to have the program cycle through all of the object's sections and accumulate the result from Equation (8).

Power Increments

The remaining term in Equation (8) to be calculated is dP_s. To start the calculations in Program Three, one must assign some starting amount of power onto some source(s) section. This initialized source may be a point located some distance from the entrance port of the system, if one is seeking to find a point source transmittance (PST). APART contains a simple loader routine that can load any or all sections of three objects with power. More sophisticated loader routines can be written that will include unusual obscurations or other situations not included in the general program.

The user must now enter the source-collector combinations as a function of the levels of scatter into Program Three. For example, at level one scatter the sources will be the objects that were loaded with the initial power. The collectors at level one scatter are all of the objects to which the sources can transfer power. The GCF's and angles for these transfers, as calculated in Program Two, must be recalled for this transfer calculation. The program will calculate dP_c for each source and collector section of the input combinations. Each increment of power reaching a collector section is stored separately and also is added after all power from all sources has been calculated. Thus, at the end of a level of scatter calculations, the program will have stored all increments of power to all the collectors and the total amount of power on each section of the collectors.

At the next level of scatter calculations, the above collectors will become sources. The sum of the increments of power on the collectors [Equation (5)] will become the dP_s of Equation (8). This sequence of calculations will continue until the image is a collector. The calculations can be carried out to a higher level of scatter if one wishes, but usually the energy reaching the image at the higher level is considerably lower than that received at a lower level of scatter.

One source section may contribute increments of power to the same collector section by several optical paths (i.e., directly or by reflection). When this power is then scattered from the collector into a single direction toward a second level collector, each increment of power incident on the first collector will contribute a different proportion of the scattered energy because of the different input angles. This is because the BRDF is generally angle dependent. Although the separate storage of these increments of power is a necessary and laborious task, it is responsible for the user's insight into the system scattering mechanisms.

The program can output a map of the increments of power reaching any object the user wishes. Of particular interest is a map of objects contributing power to the image. If a particular critical object is a major contributor of power, one can tell at a glance which sections on that critical object contributed the most power. Tables 1 and 2 illustrate some of the output from Program Three for two objects transferring power to the image.

Table 1. Power on One Section of the Image Coming from the Main Tube

This object is considered to the image

This is the power on pi section 3, z section 1

	0	0	0	0	0.18E-06	Total = 1.83E-07
	0	0	0	0	0	Total = 0
	0	0	0	0	0	Total = 0
	0	0	0	0	0	Total = 0
	0	0	0	0	0.18E-06	Total = 1.83E-07
Total	0	0	0	0	3.67E-07	

Total power to this section is 3.67E-07

Table 2. Power on One Section of the Image Coming from the Primary Mirror

This object is considered to the image

This is the power on pi section 3, z section 1

	0.38E-08	0.37E-08	0.37E-08	0.36E-08	0.35E-08	Total = 1.84E-08
	0	0	0	0	0	Total = 0
	0	0	0	0	0	Total = 0
	0	0	0	0	0	Total = 0
	0.38E-08	0.37E-08	0.37E-08	0.36E-08	0.35E-08	Total = 1.84E-08
Total	7.62E-09	7.49E-09	7.36E-09	7.23E-09	7.10E-09	

Total power to this section is 3.68E-08

There will be one array of this type for each section of the image and one group of arrays from all objects transferring power to it. The numbers in the arrays contain the increments of power incident on the image from each section of the source listed. In the examples shown, the source objects have five pi and z sections each. For example, the power incident on the image from the primary mirror's pi section one and z section four is 0.36E-08. The user could now realize that only two sections of the main tube transfer power to the image compared to 10 sections from the primary mirror. Furthermore, the power coming from the main tube is about 10 times higher than from the primary mirror. Thus, for the data presented, the significant path is from the fifth z section of the main tube to the image. One can also request that the increments of power to the critical objects be printed. In this manner, the user can trace all of the scattered radiation throughout the system and identify the radiation from the significant paths followed to reach the image.

The user, having identified the important scattering paths, now has available the possible alternatives to improve the system performance. First, one can rerun only the significant paths and vary the surface coatings on the critical objects to determine their effects. It is important to realize that the addition of coatings or vanes on a surface does not mean that all of APART must be rerun with new input throughout. All that must be done is to change one card of the Program Three input deck and rerun Program Three. This step can also be done in the same job sequence by stacking runs. If the result of this step does not result in sufficient system improvement, one can consider the possible redesign of the system to eliminate the sections of the critical objects from the view of the image. Rerunning the Program One scan from the image will be helpful in this procedure. A third possibility is to alter the radiation incident on the most important sections of the critical objects. If the power reaching the critical sections can be lowered by system redesign or surface coatings, the power on the image likewise will be reduced. Thus, with the use of APART the user knows just which steps are possible to alter the system performance.

Program Output

There are numerous output options available to the user of Program Three. The printing of the map of the power increments mentioned above is an example of a very detailed output. At the termination of each level of scatter, a running total of the power distribution on each object and the power incident at this level can be printed. Following all of the levels of scatter, a table of objects contributing power to the image can be output. This table lists the percent of the total energy reaching the image at each level of scatter from each object and the total power reaching the image at each level (Table 3). This percent table gives the user immediate insight into which objects are prime contributors and at what level they are; however, the knowledge of which sections of these objects are the most significant is lost in this output.

Table 3. A Percent Table for 3 Levels of Scatter

Percent of Power Contributed by Each Object as a Function Each Scattering Level

Objects	Level of Scatter 1	2	3
1 Source			
2 Main Tube	0.0	0.0	0.0
3 Outer Secondary Baf	0.0	2.4	100.0
4 Inner Secondary	0.0	0.0	0.0
5 Outer Conical	0.0	0.0	0.0
6 Inner Conical	0.0	0.4	0.0
7	0.0	0.0	0.0
8 Secondary Backing	0.0	0.0	0.0
9 Secondary Mirror	0.0	0.0	0.0
10 Primary Mirror	0.0	58.2	0.0
11 Entrance Port	0.0	39.0	0.0
12 Image Plane	0.0	0.0	0.0
13 Dummy	0.0	0.0	0.0
Total Power	0.0	0.477E-04	0.879E-07

*Representative Cassegrain Stray Radiation Analysis

Following the calculation of all levels of scatter for an off-axis source angle, the program can store information for comparison with other source angles. An accumulated percent table can be stored for up to 10 source angles. This table includes the total energy reaching the image and the percent of energy coming from each of the objects in the system making up that total. Thus, the user can see how the energy reaching the image changes with different off-axis source angles.

A figure of merit for the stray radiation rejection performance of the system called point source transmittance (PST) can be defined for each off-axis point as either

$$\text{PST} = \frac{\text{Power/unit area on image}}{\text{Power/unit area at entrance port perpendicular to source}} \qquad (10)$$

or,

$$PST = \frac{\text{Total power on image}}{\text{Total power on entrance port}}. \quad (11)$$

These PST's can be stored for each source angle and plotted against the off-axis angle at the end of a cycle of source angles. The plot can be either a printer plot or a Cal Comp plot.

Cycles of source angles can also be stacked in a single job execution. For example, one could run 10 source angles on a system with 90° baffle vanes on the main tube, alter the vane angles to 60°, and have the program plot both sets of results together. Up to eight cycles of source angles can be overplotted in one job execution. Parametric studies of the surface coatings as well as the effect of the BRDF on a system's performance can be made with very little setup time.

Earth Integration

With the generated PST data, the contribution from a broad source can be integrated by subdividing the source and determining the off-axis angle for each section. The PST curve can be interpolated and a resulting irradiance on the image calculated. Such a routine, written by Gary Hunt, Sperry Support Services, Huntsville, Alabama, has been incorporated into APART. It is designed to integrate the radiation from an earth-shaped object for a set of earth limb angles designated in the input. The PST values are spline interpolated for the off-axis subsections of the earth. The irradiance on the earth, albedo, earth's radius, orbital altitude, and look angles to the hard earth are input variables. Output is the irradiance on the image and the total power reaching the image as a function of a set of earth limb angles.

Comparison with Measured Data

The true value of an analysis program is measured by how accurately it predicts the real result. APART predictions have been compared to systems tested for their stray radiation rejection, and the results have usually been within a factor of two. The complex HOST sensor has been analyzed with APART[4] and the results have given us insight into how simple the scattering mechanisms can be, even in a complicated system. One system, a 0.5-m-diameter model of the Large Space Telescope (LST) has been designed, analyzed, fabricated, and tested to help determine APART's worth. Before testing started, an analysis of the system in its testing chamber revealed that the testing chamber was going to have a major influence on the amount of power reaching the image. As a result, the testing procedure had to be redesigned. The measured values gave very good agreement with the computer predictions.[5] The APART analysis was also helpful in directing the debugging of the test procedures.

Conclusion

The APART program has been written to analyze the stray radiation in optical systems. It was designed to be straightforward in structure with a versatile output and a simple nonredundant input. It gives the user an excellent insight into the scattering mechanisms present within a system and also a clear understanding of how to improve the system for better stray radiation performance. APART uses a minimum of computer core and central processor time because it stores the results of calculations to eliminate unnecessary recalculation. Its ability to accurately predict the system performance as well as its ability to develop user insight have dispelled some preconceived notions about scattering principles.

References

1. Delano, E., "First-Order Design and the y,$\bar{y}$ Diagram," Appl. Opt., Vol. 2, No. 12, pp. 1251-1256. 1963.
2. Shack, R. V., "Analytic System Design with a Pencil and Ruler--The Advantages of the y-$\bar{y}$ Diagram," Proc. SPIE, Vol. 39, Aug. 1973, Applications of Geometrical Optics.
3. Harvey, J. E., "Light-Scattering Characteristics of Optical Survaces," Ph.D. Dissertation, University of Arizona, 1976.
4. A Study Leading to Improvements in Radiation Focusing and Control in Infrared Sensors, Final report for D/A project 8X363304D215, Report No. AMMRC CTR 76-42, Army Materials & Mechanics Research Center, Watertown, Mass., 02172.
5. Hunt, G. H. and Shelton, G. B., "Experimental Measurement and Computer Analysis of Stray Radiation in a Telescope," in Proc. SPIE, Vol. 107, April 1977.